Delft University of Technology

Coherent structures in turbulence
Their generation, identification, and contribution to tracer particle dispersion

Goudar Vishwanathappa, Manu

DOI
10.4233/uuid:e9962229-d045-4614-876e-de3e7e5f188f

Publication date
2017

Document Version
Final published version

Citation (APA)
Goudar Vishwanathappa, M. (2017). *Coherent structures in turbulence: Their generation, identification, and contribution to tracer particle dispersion*. [Dissertation (TU Delft), Delft University of Technology]. https://doi.org/10.4233/uuid:e9962229-d045-4614-876e-de3e7e5f188f

Important note
To cite this publication, please use the final published version (if applicable).
Please check the document version above.

Copyright
Other than for strictly personal use, it is not permitted to download, forward or distribute the text or part of it, without the consent of the author(s) and/or copyright holder(s), unless the work is under an open content license such as Creative Commons.

Takedown policy
Please contact us and provide details if you believe this document breaches copyrights.
We will remove access to the work immediately and investigate your claim.

This work is downloaded from Delft University of Technology.
For technical reasons the number of authors shown on this cover page is limited to a maximum of 10.

COHERENT STRUCTURES IN TURBULENCE

THEIR GENERATION, IDENTIFICATION, AND CONTRIBUTION TO TRACER PARTICLE DISPERSION

MANU V GOUDAR

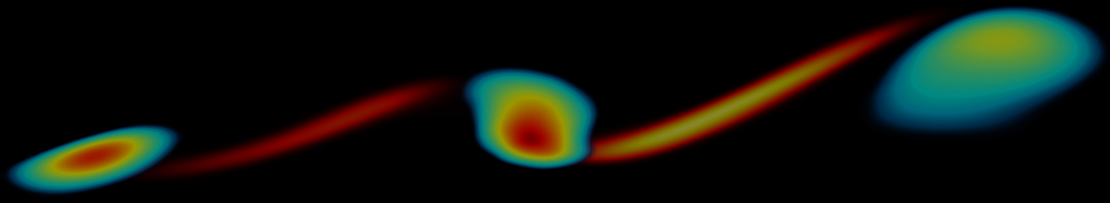

COHERENT STRUCTURES IN TURBULENCE

Their generation, identification and contribution to tracer particle dispersion

Proefschrift

ter verkrijging van de graad van doctor aan de Technische Universiteit Delft, op
gezag van de Rector Magnificus prof. ir. K.C.A.M. Luyben, voorzitter van het College
voor Promoties, in het openbaar te verdedigen op vrijdag 7 juli 2017 om 15:00 uur

door

Manu GOUDAR VISHWANATHAPPA

Master of Science in Mechanical Engineering
Technische Universiteit Delft
geboren te Shivapura, Karnataka, India.

This dissertation has been approved by the

Promotor	Prof. dr. ir. J. Westerweel
Copromotor	Dr. ir. G. E. Elsinga

Composition of the committee

Rector Magnificus	Chairman
Prof. dr. ir. J. Westerweel	Technische Universiteit Delft
Dr. ir. G. E. Elsinga	Technische Universiteit Delft
Independent members:	
Prof. dr. T. Ishihara	Nagoya University, Japan
Prof. dr. J. M. Foucaut	Ecole Centrale de Lille, France
Prof. dr. F. Toschi	Technische Universiteit Eindhoven
Prof. dr. J. G. M. Kuerten	Technische Universiteit Eindhoven
Prof. dr. ir. C. R. Kleijn	Technische Universiteit Delft
Reserve member:	
Prof. dr. ir. D. J. E. M. Roekaerts	Technische Universiteit Delft

This research was supported by the Dutch Technology Foundation (STW), which is a part of the Netherlands Organization for Scientific Research (NWO) and partly funded by the Ministry of Economic affairs (project number 11989).

Front : Cover depicts three vortices and dissipation between them in a cross-stream plane of a channel flow (Figure 3.1).

Back : Cover illustrates particle paths colored by the magnitude of velocity in a Burgers' vortex.

Copyright © 2017 by Manu V. Goudar, all rights reserved.

ISBN 978-94-92516-61-9
An electronic version of this dissertation is available at
`http://repository.tudelft.nl/`

ಈ ಮಹಾಪ್ರಬಂಧವನ್ನು ನನ್ನ ಪ್ರೀತಿಯ ತಾಯಿ, ತಂದೆ, ಮತ್ತು ಅಕ್ಕನಿಗೆ ಸಮರ್ಪಿಸುತ್ತೇನೆ.

Dedicated to my sister and parents.

SUMMARY

Turbulence is implicitly present or explicitly desired in many natural and industrial processes, such as, flow over solid surfaces, cloud formation, pollination, combustion, and chemical mixing. Hence, a better understanding of turbulence can aid in fuel saving by reducing drag in the case of flow over solid surfaces, namely, cars, airplanes, and ships. Furthermore, cloud formation models for refining weather modeling as well as the modeling of chemical mixing and combustion can be enhanced. However, there are different approaches to understand turbulence and in this thesis, turbulence is studied in terms of coherent structures.

One of the three-dimensional coherent structures description of wall-bounded turbulence is the *hairpin packet model*, where, the vortices are clustered in a packet. The existence of such packets has been explained by auto-generation mechanism [Smith et al., (1991)], where, a parent vortex of a threshold strength generates new off-spring vortices. However, such threshold strength vortices are rarely observed in actual turbulent flows. Additionally, the clustering of vortices in a packet also depends on the timescale of the generation of vortices, but no such timescale has been reported in literature until recently. Furthermore, the identification of the hairpin packets and the generation of new vortices is still done visually due to the lack of an objective identification criteria, even though the hairpin packet model is a few decades old. Hence in this thesis, how such threshold strength vortices come into existence, the timescale of generation of a vortex, and a proof of concept study to identify vortex packets objectively is examined. Additionally, the contribution of the structures found in hairpin packets, namely, vortices, shear-layers, or saddle points, on scalar transport is examined, which could assist in enhancing chemical mixing and combustion.

The creation of threshold strength vortices is explored by examining the interactions between commonly found weak vortices and checking if they initiate subsequent auto-generation. Here, the evolution of two weak conditional vortices with different initial strengths, initial sizes and initial stream-wise spacing between them is studied. The numerical procedure followed is similar to Zhou et al., (1999). The two vortices are found to merge to form a single stronger vortex, when the upstream vortex is located at higher wall-normal location. This strong merged vortex further auto-generated depending on the initial stream-wise separation between vortices. Further investigations

led to the modification of the auto-generation mechanism, where, the ejection events rapidly lift-up the head of the parent vortex, leading to the blockage of flow upstream and the generation of a new vortex upstream by shear-layer roll-up. This modified auto-generation mechanism differs from the existing one at the later stages of auto-generation, where the blockage of flow upstream and shear-layer roll-up are considered instead of vortex dynamics. Additionally, this modified mechanism can explain the auto-generation in single legged or asymmetric vortices, which is observed in actual turbulent channel flow at friction Reynolds number $Re_\tau = 180$.

The timescale of auto-generation in turbulent channel flow at $Re_\tau = 180$ is determined visually. The timescale is found to be $10 - 15$ time wall units, which is similar to experimental results by Jodai and Elsinga, (2016). However, this is an order of magnitude smaller than the timescale observed in the idealized auto-generation simulations ($80 - 250$ time wall units). As the generation of new vortices is linked to the creation of ejection events, this timescale could be utilized to actively modify the turbulent flow, either to enhance turbulence or to reduce drag. However, it should be noted that the statistical description of the timescale of auto-generation and the number of vortices generated remains an open issue.

At present, the statistical relevance of hairpin packets and auto-generation is difficult to establish due to the lack of objective identification methods to identify vortex packets and auto-generation in actual turbulent flows. Therefore, it becomes important to know more about a hairpin packet in order develop an objective method. Hence, a proof of concept study, where, a link between a hairpin packet and a shear-layer structure [Elsinga and Marusic, (2010)] is explored in actual turbulent channel flow. It will be shown that the two consecutive co-rotating vortices in a hairpin packet can be viewed in a different frame of reference (i.e., the principal straining directions) as a shear-layer structure. Hence, a general shear-layer detection scheme could be utilized to detect shear-layer structure containing co-rotating vortices. Furthermore, based on the pattern of the identified co-rotating vortices a hairpin packet could be objectively identified. Additionally, as the shear-layer structure is observed in all kinds of flows and considered universal, its instantaneous existence in different flows and the connection to packet of vortices could be explored in future.

In the final part of this thesis, the relevance of general flow structures, namely, the Burgers' vortex, the shear-layer structure, and the node-saddle topology, in the dispersion of tracer particles is studied. These idealized three-dimensional structures are considered as they represent typical elliptical and hyperbolic critical points. These critical points are shown to affect the dispersion in two-dimensional turbulence by Goto and Vassilicos, (2004) and the present study extends this to three-dimensions. Differ-

ent dispersion statistics, such as, pair dispersion, material lines, and tetrad dispersion, are studied and compared to actual isotropic turbulent flow statistics. Also, the snapshots of particle distribution at different times is presented to understand the influence of the different features of these structures on the dispersion statistics. Moreover, the shear-layer structure is observed to closely resemble the actual turbulent flow statistics qualitatively and quantitatively. The Burgers' vortex is found to deviate the most, whereas the node-saddle topology did exhibit some similarities to actual turbulent dispersion statistics. However, it deviated in the geometrical features associated with the material lines and tetrad dispersion.

To conclude, this thesis improved the existing hairpin packet model and modified the existing auto-generation mechanism. Additionally, it provided some insights on the timescale of auto-generation, which could be utilized to improve existing active flow control and modification techniques. Furthermore, the influence of different three-dimensional ideal structures on dispersion statistics is also shown.

SAMENVATTING

Turbulentie is impliciet aanwezig of expliciet gewenst in veel natuurlijke en industriële processen, zoals stroming over vaste oppervlakken, de formatie van wolken, bestuiving, verbranding en het mengen van chemische stoffen. Bovendien kan een beter begrip van turbulentie helpen bij het besparen van brandstof door weerstandsvermindering van stroming over vaste oppervlakken, zoals bij auto's, vliegtuigen en schepen. Bovendien kunnen wolkvormingsmodellen voor het verfijning van weermodellering, evenals de modellering van chemische menging en verbranding, worden verbeterd. Er zijn echter verschillende benaderingen om turbulentie te begrijpen, in dit proefschrift wordt turbulentie bestudeerd door middel van coherente structuren.

Een omschrijving van driedimensionale coherente structuren van de door een wand begrensde turbulentie wordt gegeven door het haarspeldpakketmodel, hierin zijn wervelingen in een pakket gegroepeerd. Het bestaan van dergelijke pakketten is uitgelegd door het auto-generatie mechanisme [Smith et al., (1991)], waar een voldoende sterke bronwerveling nieuwe wervelingen produceert. Echter, dergelijke sterke wervelingen worden zelden waargenomen in een daadwerkelijke turbulente stroming. Bovendien hangt de clustering van wervelingen in een pakket ook af van de tijdschaal van de opwekking van wervelingen, maar tot dusver is een dergelijk tijdschaal niet in de literatuur vermeld. Bovendien wordt de identificatie van de haarspeldpakketten en de opwekking van nieuwe wervelingen vooralsnog visueel gedaan vanwege een gebrek aan objectieve identificatiecriteria. Vandaar dat in dit proefschrift wordt onderzocht hoe wervelingen van een bepaalde drempelwaarde sterkte tot stand komen, en wat de tijdschaal van de generatie van een werveling is. Ook bevat dit proefschrift een conceptstudie naar een methode om wervelingpakketten objectief te kunnen identificeren. Daarnaast wordt de bijdrage van coherente structuren (i.e., wervelingen, schuiflagen of zadelpunten) op het scalaire transport onderzocht. Dit zou kunnen bijdragen tot het verbeteren van verbranding en chemisch mengen.

Het creëren van wervelingen van een bepaalde drempelwaarde sterkte is onderzocht door de interacties tussen zwakke wervelingen te bestuderen, en te controleren of deze vervolgens auto-generatie initiëren. Hierbij wordt de evolutie van twee zwakke conditionele wervelingen met verschillende initiële sterktes, initiële groottes, en initiële afstand in stromingsrichting tussen deze wervelingen onderzocht. De gebruikte numerieke procedure is vergelijkbaar met Zhou et al., (1999). De twee wervelingen smelten samen om een enkele sterkere werveling te vormen wanneer de stroomopwaartse werveling zich op een hogere positie langs de wand bevindt. Deze sterke samengesmolten werveling wordt verder automatisch gegenereerd afhankelijk van de initiële stroomsgewijze scheiding tussen wervelingen. Verder onderzoek heeft geleidt tot een wijziging van het mechanisme voor auto-generatie, waarbij de ejection de top van de bronwerveling snel van de wand af beweegt. Hierdoor wordt de stroming stroomopwaarts geblokkeerd, en een nieuwe werveling wordt stroomopwaarts opgewekt door een oprollende schuiflaag. Dit gewijzigde auto-generatiemechanisme verschilt van het bestaande in de latere stadia van de auto-generatie, waarbij de blokkering van de stroming stroomopwaarts en het oprollen van de schuiflaag wordt beschouwd in plaats van de dynamiek van wervelingen. Bovendien kan dit gemodificeerde mechanisme de auto-generatie in single legged of asymmetrische wervelingen verklaren, welke waargenomen zijn in daadwerkelijke turbulente kanaalstroming bij een wrijvings Reynolds getal $Re_\tau = 180$.

De tijdschaal van auto-generatie in turbulente kanaalstroming bij $Re_\tau = 180$ wordt visueel bepaald. De tijdschaal blijkt 10 tot 15 keer de wandeenheid te zijn, hetgeen vergelijkbaar is met experimentele resultaten van Jodai and Elsinga, (2016). Echter, dit is een orde van grootte kleiner dan de tijdschaal waargenomen in de geïdealiseerde auto-generatie simulaties (80 tot 250 keer de wandeenheid). Aangezien het genereren van nieuwe wervelingen gekoppeld is aan het creëren van ejection, kan deze tijdschaal gebruikt worden om de turbulente stroming actief te wijzigen, met als doel om turbulentie te verhogen of om stromingsweerstand te verminderen. Er moet echter op worden gewezen dat de statistische omschrijving van de tijdschaal van de automatische generatie en het aantal genereerde wervelingen een open probleem blijft.

Op dit moment is de statistische relevantie van haarspeldpakketten en autogeneratie moeilijk te bepalen. Dit komt door een gebrek aan objectieve identificatiemethoden om wervelingpakketten en auto-generatie in een daadwerkelijke turbulente stroming te identificeren. Daarom is het belangrijk om meer te weten te komen over een haarspeldpakket om zo een objectieve methode te ontwikkelen. Vandaar is een concept studie gedaan, waar een verband tussen een haarspeldpakket en een schuiflaagstructuur wordt onderzocht in de daadwerkelijke turbulente kanaalstroming [Elsinga and Marusic, (2010)]. Het zal worden aangetoond dat de twee opeenvolgende co-roterende wervelingen in een haarspeldpakket in een ander referentiekader (i.e., de hoofd afschuifrichtingen) kunnen worden beschouwd als een schuiflaagstructuur. Vandaar kan een algemeen schuiflaagdetectieschema worden gebruikt om schuiflaagstructuur te detecteren welke co-roterende wervelingen bevat. Voorts kan op basis van het patroon van de geïdentificeerde co-roterende wervelingen een haarspeldpakket objectief worden geïdentificeerd. Daarnaast, aangezien de schuiflaagstructuur in allerlei stromingen wordt waargenomen en als universeel wordt beschouwd, kan het instantane bestaan in verschillende stromingen en de verbinding met wervelingpakketten verder worden onderzocht.

In het laatste deel van dit proefschrift wordt de relevantie van algemene stromingsstructuren, namelijk de Burgers' werveling, de schuiflaagstructuur, en de knoop-zadel topologie in de verspreiding van tracer deeltjes bestudeerd. Deze geidealiseerde drie-dimensionale structuren worden beschouwd aangezien deze typische elliptische en hyperbolische kritische punten vertegenwoordigen. Deze kritische punten beinvloeden de dispersie in twee-dimensionale turbulentie zoals Goto and Vassilicos, (2004) laten zien, terwijl de huidige studie dit uitbreidt tot drie dimensies. Verschillende dispersiestatistieken, zoals paardispersie, materiaallijnen en tetrad dispersie, zijn bestudeerd en vergeleken met de isotrope turbulente stromingsstatistieken. Ook worden momentopnames van de deeltjesverdeling op verschillende tijdstippen gepresenteerd om de invloed van de verschillende kenmerken van deze structuren op de dispersiestatistieken te begrijpen. Bovendien is waargenomen dat de structuur van de schuiflaag zowel kwalitatief als kwantitatief erg lijkt op die van de werkelijke turbulente stromingsstatistieken. De Burgers' werveling blijkt het meest af te wijken, terwijl de knoop-zadel topologie een aantal overeenkomsten vertoont met de daadwerkelijke turbulente dispersiestatistieken. Echter, deze wijkt af van de geometrische kenmerken die verband houden met de materiaallijnen en tetrad dispersie.

Samenvattend, dit proefschrift beschrijft een verbetering van het bestaande haarspeldpakketmodel en een wijziging van het bestaande auto-generatiemechanisme. Daarnaast worden een aantal inzichten in de tijdsduur van de automatische generatie gegeven, welke kan worden gebruikt om bestaande actieve flow control en modificatie technieken te verbeteren. Bovendien wordt ook de invloed van verschillende driedimensionale ideale structuren op dispersiestatistieken getoond.

CONTENTS

1 INTRODUCTION 1
- 1.1 Objectives 4

2 AUTO-GENERATION IN WALL-TURBULENCE 5
- 2.1 Introduction 5
- 2.2 Methodology 9
  - 2.2.1 Numerical Method 9
  - 2.2.2 Conditional eddy 10
  - 2.2.3 Simulation types 11
- 2.3 Results and discussion 14
  - 2.3.1 Two-eddy case 14
  - 2.3.2 Role of low-speed streaks 20
  - 2.3.3 A modified auto-generation mechanism 21
- 2.4 Conclusions 25

3 TIME SCALE OF AUTO-GENERATION 29
- 3.1 Introduction 29
- 3.2 Methodology 30
  - 3.2.1 Identification of a vortex packet and auto-generation 31
- 3.3 Results and discussion 33
- 3.4 Conclusion 36

4 THE TALE OF TWO CO-ROTATING VORTICES 37
- 4.1 Introduction 37
- 4.2 Methodology 39
  - 4.2.1 Shear-layer structure (SLS) extraction 41
- 4.3 Results and discussion 44
  - 4.3.1 Instantaneous shear-layer structure 44
  - 4.3.2 Auto-generation and shear-layer structure 47
  - 4.3.3 Implications and future developments 49
- 4.4 Conclusions 50

5 TRACER PARTICLE DISPERSION AROUND ELEMENTARY FLOW PATTERNS 53
- 5.1 Introduction 53
- 5.2 Flow structures 55

5.2.1 Burgers' vortex (BV) . . . 55
5.2.2 Shear-layer structure (SLS) . . . 58
5.2.3 Node-Saddle topology . . . 58
5.3 Particle simulation and statistics . . . 59
5.3.1 Pair dispersion . . . 60
5.3.2 Material lines . . . 61
5.3.3 Four-particle dispersion . . . 62
5.4 Results . . . 63
5.4.1 Pair dispersion . . . 63
5.4.2 Instantaneous distribution of particles . . . 66
5.4.3 Material lines . . . 69
5.4.4 Four particle dispersion . . . 72
5.5 Conclusions . . . 74
6 CONCLUSIONS AND RECOMMENDATIONS 77
6.1 Auto-generation in wall-turbulence . . . 77
6.2 Auto-generation in turbulent flow and its timescale . . . 79
6.3 Shear-layer structure and vortex packet . . . 79
6.4 Dispersion around idealized flow patterns . . . 80
A APPENDIX : DIRECT NUMERICAL SIMULATION 81
A.1 DNS code details . . . 81
A.1.1 Non-dimensionalized Navier Stokes equation . . . 81
A.1.2 Time Integration: Runge-Kutta scheme . . . 82
A.1.3 Spatial discretisation . . . 83
A.2 Code validation . . . 83
B APPENDIX : ADDITIONAL EXAMPLES 89
B.1 Auto-generation . . . 89
B.2 Shear-layer structures and vortex packets . . . 90

REFERENCES 97

LIST OF FIGURES

Figure 1.1 Conceptual picture of hairpin eddy model. 2
Figure 2.1 Normalized JPDF of u'^+ and v'^+ and the contours of probability weighted Reynolds shear stress in the second quadrant. 7
Figure 2.2 Scenarios showing the arrangement of the two eddies in the initial condition. 9
Figure 2.3 Different initial conditions represented by the iso-surface of the square of local swirling strength. 12
Figure 2.4 Contours of low-speed streaks for different cases. 15
Figure 2.5 Merging and auto-generation of two-eddy case Ia for $\Delta x^+ = 118$. 16
Figure 2.6 Merging and auto-generation of two-eddy case Ia for $\Delta x^+ = 235$. 17
Figure 2.7 Influence of stream-wise spacing. 18
Figure 2.8 Temporal evolution of swirling strength for cases IV and V and their baseline simulations. 20
Figure 2.9 Modified auto-generation mechanism described using the generation of a new vortex in case Ia for $\Delta x^+ = 59$. 22
Figure 2.10 The front and top view of the channel showing the low speed streak and iso-contours at time $t^+ = 28.8$ for the two eddy case $(76, 51)$ 23
Figure 2.11 Two-dimensional schematic of auto-generation mechanism. 26
Figure 3.1 A hairpin packet in a fully developed turbulent channel flow at $Re_\tau = 180$. 31
Figure 3.2 Vector plots of velocity showing auto-generation in xy plane. 32
Figure 3.3 Top view of the generation of a new vortex E3 from vortex E2 with time $t^+ = 4.5,\ 6.75,\ 9.0,\ 11.25,\ 13.5$ and 15.75. . . 34
Figure 3.4 The 2-d contour plot of two vortices E3 and E2. 35
Figure 4.1 Average shear-layer structure extracted from a channel flow. 38
Figure 4.2 A vortex packet in a fully developed turbulent channel flow at $Re_\tau = 180$. 40

Figure 4.3 Coordinate systems of the flow (xyz) and the shear-layer structure ($\boldsymbol{\lambda}_i$). 42
Figure 4.4 Joint PDF of dissipation and the angle between the $\boldsymbol{\lambda}_2$ direction and the span-wise direction (z). 43
Figure 4.5 Instantaneously extracted shear-layer structure in planes $\lambda_2 = 0$, $\lambda_1 = 0$, and $\lambda_3 = 0$. 45
Figure 4.6 Vector plot in plane $\lambda_2 = 0$ of the extracted shear-layer structure from a vortex packet. 47
Figure 4.7 Time series of auto-generation in the intermediate eigenvector plane $\lambda_2 = 0$ of the extracted shear-layer structure. . . . 48
Figure 5.1 Burgers' vortex in a Cartesian coordinate system. 56
Figure 5.2 Shear-layer structure[7] extracted from the isotropic turbulent flow. 57
Figure 5.3 Node-saddle topology obtained by symmetrizing the shear-layer structure. 59
Figure 5.4 Projection of 5000 particles on the $\lambda_2 = 0$ plane of shear-layer structure at time $t = 0$. 61
Figure 5.5 The comparison of the evolution of the mean square of relative separation for different structures. 64
Figure 5.6 Comparison of the compensated relative dispersion for the shear-layer structure, node-saddle topology, and actual isotropic turbulence. 65
Figure 5.7 Evolution of 5000 particles in the shear-layer structure with time in different planes. 67
Figure 5.8 Evolution of 5000 particles in the node-saddle topology with time in different planes. 68
Figure 5.9 The distribution of particles in the shear-layer structure projected on the plane $\lambda_2 = 0$ at times $t/\tau_\eta = 4, 8, 10$, and 25. 69
Figure 5.10 Material lines: Comparison of the probability density function of $cos(\mathbf{l}, \mathbf{e}_i)$ at $t/\tau_\eta = 4.0$. 70
Figure 5.11 Tetrad dispersion: The comparison of the eigenvalues (g_i) of the inertia matrix with time. 73
Figure A.1 Comparison of mean stream-wise velocity (u^+) along the channel height. 84
Figure A.2 Comparison of root mean square velocities along the channel height. 85

Figure A.3 Comparison of root mean square velocity and mean shear stress along the channel height. 86
Figure A.4 Comparison of Reynolds shear stress and total stress along the channel height. 87
Figure B.1 Auto-generation in turbulent channel flow at $Re_\tau = 180$: Example 1 90
Figure B.2 Auto-generation in turbulent channel flow at $Re_\tau = 180$: Example 2 91
Figure B.3 Auto-generation in turbulent channel flow at $Re_\tau = 180$: Example 3 92
Figure B.4 Auto-generation in turbulent channel flow at $Re_\tau = 180$: Example 4 93
Figure B.5 Example vortex packet 1 containing two vortices ‘E1’ and ‘E2’. 94
Figure B.6 Example vortex packet 2 containing four vortices ‘E1’, ‘E2’, ‘E3’ and ‘E4’. 94
Figure B.7 Vector plot in the plane $\lambda_2 = 0$ of the extracted shear-layer structure from the example vortex packet 1 and 2. 95

LIST OF TABLES

Table 2.1 Overview of the simulations of the cases with two eddies . . 13
Table 2.2 Overview of simulations of the cases with a low-speed streak along with a eddy. 14
Table 3.1 Time taken to generate new vortex for four examples shown in Appendix B.1. 34
Table 4.1 Details utilized to compute the JPDF of dissipation and the angle between the $\boldsymbol{\lambda}_2$ direction and the span-wise direction (z). 43
Table A.1 Comparison of the simulation parameters in the present DNS and Lee and Moser[51]. 84

NOMENCLATURE

DNS	direct numerical simulation
TBL	turbulent boundary layer
TCF	turbulent channel flow
LSE	Linear stochastic estimate
x, y, z	Stream-wise, wall-normal and span-wise directions
u, v, w	Stream-wise, wall-normal and span-wise velocities
h	Half channel height
Re_τ	Friction Reynolds number
Re_λ	Taylor's Reynolds number
Re_Γ	Reynolds number based on circulation
δ'	δ velocity fluctuation
δ^+	δ is non-dimensionalized in wall units
$\langle\delta\rangle$	Mean of a quantity δ
$\|\delta\|$	Norm of a quantity δ
$-\langle u'v'\rangle$	Reynolds shear stress
u_τ	Friction velocity
Q2	Second quadrant ($u' < 0$, $v' > 0$)
Q4	Fourth quadrant ($u' > 0$, $v' < 0$)
λ_{ci}	Local swirling strength
$\mathcal{S}$	Local swirling strength squared

η	Kolmogrov length scale
τ_η	Kolmogrov time scale
t_B	Batchelor's time scale
SLS	shear-layer structure
NST	node-saddle topology
BV	Burgers' vortex

1

INTRODUCTION

Turbulence in fluid flows plays an important role in many natural and industrial processes. For instance, turbulence is a major contributor to drag in the flow over solid surfaces, it assists in the transport of pollutants, and it enhances chemical mixing and combustion. Hence, turbulence modification may help in reducing the drag to create energy efficient designs or assist in effective pollutant dispersion strategies. However to modify turbulence, it is necessary to understand the mechanisms behind it in detail.

Many different approaches are used to study and understand turbulence. They include the description of turbulence using, coherent structures[1, 2], flow topologies[3–7], and universal features of turbulence, namely, invariants of the velocity gradient tensor[6] and vorticity strain interactions[8]. In last few decades, due to the improvements in experimental and computational resources and techniques, it has become easier to study turbulence in three-dimensions. This is an important development as the full description of turbulence requires time dependent three-dimensional data because the turbulence is essentially three-dimensional, i.e, it cannot exist in two-dimensions. In the present thesis, turbulence will be mainly studied in terms of three-dimensional coherent structures.

The hairpin packet model[1, 9] is one of the descriptions of wall-bounded turbulence based on coherent structures. The structures in this model are considered important as they are associated with Reynolds shear stress, which is further connected to the drag. In various drag reduction techniques, the Reynolds shear stress or ejection events were observed to be suppressed[10–21]. Hence for drag reduction, it is important to understand the generation of Reynolds shear stress $(-\langle u'v' \rangle)$[1] or ejection events $(u' < 0,\ v' > 0)$. Thus, studying the dynamics of structures in the hairpin packet model is beneficial as it could open up some new insights to improve drag reduction.

---

[1] u' and v' refer to perturbation velocities in stream-wise and wall-normal directions, respectively.

The *hairpin packet model* was proposed by Adrian et al.[1] to describe wall-bounded turbulence and is illustrated in Figure 1.1. In this model, the vortices, such as hairpins or cane-shaped vortices, are clustered in a packet in the stream-wise direction (flow direction). The model is based on observations in actual wall-bounded turbulent flows[1, 22, 23]. The vortices in a packet are at an angle γ with respect to the wall and together they form a low momentum zone[1]. The consecutive vortices in the packet are separated in the stream-wise direction by $100 - 150$ wall units[1, 24]. The packets are observed to carry a significant amount of Reynolds shear stress, i.e., around 25% by only occupying 4.5% of the total area[9, 25]. Additionally, the conditional averaged flow around an ejection event reveals hairpin like vortices[9, 26–29], which further highlights the connection between Reynolds shear stress and the vortex packets. The existence of packets has been explained in terms of auto-generation, where a parent vortex generates new off-spring vortices[28, 30, 31]. The generation of new vortices is also associated with the generation of new ejection events[28]. Hence, understanding the generation of vortices or ejection events in a packet is important for the drag reduction problem.

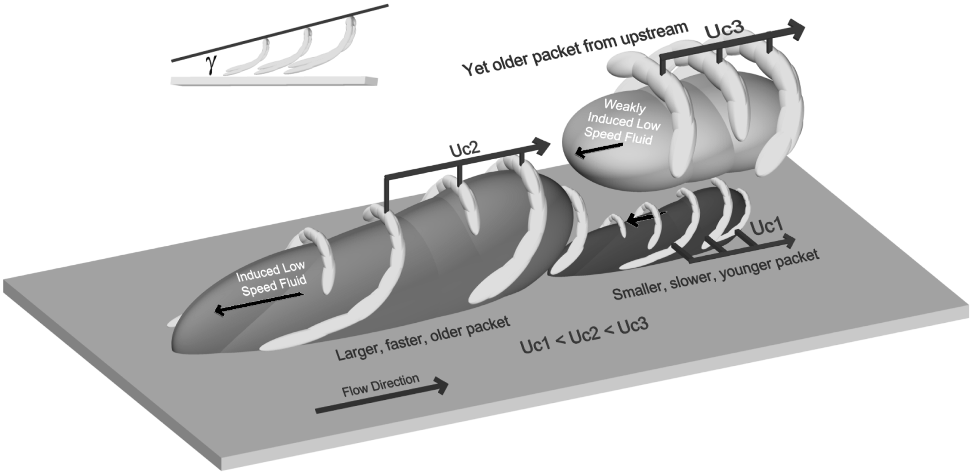
γ
Yet older packet from upstream
Uc3
Weakly Induced Low Speed Fluid
Uc2
Uc1
Induced Low Speed Fluid
Smaller, slower, younger packet
Larger, faster, older packet
Uc1 < Uc2 < Uc3
Flow Direction

FIGURE 1.1: Conceptual picture of hairpins/canes organization in wall bounded turbulence (Taken from Adrian et al.[1])

The auto-generation mechanism has been studied numerically in idealized simulations by Zhou et al.[28], Eitel-Amor et al.[32] and Kim et al.[33], where the evolution of an initial (or parent) hairpin superimposed onto a laminar background flow was simulated in time. In these simulations, the initial vortex was extracted from the actual turbulent flow by conditional averaging the flow around ejection events. Furthermore, the turbulent mean profile was used as the laminar background flow. It has been shown that the auto-generation of new vortices is only possible, if the initial vortex strength was above a threshold strength[28, 33] (see also Section 2.2). However, there was no explanation on how these threshold strength vortices could come into existence.

As already mentioned, the ejection events are associated with the generation of vortices in a hairpin packet[1, 9, 28]. The ejection events or the generation of new vortices are observed to be suppressed in many drag reduction studies. On the other hand, the generation of new vortices is desired for turbulence generation in the case of flow separation delay[34, 35]. Understanding the time required to create ejection events or vortices could assist in improving these active drag reduction and flow control techniques. However, there are no observations of auto-generation in actual turbulent flows, except for a recent experimental study[36]. Moreover, the timescale associated with auto-generation[9] may be different in actual turbulent flow compared to the idealized simulations[28, 32, 33]. Hence, the auto-generation and the time scale of the generation of a vortex in actual turbulent channel flow (TCF) is studied in this thesis.

The hairpin packets and the auto-generation in actual TCF were identified visually in this thesis as well as in many other studies. This is due to the lack of an objective identification method. An automated objective method to identify hairpin packets in turbulence data-sets could assist in studying and answering questions related to the statistical relevance of hairpin packets and auto-generation. In order to develop such an objective method, it is necessary to improve and generalize the understanding of the hairpin packets. This can be done by exploring connections between the hairpin packets and flow topologies in turbulence. In this thesis, we explore the connection between a general flow topology, called the shear-layer structure (SLS)[7], and hairpin packets, which could aid in improving the identification method.

Three-dimensional turbulence consists of many structures, namely, vortices, shear-layers and low-speed streaks. These structures can influence the transport of tracer particles in different ways. In two-dimensional turbulence, Goto and Vassilicos[37] showed that the straining regions or hyperbolic critical points tend to separate particles, thereby increasing the distance between them. On other hand, particles were observed to remain together in vortical structures or elliptical critical points. Further, they utilized this information to predict the temporal evolution of the particle pair dispersion statistics, which can be used in dispersion models. However, such a study in fully three-dimensional turbulence does not exist because of the numerous difficulties. Hence, dispersion around three-dimensional idealized structures with similar critical points will be studied in this thesis.

1.1 OBJECTIVES

Based on the discussion in previous paragraphs, the objectives of the thesis are to address the following questions

1. How do threshold strength vortices come into existence in wall-bounded turbulence?
2. Do we observe auto-generation in actual turbulent channel flow?
3. What is the time scale of auto-generation in actual turbulent channel flow?
4. What is the connection between the shear-layer structure and the hairpin packet?
5. What is the contribution of idealized structures in the turbulent dispersion statistics of tracer particles?

The first question is addressed by numerically exploring the interaction of two weak non auto-generating vortices in Chapter 2. The procedure followed is similar to that of Zhou et al.[28]. This chapter was published as 'Auto-generation in wall turbulence by the interaction of weak eddies'[38]. In Chapter 3, the hairpin packets and auto-generation are visually identified in an actual fully developed turbulent channel flow, where the second and third objectives are discussed. Next, it is known that the shear-layer structure consists of two co-rotating vortices and similarly, the hairpin packet also consists of a sequence of co-rotating span-wise vortices. Hence, a link between these two will be explored in Chapter 4, where the hairpin packets are identified in a fully developed turbulent channel flow. In Chapter 5, the tracer particles are simulated around different idealized three-dimensional structures, such as a shear-layer structure, a node-saddle topology and a Burgers' vortex. The dispersion statistics, namely pair dispersion, tetrad dispersion, and material line statistics, will be computed and compared with actual turbulent flow statistics. All these chapters can be viewed as standalone chapters as they are either published or papers in preparation. Finally, conclusions are briefly discussed in Chapter 6 along with implications and recommendations for the future study.

2

AUTO-GENERATION IN WALL-TURBULENCE

In this chapter, how threshold strength vortices that auto-generate can come into existence is explored. This is done by studying the interactions between two weak vortices or a weak vortex with a low-speed streak. Based on the observations, a modified auto-generation mechanism is proposed. This chapter has been published in Physics of Fluids with title 'Auto-generation in wall turbulence by the interaction of weak eddies'[38] and is presented here with few minor modifications.

2.1 INTRODUCTION

In most engineering applications, we come across loss of energy/momentum in turbulent flows over solid surfaces, such as flow over a car or over the wings of an aircraft. It is desired to decrease this loss of energy when creating more efficient designs. Numerous drag reduction techniques studied in the literature[10–21] have shown that the Reynolds shear stress, ejection events, stream-wise, or span-wise vortices decrease. Understanding how and why there is a decrease in these quantities could help in improving drag reduction. Hence, it is essential to study the internal structure and detailed dynamics of wall-bounded turbulent flows. Among many different approaches to investigate and understand the dynamics of turbulence, coherent structures is considered in this chapter.

One school of thought on the organized coherent structures[2, 9] is the hairpin eddy model in which the turbulent flow near a wall is populated by arch-type or hairpin-like vortices[9]. The initial generation of such hairpins in transitional boundary-layer flows has been studied by Brandt and Lange[39]. In fully developed turbulent flows the hairpin vortices have been observed to be clustered into so-called hairpin packets[1, 23, 40], which can be considered as a group of stream-wise aligned hairpin vortices, around a single low-momentum region. The vortices within these packets are separated by 100-150 wall units[1, 24] in the stream-wise direction. Due to their connection to the low-momentum regions, hairpin packets are associated with turbulent kinetic energy, and as discussed by Adrian[9] and Ganapathisubramani et al.[25], they carry significant Reynolds shear stress. Moreover, conditional vaveraging around Reynolds shear stress event reveal hairpin packet kind of topologies[9, 28], which again suggests hairpin type structures contribute importantly to the Reynolds shear stress. While other vortical structures may exist near the wall[41, 42], the close association of hairpin packets with the Reynolds shear stress makes them particularly relevant to the turbulent drag problem. It therefore becomes of interest to understand how packets come into existence.

The auto-generation mechanism[28] or parent-offspring concept[30] provides a possible explanation for this packet formation. In general, these mechanisms feature an initial vortex, which produces additional upstream vortices[28, 31]. The detailed explanation on how a new vortex is generated has been subjected to debate[28, 30, 31, 43–45]. Asai and Nishioka[44] conjectured the creation of new vortices is due to the inflectional instability of a wall shear layer lifted by the initial hairpin vortex legs. Their assessment was based on smoke-wire visualization and hot-wire measurements of boundary layer transition over a flat plate. On the other hand, Bake et al.[45] argued that vortex interactions are the main reason behind auto-generation rather than the shear layer after examining periodic Klebanhoff transition on a flat plate experimentally and by a direct numerical simulation. The mechanism based on vortex dynamics was further elucidated by Zhou et al.[28]. They came up with a simple model to demonstrate the auto-generation by numerical simulations of turbulent channel flow. Starting from a single, three-dimensional vortex structure they studied its subsequent development. The initial vortex is the part of a conditional eddy, which, corresponds to the average velocity field around an ejection (Q2) event $(u' < 0, v' > 0)$. The term 'eddy' here refers to the vortex structure along with the velocity field around it. The subsequent dynamics were explained in terms of the induced motions of the vortex forming a kink in the legs of the initial hairpin, which start to approach each other causing the associated shear layer to strengthen and roll-up into a span-wise vortex. The rolled-up span-wise vortex connects to the legs, thereby creating the secondary vortex.

Zhou et al. also found that the conditional eddy only auto-generates new vortices upstream when the vortex strength is above a certain threshold value. Kim et al.[33] further demonstrated the robustness of this auto-generation mechanism by showing the generation of new vortices even in the presence of added noise, and a turbulent flow field. They also observed that the added background noise resulted in a reduc-

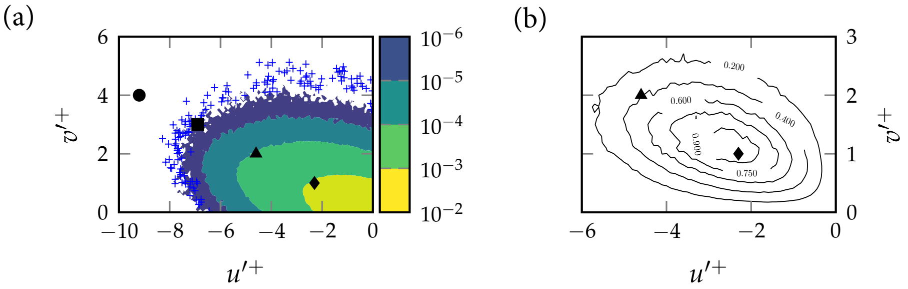

FIGURE 2.1: (a) Normalized joint probability density function ($f_{u'v'}$) of u'^+ and v'^+ in the second quadrant at $y^+ = 51$. The scatter plot in the figure is used to show the extreme low occurrence events. (b) The contours of probability weighted Reynolds shear stress given by $-u'^+v'^+f_{u'v'}$ at $y^+ = 51$. Markers ♦, ▲, ■, and ● in both figures correspond to relative strength $\alpha = 1,\ 2,\ 3,$ and 4, respectively.

tion of the threshold strength required to trigger auto-generation, though mainly in the buffer layer. However, the conditional eddy that was introduced into the fully developed turbulent channel flow and finally resulted in auto-generation had very large values of velocities ($u',\ v'$) compared to the observed values in actual turbulent flows. The relative strength α which linearly amplifies the conditional eddy, and thereby the magnitude of the ejection event on which it is based, was found to be 6 in their case. The precise definition of α will be discussed in Sec. 2.2. They increased α to get values of the swirling strength comparable with the actual turbulent flow vortices. However, our simulations indicate that $\alpha = 4$ already results in velocity values which are above the extreme values found in actual turbulent channel flow, as shown in Fig. 2.1. The probability of occurrence of velocity values at $\alpha = 3$ is even below 10^{-6} (see Fig. 2.1). The velocities corresponding to strength $\alpha = 2$ occur much less than the occurrence of velocities corresponding to $\alpha = 1$. The relative strength values of $\alpha = 2,\ 3$ were considered as the threshold strength for auto-generation in Zhou et al. On the contrary, in the present study values of $\alpha = 1$ are considered as it is of interest to consider scenarios involving weaker initial eddies, which are much more frequent in wall-bounded turbulence.

Therefore, in the first part of this study, how a threshold strength vortex may come into existence is explored by considering the interaction and possibly the merging of two weak initial eddy structures. Weak eddy structure means that it is below the threshold strength and does not auto-generate by its own. Adrian et al.[1] suggested that different vortex packets can merge. The merging of entire clusters of vortices was also described by Lozano-Durán and Jiménez[2]. Merging of individual vortices was also observed in experiments[46]. Adrian et al.[29] showed the growth of span-wise scales by studying the span-wise merging, growth and the interaction of hairpin vortices. However, the span-wise merging was reported to result in weaker, not stronger vortices. Therefore, it cannot be the origin of threshold strength vortices. Parthasarathy[47] studied multiple vortex interaction; however all the vortices under consideration were above threshold strength vortices. Based on these observations, the interactions between two ideal non auto-generating eddies in the stream-wise direction are considered in this chapter. The eddies are extracted from a fully developed channel flow simulation similar to that of Zhou et al.[28], which is discussed in detail in sections 2.2.2 and 2.2.3. A variety of scenarios are then created based on different initial strengths, different initial sizes and different initial stream-wise spacings between the aligned eddies as shown in Fig. 2.2. The role of these quantities in the auto-generation mechanism is studied to understand their influence on the onset of auto-generation.

In the second part of this study, the role of low-speed streaks on the onset of auto-generation is investigated. Low-speed streaks can affect auto-generation as they are sandwiched between the legs of the vortex in a conditional eddy[28]. So, when two eddies are aligned behind each other as shown in Fig. 2.2, their low-speed streaks get superimposed and thereby strengthen (shown later in Fig. 2.4). In order to understand the effect of low-speed streaks in auto-generation, a divergence-free low-speed streak is added to a non auto-generating conditional eddy and is studied for the generation of new vortices.

In the final part, critical aspects leading to onset of auto-generation are identified and a modified interpretation of the auto-generation mechanism[28, 44] is also presented. This interpretation for auto-generation is different from Zhou et al.[28] at later stages of the development where it views shear layer deformation instead of vortex dynamics. Also, in Zhou et al.[28], a symmetric hairpin vortex with two legs was used to explain the auto-generation mechanism, which is not often found in actual turbulent flows[42]. Zhou et al.[28] later added that the non-symmetric initial hairpins also auto-generated hairpin packets. These packets are more complicated, but bear resemblance with the idealized symmetric case, showing long low-momentum zones and similar growth angles. Thus, the stages involving the mutual interaction and self-induction by the two legs, as in the model of Zhou et al.[28], do not seem critically important. Hence, a stronger emphasis is laid on the role of the interaction of the hairpin with the background flow field.

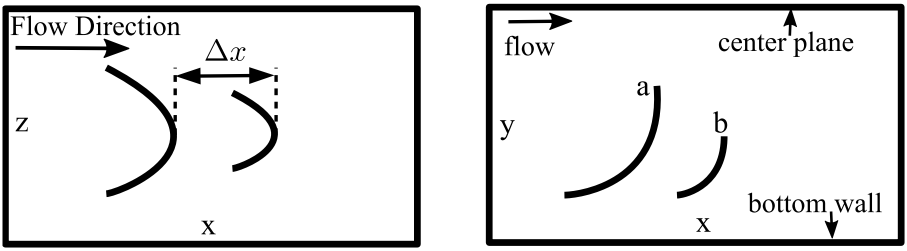

FIGURE 2.2: Scenarios showing the arrangement of the two eddies in the initial condition. The left figure shows a top view and the right figure a side view of the channel. Δx is the stream-wise distance between the two vortices. In this example, the upstream vortex 'a' is of higher event (y_e) location and the downstream vortex 'b' is of lower y_e location.

2.2 METHODOLOGY

2.2.1 *Numerical Method*

The dynamics of the eddies was simulated by Direct Numerical Simulation (DNS) in a channel flow driven by a constant pressure gradient. The pressure-correction method was used to solve the Navier-Stokes equations, where, the pressure distribution was only computed in the velocity corrector step in order to satisfy the constraint of a divergence free flow field (mass conservation). The explicit third-order Runge-Kutta scheme was employed for integration in time for advection and diffusion terms. And for spatial discretization, a pseudo-spectral (FFT-based)[48] method was used for the stream-wise (x) and span-wise (z) directions and a 6^{th} order compact finite-difference scheme[49] for the wall-normal direction (y). Periodic boundary conditions were applied in the horizontal directions and no-slip, no-penetration conditions at the solid walls. The computational domain was fixed to $4\pi h \times 2h \times \frac{4}{3}\pi h$ in the x, y and z directions with $192 \times 129 \times 128$ grid points, respectively. The uniform grid spacing was 11.78 and 5.89 wall units in the stream-wise and the span-wise direction respectively. A non-uniform grid[50] was used in the wall-normal direction, where Δy^+ varied from 0.75 near the walls to 3.87 in the core of the channel. The superscript $^+$ refers to scaling in viscous wall units. The velocities in the stream-wise, wall-normal and span-wise directions are given by u, v, w or $u_i = u_1, u_2, u_3$ and the superscript $'$ on them represent perturbation velocities relative to the mean flow $U(y)$. The DNS code is validated by comparing the turbulent statistics at friction Reynolds number $Re_\tau = 180$ to the data provided on website http://turbulence.ices.utexas.edu/[51]. This comparison is presented in appendix A.2. It should be noted that the Reynolds number considered in the present simulations is low. This is because the underlying mechanisms were shown to be similar and robust at higher Reynolds number by Kim et al.[33]. Additionally, fewer number grid points at low Re_τ gives us an opportunity to perform large number of simulations in small time and eases the data analysis in three-dimensions with time.

2.2.2 *Conditional eddy*

The initial condition at the start of a simulation is the superposition of the turbulent mean flow $U(y)$ and a perturbation velocity $\tilde{u}_i'$ associated with a conditional eddy. The turbulent mean flow was considered due to the high shear rate near the wall, which plays a role in the auto-generation[9]. The individual conditional eddy was extracted from a DNS of fully developed turbulent channel flow at $Re_\tau = 180$ by the means of linear stochastic estimation (LSE) of the flow field associated with an ejection event ($u' < 0$, $v' > 0$) identical to Zhou et al.[28]. This initial condition was simulated by the DNS method introduced in section 2.2.1. The pressure was not required to be initialized in the DNS, as the initial condition was found to divergence-free flow field. The LSE approximates[27] the conditionally averaged flow field given by $\langle \mathbf{u}'(\mathbf{x}) | \mathbf{u}_\mathbf{e}'(\mathbf{x}_\mathbf{e}) \rangle$ where $\mathbf{u}_\mathbf{e}'(\mathbf{x}_\mathbf{e})$ represents the velocity event vector conditioned at point $\mathbf{x}_\mathbf{e}$.

This LSE procedure has been extensively discussed in papers by Adrian[26, 27] and is given by

$$\begin{aligned} \tilde{u}_i{}'(\mathbf{x}) &= \text{Linear estimate of } \langle \mathbf{u}'(\mathbf{x}) | \mathbf{u}_\mathbf{e}'(\mathbf{x}_\mathbf{e}) \rangle \\ &= \sum_{j=1}^{3} L_{ij}(\mathbf{x}, y_e) u_{j,e}' \quad i = 1,2,3 \end{aligned} \tag{2.1}$$

where L_{ij} are linear estimate coefficients and $u_{j,e}'$ is the velocity event vector located at a wall-normal distance y_e. The coefficients L_{ij} are computed from unconditional two-point correlations according to

$$\sum_{j=1}^{3} \langle u_k'(\mathbf{x}_e) u_j'(\mathbf{x}_e) \rangle L_{ij} = \langle u_i'(\mathbf{x}) u_k'(\mathbf{x}_e) \rangle, \quad k = 1,2,3. \; i = 1,2,3. \tag{2.2}$$

where $\langle u_k' u_j' \rangle$ and $\langle u_i' u_k' \rangle$ represent the unconditional two-point co-variances between the velocities at $\mathbf{x}_e$, and between the fluctuating velocity field and the velocity at $\mathbf{x}_e$ respectively. In equation (2.2), the correlations only depend on y_e, y, and the relative distances Δx, Δz with respect to the event as x, z are homogeneous directions in the flow. Hereafter the relative distances Δx and Δz are simply represented as x and z respectively unless stated otherwise.

The velocity event vector $u'_{j,e}$ (see Eq. 2.1) was chosen such that it matched to the value of the second quadrant (Q2) event ($u' < 0, v' > 0$) which contributes most to the Reynolds shear stress ($-\langle u'v' \rangle$) at a particular wall-normal location (y_e^+). That is, the values of $u_e = u'$, $v_e = v'$ which maximizes $|u'v'|f_{uv}(u',v')$ in the second quadrant, where $f_{uv}(u',v')$ represents the joint probability density function of occurrence of u' and v'. The span-wise component w'_e was zero resulting in symmetric conditional eddy as shown in Fig. 2.3a. The vortex is visualized by iso-surfaces of the square of local swirling strength[28] given by $\mathcal{S} = \lambda_{ci}^2$ which is used for vortex identification throughout this chapter. The local swirling strength is defined as the imaginary part of a complex eigenvalue (λ_{ci}) of the velocity gradient tensor. If all the eigenvalues are real then the local swirling strength is zero. The values of the maximum swirling strength of the eddy conditioned at $y_e^+ = 51$ was found to be comparable with the reported values in Zhou et al.

2.2.3 *Simulation types*

Two of such conditional eddies were added to the turbulent mean flow $U(y)$ to study their interaction. The initial velocity field at the start of the simulation was given by

$$\tilde{u}_i(\mathbf{x}) = U(y) + \alpha\tilde{u}'_i(x,y,z;y_{e1}) + \beta\tilde{u}'_i(x+\Delta x,y,z;y_{e2}) \tag{2.3}$$

where α and $\tilde{u}'_i(x,y,z;y_{e1})$ are the relative strength and the perturbation velocity of the first eddy corresponding to the event at y_{e1}, and similarly the relative strength β, and perturbation velocities $\tilde{u}'_i(x+\Delta x,y,z;y_{e2})$ of the second eddy are based on the event at y_{e2} with an additional stream-wise shift (Δx) relative to the first eddy. The stream-wise shift is approximately the distance between the stream-wise locations of the maximum swirling strength of the eddies at time ($t^+ = 0$). Therefore Δx will be referred to as distance between two eddies throughout the chapter. Figure 2.3b shows an example of an initial condition containing two vortices computed from equation (2.3). An overview of all the two-eddy cases studied is given in table 2.1. Similar simulations[47] were performed previously, where the eddies considered were above the threshold strength and could auto-generate into new vortices individually. The values of the relative strength α, β listed in table 2.1 correspond to cases where eddies do not auto-generate individually as it is aimed in the present chapter to study below threshold strength eddies. The stream-wise spacing between the vortices (Δx) was chosen comparable to the observed spacing of 100-140 wall-units in experiments[1, 24, 46]

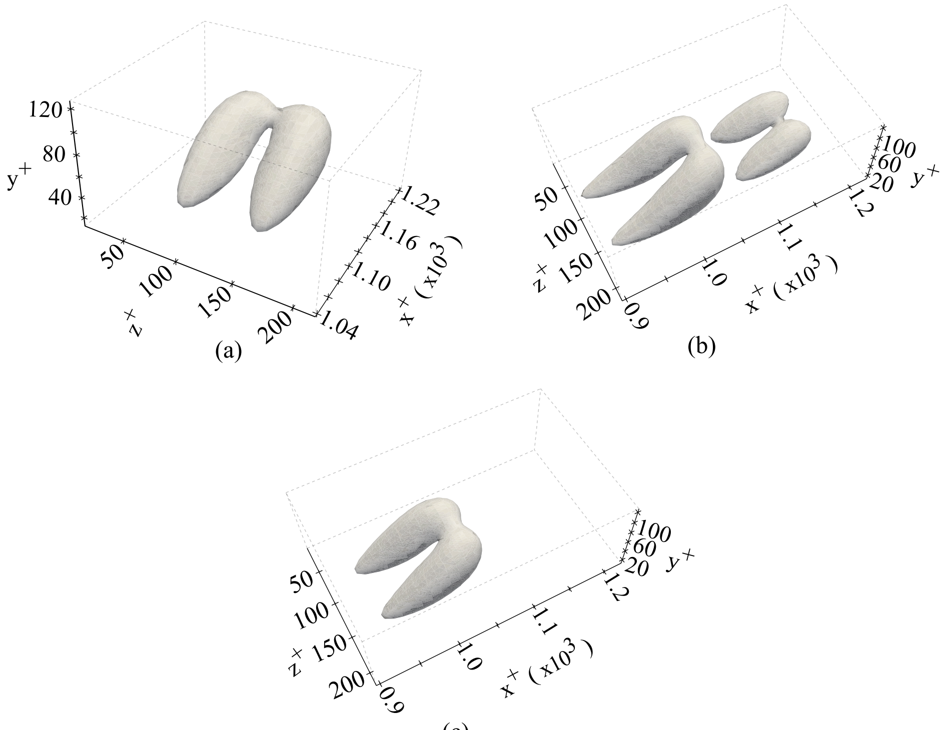

(a) (b)

(c)

Figure 2.3: Different initial conditions represented by the iso-surface of the square of local swirling strength $\mathcal{S}^+ = \lambda_{ci}^{+2} = 3.86 \times 10^{-4}$ (approximately 20% of maximum $\mathcal{S}^+$). (a) Single eddy case with event location $(y_e^+ = 76)$ and relative strength of conditional eddy $(\alpha = 1)$. (b) Two eddy case, upstream vortex with $(y_e^+ = 76, \alpha = 1)$ and downstream vortex $(y_e^+ = 51, \alpha = 1)$. (c) Low-speed streak superimposed (Eq. (2.4)) on an eddy $(y_e^+ = 76, \alpha = 1)$. It looks very similar to the single-eddy case $(y_e^+ = 76, \alpha = 1)$.

and below to study vortex-vortex interactions. Reference event planes (y_e) were considered in the outer layer and all event locations were between 0.1h to 0.3h in the wall normal direction. Case I and II simulations in table 2.1 represent a taller upstream vortex compared to the downstream vortex and vice-versa in case III. In cases I and III both eddies have the same relative strength whereas the upstream eddy in case II has a higher relative strength than the downstream eddy.

In the second part of this study, the interaction of a single conditional eddy with a low-speed streak is examined. To obtain the streak, the stream-wise velocity component in a cross-stream plane was extracted from the velocity field of a conditional eddy $\tilde{u}_i$ (section 2.2.2). The extracted plane is at a stream-wise distance x_p relative

TABLE 2.1: Overview of the simulations of the cases with two eddies. 'NA' or 'Not Applicable' refers to cases where the initial vortices have already merged with each other. Case Ib and Ic, and case IIa and IIb are together as they have similar merging and auto-generation behavior for all Δx^+. Auto-generation is decided visually based on whether new vortices are generated when iso-surfaces at all time steps are drawn at 10% of the square of maximum initial swirling strength.

Case	Strength $(\alpha,\ \beta)$	Ref Plane (y^+_{e1}, y^+_{e2})	Spacing Δx^+	Merging	Auto-generation
Ia	(1,1)	(76,51)	59	NA	Yes
			118	Yes	Yes
			177	Yes	Yes
			235	Yes	No
Ib		(103, 51)	59	NA	Yes
			118	Yes	No
Ic		(103, 76)	177	Yes	No
			235	Yes	No
IIa	(2,1)	(103, 51)	59	NA	Yes
			118	Yes	Yes
IIb		(103, 76)	177	Yes	Yes
			235	Yes	Yes
III	(1,1)	(76, 103)	59	NA	Yes
			118	No	Yes
			177	No	No
			235	No	No

to the event location $\mathbf{x}_e$. The streak is created by expanding this cross-stream plane uniformly in the x-direction. Hence the stream-wise derivative is zero. Furthermore, because $u_2 = u_3 = 0$, the streak is also divergence free and does not contain any vortex. Mathematically, the initial field containing one eddy and the streak is given by

$$\tilde{u}_i(\mathbf{x}) = U(y) + \alpha \tilde{u}'_i(x, y, z; y_{e1}) + \beta \tilde{u}'(y, z; y_{e2}, x_p) \tag{2.4}$$

where $\tilde{u}'(y, z; y_{e2}, x_p)$ corresponds to the stream-wise velocity at a plane x_p extracted from a conditional eddy conditioned to the event at y_{e2}, and β defines the relative strength of the streak as it linearly amplifies the velocities.

TABLE 2.2: Overview of simulations of the cases with a low-speed streak along with a eddy.

Case	Eddy		Low-speed streak		
	Event plane (y_e^+)	Strength (α)	Event plane (y_e^+)	Strength (β)	Spacing (x_p^+)
IV	76	1	51	1	59
V	76	1	76	1	0.0

An overview of all the vortex-streak simulations is shown in table 2.2. Case IV is obtained by removal of the second, downstream vortex in the two eddy case Ia with $\Delta x^+ = 59$ (see Table 2.1) and replacing it with a low-speed streak. This low-speed streak was obtained from the original downstream eddy in case Ia ($y_{e2}^+ = 51$). It was the plane that overlapped with the peak swirling strength of the upstream eddy (i.e., $x_p^+ = 59$). The streak is illustrated in Fig. 2.4. The contours of the low-speed streak for cases I, IV, and the single eddy cases of $y_e^+ = 76$ and 51, as well as the plane x_p for case IV are shown in the figure. Case V is created to compare with the single eddy case of $y_e^+ = 76$ with $\alpha = 2$. The low-speed streak was extracted from single eddy $y_e^+ = 76$ with $\beta = 1$ at plane $x_p^+ = 0$ and overlapped with the conditional eddy corresponding to the same event location and relative strength ($\alpha = 1$). The iso-surface of the square of swirling strength of this initial condition (case V) is shown in Fig. 2.3c. It is very similar to the single-eddy case of 76 with $\alpha = 1$ (Fig. 2.3a). However the strength of the low-speed streak is doubled. The two eddy case Ia with $\Delta x^+ = 59$, and the single eddy case of 76 with $\alpha = 2$ are the baseline cases, which are used to compare with the cases IV and V respectively.

2.3 RESULTS AND DISCUSSION

2.3.1 *Two-eddy case*

The interaction between the two individually non auto-generating eddies was studied to understand how above threshold strength vortices may come into existence. This was done by placing two non auto-generating eddies behind each other aligned in stream-wise direction (see section 2.2.3) and checking for auto-generation. Zhou

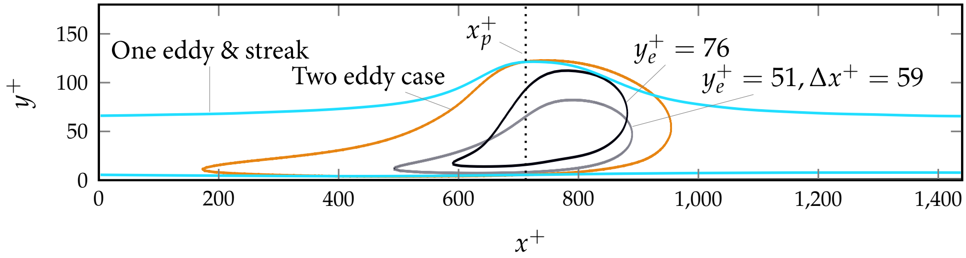

FIGURE 2.4: Contours of low-speed streaks at $u'^+ = -1.0$. Black and green contours represent two individual eddies of relative strength $\alpha = 1$ at $y_e^+ = 76$ and 51. Two eddy case with eddies $(76, 51)$ and $\alpha = (1, 1)$ is given by red contour and blue contour corresponds to superposition of plane x_p^+ of $y_e^+ = 51$ on eddy $y_e^+ = 76$ as given in Eq. (2.4).

et al.[28] described auto-generation as the means of generating new hairpin vortices from a parent hairpin vortex. In the present case, auto-generation is loosely referred to as the creation of new structures irrespective of whether these structures are hairpins or a pair of counter-rotating stream-wise vortices. An overview of the two-eddy cases studied is given in table 2.1. It is important to emphasize that all eddies shown in the table do not auto-generate individually, which was confirmed in separate simulations of the single eddies. Moreover, the single-eddy evolution was studied to set up a baseline for studying the interaction between two eddies. The initial conditional vortex is a pair of lifted, counter-rotating stream-wise vortices (Fig. 2.3a). Zhou et al.[28] report the following important observations connected with the evolution of a single eddy, which are confirmed by our simulations. All studied conditional vortices evolve into a hairpin vortex, which is referred to as the primary hairpin vortex[28]. If it has sufficient initial strength, i.e., above a threshold strength, then it auto-generates. A conditional vortex with a higher swirling strength (or higher relative strength α) travels slower than a weaker vortex at the same event location (y_e^+). A conditional vortex based on an event specified at higher event vector location (y_e^+) travels faster for the same swirling strength due to higher mean flow velocity at larger wall normal location (y^+)[28].

Returning to the two eddy cases, Fig. 2.5 shows an example of two vortices merging to form a single vortex (Fig. 2.5a-2.5b). This merged vortex subsequently auto-generates new vortices as shown in Fig. 2.5c. As mentioned the two initial eddies do not auto-generate individually, i.e., they are all below the threshold strength required for auto-generation. Hence merging of *weak* vortices seems a viable concept to produce *stronger* vortices that do auto-generate. Table 2.1 lists the outcomes of the other two eddy simulations in terms of whether or not merging and auto-generation are observed. Two vortices separated by a stream-wise distance of $\Delta x^+ = 59$ were found to be merged already in the initial field for all the cases shown in table 2.1 and hence merging is indicated in the table as not applicable (NA). Merging was observed for the cases I and II where the upstream vortex was at a higher event location compared to the downstream vortex. When the upstream vortex was at a lower event location compared to the downstream vortex, like in case III, merging did not occur. In cases I and II, the upstream vortex moved faster than the downstream vortex due to its higher location, reducing the distance between them with time and finally resulting in merging. From the single-eddy case, it was already known that an vortex with higher y_e^+ travels faster than an vortex with lower y_e^+, due to increasing mean flow velocity with y^+. After merging the geometric shape of the structure remained broadly similar to a hairpin vortex. In case III, the downstream vortex travels faster and moves away from the upstream vortex hence they do not merge.

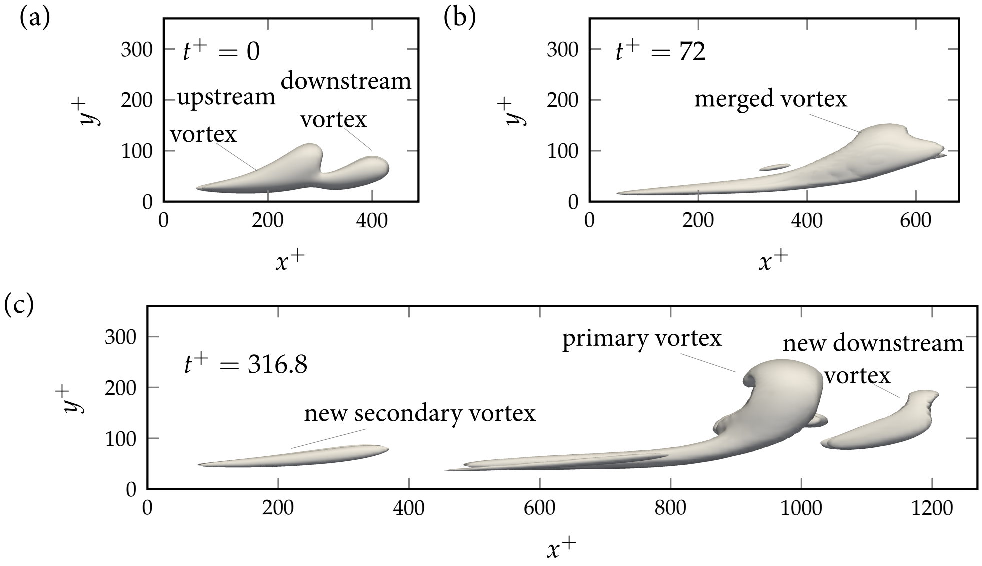
(a)
$t^+ = 0$
upstream vortex
downstream vortex
y^+
x^+
300
200
100
0
0
200
400
(b)
$t^+ = 72$
merged vortex
y^+
x^+
300
200
100
0
0
200
400
600
(c)
$t^+ = 316.8$
primary vortex
new downstream vortex
new secondary vortex
y^+
x^+
300
200
100
0
0
200
400
600
800
1000
1200

FIGURE 2.5: Iso-contours of the swirling strength squared $\mathcal{S}^+ = 1.64 \times 10^{-4}$ (10% of maximum initial $\mathcal{S}^+$) for the two-eddy case Ia with $\Delta x^+ = 118$ (side view). In these plots x^+ is indicative of the size of the vortices rather than the distance travelled by them. (a) Two vortices at time $t^+ = 0$. (b) At time $t^+ = 72$, the two initial vortices have merged to create a single vortex. (c) The merged vortex auto-generates one upstream and one downstream vortex at $t^+ = 316.8$.

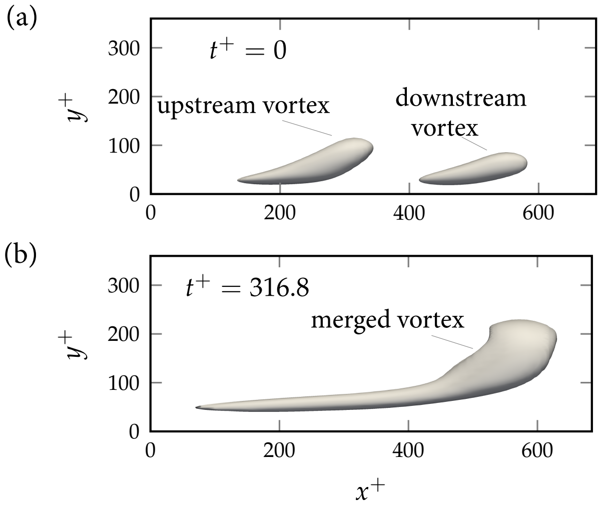

FIGURE 2.6: Iso-contours of the swirling strength squared ($\mathcal{S}^+ = 1.64 \times 10^{-4}$) of the two-eddy case Ia with $\Delta x^+ = 235$. In these plots x^+ is indicative of the size of the vortices rather than the distance travelled by them. (a) Two vortices at time $t^+ = 0$. They merge at time $t^+ = 144$. (b) At time $t^+ = 316.8$, the merged vortex does not auto-generate.

Auto-generation does not occur in all the simulations with vortex merging as indicated in table 2.1. Figures 2.5 and 2.6 represent examples of an auto-generation and a non auto-generation case, respectively. In both simulations, the initial eddies were of unit strength ($\alpha = \beta = 1$) with the upstream eddy conditioned on $y_e^+ = 76$ and the downstream eddy on $y_e^+ = 51$ (case Ia, table 2.1). The only difference was in the stream-wise separation (Δx^+). For $\Delta x^+ = 118$, the two vortices (Fig. 2.5) merge after $t^+ = 72$ to form a single vortex. Then at time $t^+ = 316.8$, this merged vortex generates two new vortices, one upstream and one downstream as shown in Fig. 2.5c. Merging is also observed for the larger stream-wise separation distance $\Delta x^+ = 235$ at $t^+ = 144$ (Fig. 2.6a). The development of this merged vortex at time $t^+ = 316.8$ can be seen in Fig. 2.6b. It did not generate any new vortices and slowly dissipated with time. Similar cases where the auto-generation did not occur for large stream-wise separation can be found in table 2.1. This is because, as the separation distance increases, the time till merging increases as well. During this time, the strength of the vortices decay resulting in weaker vortices at the time of merging, hence a weaker interaction.

These interactions for different stream-wise spacing can also be quantified in terms of the vortex strength. The strength of the vortex at an instant in time is defined as the maximum of the swirling strength squared, which is normalized by means of its initial

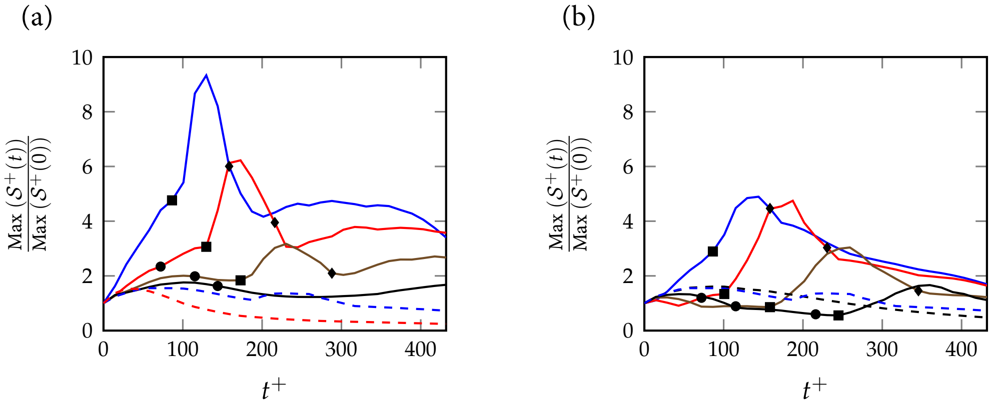

Figure 2.7: Influence of stream-wise spacing on temporal evolution of normalized square of swirling strength : Lines (——), (——), (——) and (——) indicate stream-wise spacing $\Delta x^+ = 59, 118, 177,$ and 235, respectively. Lines (- - -), (- - -) and (- - -) represent individual eddies at event vector location $103, 76,$ and 51, respectively. Filled square (■) represents a shift in the peak location from the leg to the head, whereas black diamonds (⧫) represents a shift from the head to the legs. Black bullets (•) represents the time when merging is complete, which is visually decided (e.g., Fig. 2.5b). (a) Case Ia, with single eddies $y_e^+ = 76$ & 51. (b) Case Ic, with single eddies $y_e^+ = 103$ & 76.

value (at $t^+ = 0$). The evolution of the two-eddy cases Ia with different stream-wise separations are shown in Fig. 2.7a along with the individual eddies at $y_e^+ = 76$ and 51 of strength $\alpha = 1$ for comparison. Similarly, Fig. 2.7b represents cases Ic along with individual eddies at $y_e^+ = 103$ and 76. In these figures, the square of the initial maximum swirling strength ($\mathcal{S}^+(0)$) in two eddy and single eddy cases were found to be comparable to within 10% and therefore, it is used for normalization. The resulting normalized value represents the amplification of vortex strength compared to the initial state. At first the peak in swirling strength is located in the leg of the vortex then as the vortices merge and the hairpin shape develops, the peak location shifts to the hairpin head. This transition is indicated in Fig. 2.7 by the marker (■). After a while the swirling strength in the head starts to decrease and the peak in swirling strength returns to the legs, which is marked by (⧫) in Fig. 2.7. The marker (•) represents the time when merging is complete, which is visually decided (e.g., Fig. 2.5b).

In Fig. 2.7a, it is observed that the initial growth rate (increase in vortex strength with respect to time) is much steeper for a stream-wise spacing of $\Delta x^+ = 59$ than for $\Delta x^+ = 118$. With increased spacing the growth rate decreases and around $\Delta x^+ = 235$, it becomes similar to the single eddy cases. The peak amplification, i.e., the value of normalized maximum swirling strength squared, follows a similar trend. It reaches 9.33 for $\Delta x^+ = 59$ compared to 6.22 for $\Delta x^+ = 118$, and it continues to decrease as the stream-wise spacing is increased. The peak amplification of 9.33 in case Ia is about six times the value of 1.55 for the single eddy case with $y_e^+ = 76$. The two vortices thus temporarily produce a much stronger merged vortex (for $\Delta x^+ \leq 118$), which is above the threshold strength for auto-generation. Whereas individually, the vortices remain below the threshold strength and eventually get dissipated[28]. When the stream-wise distance between the vortices is higher, the time required to merge is longer, and during this time the vortices weaken individually. And when these weak vortices merge, the merged vortex is not strong enough to generate new vortices. Similar observations can be made in Fig. 2.7b, where again the peak amplification decreases as the stream-wise spacing is increased.

The peak amplification is also found to increase when the distance between the two eddies in the wall-normal direction is decreased. The upstream eddy for both cases Ib and Ic is conditioned at $y_e^+ = 103$, however the downstream eddy was conditioned at $y_e^+ = 51$ for case Ib and $y_e^+ = 76$ for Ic. The peak amplification in case Ic was found to be 4.89 (see Fig. 2.7b) compared to 3.14 for case Ib with stream-wise spacing $\Delta x^+ = 59$. A similar trend of higher peak amplification was observed in case IIb compared to IIa, where the downstream eddy in case IIa was conditioned at lower y^+ than case IIb.

In cases IIa and IIb (see Table 2.1), where the stream-wise spacing was higher, i.e., $\Delta x^+ = 235$, the merged vortex did auto-generate even though the stream-wise spacing between the two vortices was large for vortex-vortex interaction. This was due to the higher initial strength of the eddy, though it was still below threshold strength.

From all these observations, it can be inferred that stream-wise merging results in the creation of a stronger vortex whose subsequent auto-generation may still depend upon the initial strength of eddies and their stream-wise spacing. The strength of the initial eddies (α and β) required for auto-generation in the cases I was around unity, which corresponds to an eddy conditioned on a commonly occurring ejection event. This is clearly lower than the threshold strength of a single eddy required for auto-generation[28]. However, auto-generation was also observed in cases where merging did not occur (see case III, table 2.1). This clearly indicates that vortex merging is not the only mechanism that can trigger auto-generation. It was also found that the auto-generation occurred in non-merging cases in the present study when the stream-wise spacing was lower than 118 wall units. From these observations, it can be educed that the stream-wise separation (Δx^+) between eddies plays a major role in auto-generation. However, the initial stream-wise separation cannot be identified

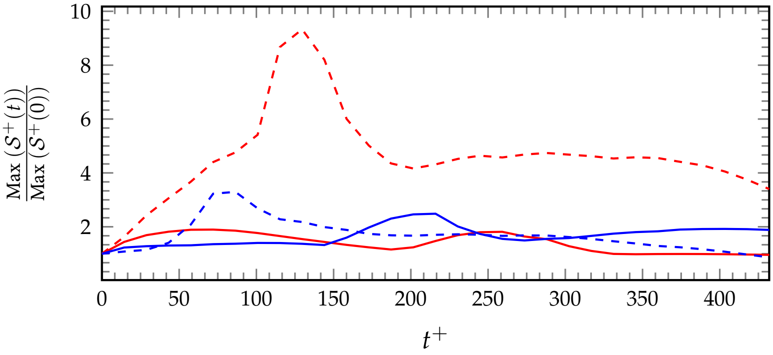

FIGURE 2.8: Temporal evolution of normalized maximum swirling strength. Lines (——) and (- - -) refer to case IV and its baseline simulation (case I (76,51), $\Delta x^+ = 59$). Lines (——) and (- - -) refer to case V and its baseline simulation (single eddy $y_e^+ = 76$ and $\alpha = 2$).

as the sole parameter to define the onset of auto-generation, as auto-generation also depends upon the strength of the eddies in our simulations. The initial strength α was used as a quantity to define the onset of auto-generation in Zhou et al.[28]. However, in the present investigation below threshold strength eddies were considered and still new structures were generated when the stream-wise spacing was sufficiently small. This may be because when two eddies are placed near to each other their fluctuating velocity fields get superimposed onto each other and amplified, which is similar to an increase in threshold strength where the velocity field is linearly amplified. The magnitude of the superimposed fluctuating velocity at a given spatial location decreases with the increase in stream-wise separation between the two eddies (see Fig. 2.4). So, threshold strength and stream-wise spacing (Δx^+) are both related to the velocity field. A quantity defining the velocity field, like ejection events or low-speed streaks, may thus be used to define the onset of auto-generation.

2.3.2 *Role of low-speed streaks*

An extracted conditional eddy consists of a vortex on top of a low speed streak. So when two conditional eddies are superimposed, their low-speed streaks are also superimposed. In order to separate the effect of overlapping low-speed streaks, an extracted low-speed streak is superimposed under a conditional eddy and simulated to check for the generation of new vortices. In order to create a low-speed streak, the vortex was removed from a conditional eddy as described in section 2.2.3. The streak was then added to a conditional eddy as shown in equation (2.4). An overview of the simulations is given in table 2.2. Neither case IV nor Case V revealed any signs of auto-generation. Figure 2.8 represents the temporal evolution of the normalized maximum swirling strength of cases IV and V along with the baseline cases where auto-generation occurs. It was observed that adding a low-speed streak did not cause an increase or amplification of the maximum normalized $\mathcal{S}^+$ in contrast to the baseline cases that included a vortical structure in the second eddy. From this, it is inferred that the overlapping of the low-speed regions (in the two eddy cases) is not the main cause of the subsequent auto-generation.

From the above, it is inferred that vortex-streak interactions do not explain auto-generation, hence cannot be used to predict the onset of auto-generation. As the ejection events are used to extract the conditional eddy, their role in the auto-generation mechanism is studied in a more detailed way in Subsection 2.3.3.

2.3.3 *A modified interpretation of the auto-generation mechanism*

The auto-generation mechanism proposed by Zhou et al. is based on vortex dynamics where self and mutual induction play an important role. In the following, a modified description of auto-generation especially concerning the onset of the formation of the secondary hairpin vortex is proposed. I will not only consider vortex induction, but also put a stronger emphasis on the environment of the primary hairpin. After all, the initial eddy does not only contain a hairpin vortex but also the imprint of its surrounding structures that are statistically important. The modified interpretation of creating new vortices utilizes the ideas of shear-layer instabilities conjectured by Asai and Nishioka[44]. In the following paragraphs, this will be discussed in detail.

Figure 2.9 illustrates the evolution of the two eddy case Ia with the stream-wise separation of $\Delta x^+ = 59$. The vectors in the plot are scaled to unit length, hence only indicating the flow direction. This aids in better visualization of the shear layer roll-up. Figure 2.9a-e were plotted for time $t^+ = 28.8$, 57.6, 86.4, 158.4, and 244.8, respectively.

The initial development can be explained from figure 2.9a. The vortex is contained within a low speed region, which is clearly larger and taller than the vortex itself[1, 52] (see Fig. 2.10). This large size region can play a role in the auto-generation mechanism, and is not explained by induction of a single hairpin. Assuming the initial stages of development as largely passive, meaning advection of the vortex is by the local velocity, it is seen from Fig. 2.9a that the wall-normal velocity is large in point 'A2', i.e., the head as compared to point 'A1' in the legs. Consequently, the head lifts away from the wall faster than the legs, which is indeed observed (Fig. 2.9c-e). At the same time,

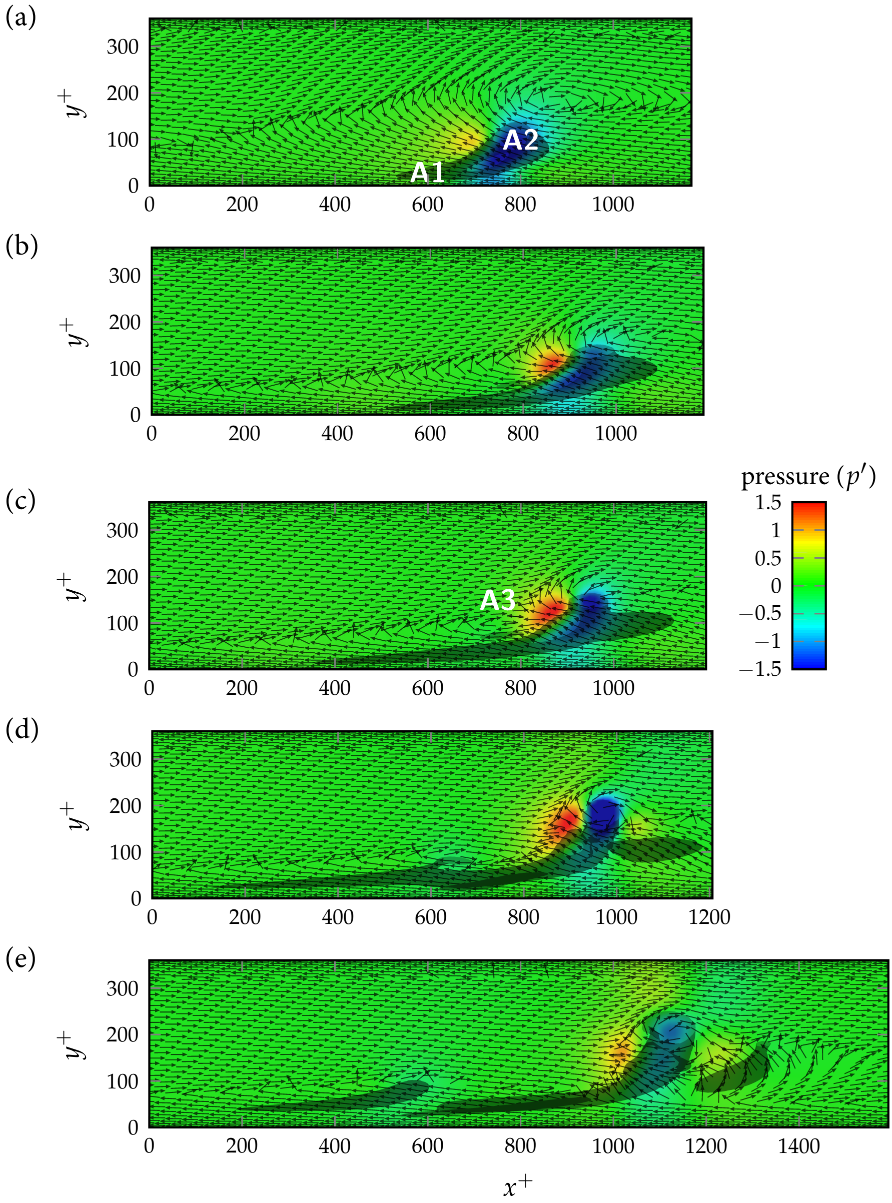

FIGURE 2.9: Auto-generation mechanism : Vector plots of velocity (u'^+, v'^+) along with non-dimensionalized pressure fluctuation ($p' = p/\rho u_\tau^2$) contours in the symmetry plane, which is between the two legs of a vortex. All vectors are scaled by unit length, and hence only indicate the flow direction. Vectors scaled by velocity magnitude are shown in Figure 3.2 for different auto-generation case. The iso-surfaces in the figures correspond to the 10% of the initial maximum swirling strength. This is for the two eddy case $(76, 51)$ at strength $\alpha = (1, 1)$ with $\Delta x^+ = 59$. Figures a-e represent the evolution of two eddies and vector plots in time (t^+) 28.8, 57.6, 86.4, 158.4, and 244.8 respectively.

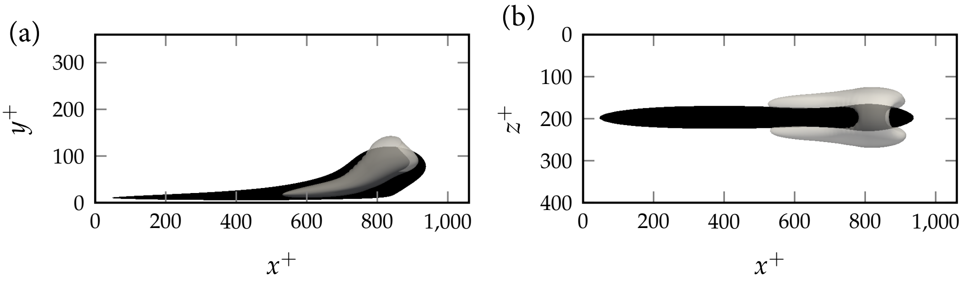

FIGURE 2.10: The front (a) and top (b) view of the channel showing the low speed streak ($u'^+ = -2.0$) in black under the iso-contours (grey) of local swirling strength (10% of the initial maximum). Figures are at time $t^+ = 28.8$ for the two eddy case $(76, 51)$ at strength $\alpha = (1, 1)$ with $\Delta x^+ = 59$.

the stream-wise velocity ($U + u'$) in 'A2' is higher compared to 'A1', which means the legs are stretched (Fig. 2.9b-e). The combination of these two effects is observed in Fig. 2.9b-e, where the angle of the legs near the head and the shear layer just upstream of the head grows steeper.

In Fig. 2.9a, a shear layer upstream of the initial hairpin vortex is visible at an angle with respect to the wall[1]. This occurs when the ejected fluid between the legs meets the incoming (high velocity) flow. After 28.8 wall time units, i.e., at $t^+ = 57.6$ (Fig. 2.9b), as the velocity at the location of the head is higher than the un-lifted part due to its higher y^+, the legs get stretched in the stream-wise direction and amplify (see Fig. 2.7). At the same time, the head of the vortex moves up in the wall-normal direction as discussed above and the swirling strength of the head increases. This increase in strength appears to be associated with the hairpin head approaching the shear layer where the velocity differences across the layer strengthen the roll-up (see Fig. 2.7). The stronger roll-up increases the vortex induced flow leading to a stronger ejection of the fluid between the legs near the head and a stronger self-induction[28] which lifts the head even further from the wall. Furthermore, the angle of the shear layer and the lifted stream-wise legs become steeper. With time, the hairpin head is lifted above the initial shear layer and starts to obstruct the incoming high velocity flow. This is indicated by high pressure region upstream of the head in Fig. 2.9c-d. Due to the blockage, a stagnation point in (u', v') is formed within the now heavily distorted shear layer upstream of the lifted primary hairpin. The stagnation point is associated with a local pressure peak which deflects incoming flow away from the hairpin head resulting in a local saddle point topology (labeled 'A3' in Fig. 2.9c). Most of the incoming flow is deflected up and over the primary hairpin head, but some fluid is pushed downward.

This downward flow interacts with the low speed flow underneath causing a roll-up of the shear-layer[44], which marks the birth of the secondary hairpin head Fig. 2.9c. The secondary hairpin head is observed to distort the legs and create a kink in them. The un-lifted legs just upstream of the primary hairpin head are pushed down as shown in Fig. 2.9d. This sequence is different from the interpretation given by Zhou et al. where the kinks in the legs develop *before* the new hairpin head is created. With time, as the new roll-up gets stronger, the upstream un-lifted legs of the stream-wise vortex gets attached to it. This attachment of head to the legs is a viscous process[28].

The stronger ejection with time lifts up the new secondary hairpin similar to the description of the points 'A1' and 'A2' in Fig. 2.9a. This causes the stream-wise vortex to lift up at the point of the new hairpin and the sweep events downstream of the new head push the stream-wise legs down towards the wall. This leads to the separation of the new vortex from the original stream-wise vortex (Fig. 2.9e). If the ejection events in the new leg are stronger then a third vortex is formed in a similar way or else it gets dissipated with time. A third vortex formation has also been observed between the old and the new vortex when the ejection in the leg of the old vortex is strong.

From the above observations, the auto-generation is summarized as the rapid lift up of a hairpin vortex that blocks the incoming flow leading to the roll-up of the shear layer creating a secondary vortex. The rapid lift up of the initial hairpin is identified to be a critical element in the onset of auto-generation. In the present simulations, the rapid lift up is observed in three scenarios: (i) a single beyond threshold strength vortex, (ii) merging vortices, and (iii) non-merging cases of below threshold strength vortices. In the first scenario, as the strength of a hairpin vortex is increased, its environment, i.e., ejection events become stronger. This along with the self-induction leads to the rapid lift up of the hairpin vortex. In the second scenario (Case I and II), two weak hairpin vortices merged to form a stronger hairpin. Also the ejection events at the beginning of the simulation were stronger due to the superposition of two vortices. The creation of a stronger vortex along with the enhanced ejection event leads to the faster lift up of a merged eddy. In the last scenario of the non-merging case of week vortices (case III), when the stream-wise spacing between eddies was sufficiently small, the ejection of fluid by the downstream vortex propelled the upstream vortex away from the wall. Also, similar to the merging case, the superposition of two eddies leads to the creation of a stronger ejection event. The combined effect lifts the upstream vortex away from the wall. So ejection events play a critical role in the rapid lift up of the vortex, which then interacts with the incoming flow to create a new hairpin.

In this new modified interpretation, two stream-wise vortices are not required to describe the lift up and further auto-generation, as is the case in Zhou et al. A single leg can lift up and block the incoming flow leading to shear layer roll up and creation of a new vortex (see Fig. 3.2 in Chapter 3). This is one of the advantages of the present interpretation as it does not rely on the presence of two stream-wise vortex legs which are not often found in actual turbulent flows[42]. It also further strengthens the existing hairpin eddy model[1].

2.4 CONCLUSIONS

In this chapter, it was explored how an above-threshold strength eddy may come into existence, the role of a low-speed streak in the onset of auto-generation, and also proposed a modified interpretation of the auto-generation mechanism. This was done by performing a series of direct numerical simulations of turbulent channel flow at $Re_\tau = 180$ with idealized initial conditions. The initial condition was the sum of the mean velocity profile at $Re_\tau = 180$ and the perturbation velocity corresponding to a conditional eddy extracted by LSE from fully developed turbulent channel flow data at the same Reynolds number.

The two non auto-generating conditional eddies were aligned behind each other in the stream-wise direction to study the interactions that lead to auto-generation. It was found that two vortices merged when an eddy conditioned at higher wall-normal location was placed upstream of the one conditioned at the lower wall-normal location. The vortex with higher wall-normal location moved faster due to higher mean velocity and merged with the downstream vortex. The maximum normalized square of swirling strength increased after merging. Hence, merging can lead to the creation of an above threshold strength vortex. However, all the merging cases did not auto-generate, only the cases with lower stream-wise separation auto-generated. As the initial distance between the vortices increased, merging took longer time, during which the vortices weakened individually, and hence the merged vortex was not strong enough to create new vortices. However, when the initial strength of the eddies was increased the merged vortex auto-generated even for larger stream-wise separations. From these observations, it is inferred that merging can create stronger vortices, but subsequent auto-generation may still depend upon initial strength or the initial stream-wise separation.

For small initial stream-wise separations, a few non-merging eddy cases also generated new structures. Merging was not possible in these cases as the downstream vortex convected faster than the upstream vortex, as it was conditioned at a higher wall-normal location compared to upstream vortex. Hence, merging is not the only mechanism to trigger auto-generation. The small stream-wise separation is identified as a quantity to play a role in the onset of auto-generation.

Zhou et al. used threshold strength in the initial condition to define the onset of auto-generation in single eddy cases. In the present case, where the two eddies were below threshold strength, auto-generation was found to depend largely on the stream-wise separation. The smaller stream-wise separation between eddies emulate increasing threshold strength as velocity fields in both cases got amplified. Hence, the role of the velocity field and specifically of the low-speed streak was explored for the onset of auto-generation. When the stream-wise separation was smaller, low-speed streaks from the two eddies got superimposed and amplified. A separate set of simulations were performed by adding a divergence-free low-speed streak to a conditional eddy to understand the influence of vortex-streak interactions on the auto-generation. These simulations did not result in any auto-generation or amplification of the normalized maximum swirling strength compared to the base line cases (Fig. 2.8).

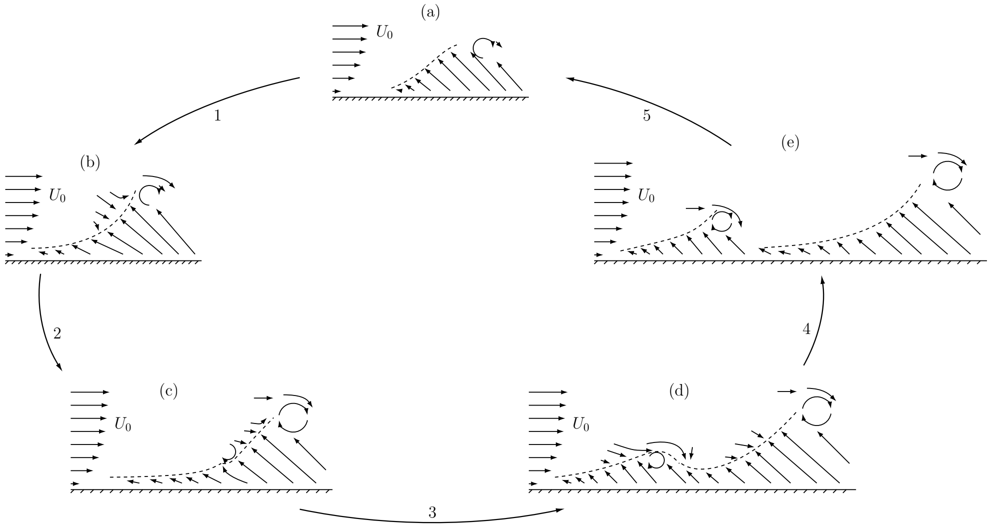

FIGURE 2.11: Two-dimensional schematic of auto-generation mechanism shown in Fig 2.9. Vectors indicate (u', v'), - - - - represents the shear-layer and U_0 indicates the mean flow. (a) Initial hairpin with a shear-layer. (b) Head of the hairpin lifts up rapidly blocking the incoming flow. Formation of a stagnation/saddle point forces fluid to move towards head or towards wall. (c) Fluid moving towards the wall deforms the shear-layer and initiates the shear-layer roll up. (d) Continued lift up of the initial hairpin head deforms the shear-layer further. At the same time, as the new roll-up strengthens, the fluid downstream is pushed down and the Q2 event upstream of the roll-up is enhanced. (e) The new hairpin vortex detaches form the original hairpin.

At the end, a modified interpretation of the auto-generation mechanism based on the ejection events and its interaction with the surrounding flow is presented. Inspection of the data suggests that a strong lift-up of the hairpin head by the ejection event coupled with a stream-wise vortex can lead to auto-generation as shown in Fig. 2.11. A stream-wise vortex with a small span-wise swirl, i.e., head (Fig. 2.11a), is rapidly lifted up by the ejection events. Due to lift up of the vortex head, the in-rushing flow is blocked (Fig. 2.11b). This inrush of flow and the already existing ejection events cause the shear layer to deform and roll-up in the span-wise direction just upstream of the vortex (Fig. 2.11c-d). As this span-wise roll-up becomes stronger, it connects to the leg/legs of the downstream vortex. With time, this becomes a new vortex and gets separated from the main vortex (Fig. 2.11d-e). If the ejection events are stronger in any of the two vortices, a third vortex will be formed in a similar way, else the vortices are dissipated over time. The generation of new vortices was also observed in experiments by Jodai and Elsinga[36] within a fully turbulent boundary layer in a similar way.

This modified mechanism differs from the existing mechanism by Zhou et al. where induced vortex motions result in formation of a kink in the legs of the initial vortex (Fig. 2.11d) before a new hairpin head is created. In other words, kink formation in Zhou et al. is due to mutual and self induction of stream-wise legs, whereas in the present mechanism, it is the consequence of the shear layer roll-up and ejection events. Also, the presence of two stream-wise vortex legs is not necessary to describe the onset of auto-generation as a single leg can lift up and block the incoming flow leading to the shear-layer roll up and further generating new vortex.

The implication of the present study is that commonly found weak vortices can also auto-generate, which further strengthens the existing hairpin eddy model[9].

3

TIME SCALE OF AUTO-GENERATION

In the previous chapter, auto-generation was studied by performing idealized simulations in a laminar background flow. Even though the auto-generation mechanism was proposed to explain the existence of hairpin packets in fully developed turbulent flow, it has not yet been observed in the direct numerical simulations of actual wall bounded turbulence. In this chapter, auto-generation along with its time scale is studied in turbulent channel flow.

3.1 INTRODUCTION

In the present day of depleting energy resources, it is necessary to decrease the energy loses in flows over solid surfaces, such as fluid transport in pipes or vehicle transport (e.g., motion of car/aircraft through a fluid). The energy loss is associated with the pressure drag and friction at the wall to which turbulence is a major contributor. Therefore, turbulence modification could be an effective drag reduction strategy. However, this modification requires understanding of the dynamics of turbulent flows. Furthermore, the study of the dynamics of turbulence also aids us in understanding the fundamental mechanism behind it.

The hairpin packet model[1] is one way to understand the dynamics of wall-bounded turbulence in terms of coherent structures. In this model, the boundary layer is populated by hairpin packets[22, 23] and each packet further consists of hairpin-like or arch/cane shaped vortices aligned in the stream-wise direction[1, 41]. These different vortices are considered to be from the same family of vortices[1]. Together, the aligned vortices enclose a low-momentum zone. Furthermore, these packets contribute significantly to the Reynolds shear stress (25%) while only occupying 4.5% of the total area[25]. The formation of a packet is explained by the auto-generation mechanism[28, 31], where a parent vortex generates a new vortex upstream[28]. This mechanism and its robustness have been shown in idealized simulations[28, 33, 38], where the evolution of a vortex superimposed on a mean laminar velocity field was studied. Moreover, the generation of the new vortical structure is associated with the generation of a new ejection event ($u' < 0, v' > 0$)[1][28, 38], which contributes to the Reynolds shear stress, hence, friction.

The ejection events are associated with a self-sustaining turbulent cycle and momentum transfer in wall-bounded flows[9]. Furthermore, these ejection events along with span-wise vortices are observed to be suppressed in the case of drag reduction[12, 17–20]. Hence, suppressing the hairpin packets could result in drag reduction as the generation of new vortices with ejection events is hindered. On the other hand, enhancing turbulence or packet formation can delay or prevent separation[34, 35]. To actively modify the generation of vortices and ejection events, it is important to know the associated time scale, that is, the time scale of the auto-generation cycle.

The time scale of auto-generation in the idealized simulations reported in Zhou et al.[28] and Goudar et al.[38] varies from $80 - 250$ time wall units. However, it has been suggested that the time scale of a new vortex generation depends on the instantaneous shear stress[9]. Hence in the present chapter, auto-generation in hairpin packets is studied in actual fully developed turbulent channel flow.

3.2 METHODOLOGY

In the present study, the hairpin packet and auto-generation were visually detected from the highly resolved direct numerical simulation (DNS) database of the fully developed turbulent channel flow at friction Reynolds number $Re_\tau = u_\tau h/\nu = 180$, where u_τ, h and ν represent the friction velocity, half channel height, and kinematic viscosity, respectively. The friction velocity u_τ is defined as $\sqrt{\tau_w/\rho}$, where, τ_w and ρ represent shear-stress at the wall and fluid density, respectively. The flow was driven by a constant pressure gradient and a pressure correction method was used to solve the Navier-Stokes equations. In this method, the pressure distribution was only computed in the corrector step to satisfy mass conservation. A pseudo-spectral method[48] was used to compute derivatives in stream-wise (x) and span-wise (z) directions, while a sixth order compact difference scheme[49] was used in the wall-normal direction (y). The third-order Runge-Kutta scheme was employed for integration in time. Periodic boundary conditions were enforced in the stream-wise and span-wise directions, and the no-slip and no-penetration boundary conditions were prescribed at the walls. The number of grid points was $384 \times 129 \times 192$ in a computational domain of $4\pi h \times 2h \times \frac{4}{3}\pi h$ in x, y, and z, respectively. A uniform grid spacing of 5.89 and 3.93 wall units was employed in the x and z directions, respectively, where, a wall unit or '$+$' unit is a non-dimensionalized scale constructed using u_τ and ν. And in the wall-normal direction, a non-uniform grid[50] was utilized where, Δy^+ varied from 0.75 near the wall to 3.87 wall units in the core of channel. Thirty velocity fields were stored at intervals of 2.25 time wall units ($t^+ = tu_\tau^2/\nu$). The DNS code utilized here is the same one as in the previous chapter except that the resolution in periodic directions is higher. The validation for this higher grid resolution is shown in appendix A.2. The vortices in this turbulent flow are visualized by the iso-surfaces of the square of the local swirling strength[28] given by $\mathcal{S} = \lambda_{ci}^2$. The local swirling strength is defined as the imaginary part of a complex eigenvalue (λ_{ci}) of the velocity gradient tensor. If all the eigenvalues are real, then the local swirling strength is set to zero.

---

[1] u' and v' refer to perturbation velocities in stream-wise and wall-normal directions, respectively.

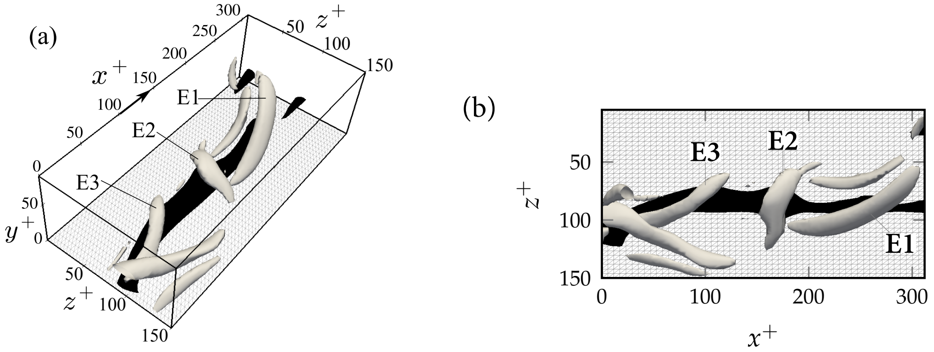

FIGURE 3.1: A hairpin packet containing three vortices in fully developed turbulent channel flow at a certain time $t^+ = 15.75$. Vortices (in gray) represent the iso-surface of the local swirling strength squared (5% of the maximum). The black iso-surface represents the low-speed streak at $u'^+ = -4$. 'E1' represents the downstream vortex, followed by upstream vortices 'E2' and 'E3', respectively. The arrow along x-axis in (a) represents the direction of the mean flow. The bottom wall of the channel is indicated by a wireframe.

3.2.1 *Identification of a vortex packet and auto-generation*

The hairpin packets were identified visually by inspecting the hairpin packet signatures in xz plane as described by Adrian et al.[1] and Ringuette et al.[53]. The local swirling strength was utilized to detect vortices (head of hairpins) in the xz plane. If the vortices

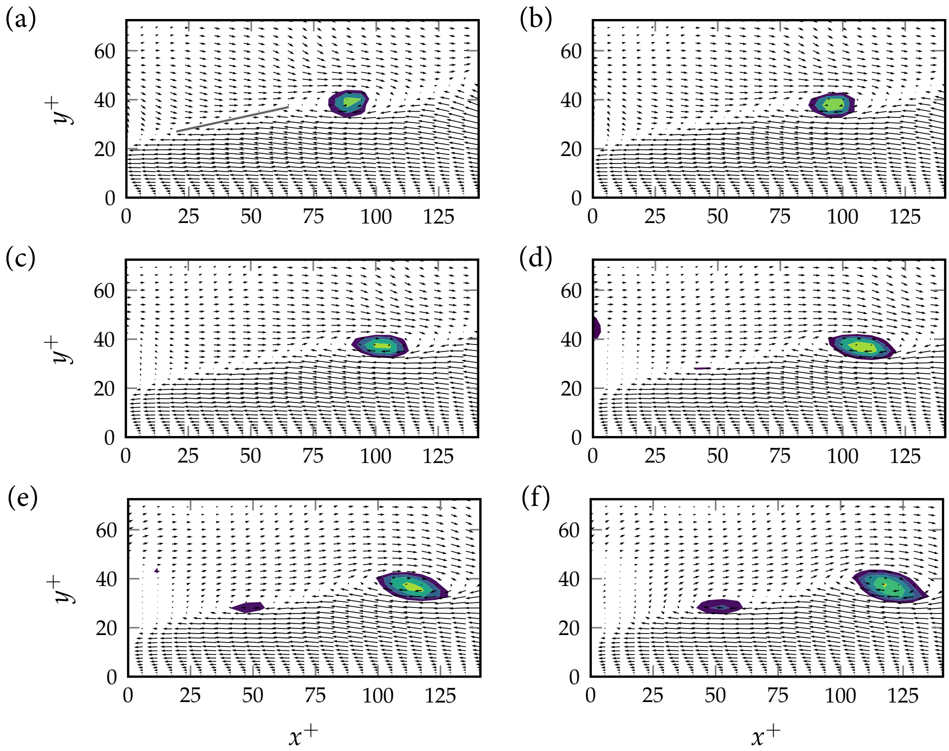

FIGURE 3.2: Auto-generation of vortex 'E3' in the vortex packet '(E1 E2)'. Vector plots of perturbation velocity (u'^+, v'^+) along with contours indicating $>$ 5% of the maximum local swirling strength squared $\mathcal{S}$. Figures a-f represent vector plots at times $t^+ = 0.0,\ 2.25,\ 4.5,\ 6.75, 9.0,$ and 11.25, respectively. The gray line in (a) refers to the straight shear-layer.

were grouped in the stream-wise direction and their distance from the wall increased in the downstream direction, then, it was identified as a hairpin packet. And one such packet is shown in figure 3.1.

Next, the auto-generation time scale is computed by tracking the first two upstream vortices in the packet back in time. The two upstream vortices '(E2 E3)' in Fig. 3.1 are traced back in time and are shown in Figure 3.2. The velocity vector plots along with the contours representing $>$ 5% of the maximum swirling strength squared $\mathcal{S}$ are plotted in the figures 3.2a-f. The most upstream vortex in figure 3.2f is 'E3' followed by 'E2' in the downstream. The final and initial time of the auto-generation is defined as follows. When the shear-layer upstream of vortex 'E2' (between $x^+ = 75 - 100$) is straight (see gray line in Fig. 3.2a), then, the time associated with it is defined as the start of auto-generation. With time, the shear-layer is observed to deform (see Fig. 3.2b-d). Here, it should be noted that the local swirling strength has a non-zero value at the curved shear-layers. Hence, threshold for $\mathcal{S}$ is fixed to 5% to eliminate contours showing curved shear-layers. Additionally, velocity vectors are plotted to accurately identify the time at which the new vortex comes into existence. This is observed in figure 3.2f at time $t^+ = 11.25$, where, the vector plots and swirling strength show the formation of vortex 'E3'. The time between the start and the end of the auto-generation essentially corresponds to the shear-layer roll-up, which is 11.25 time wall units in the Fig. 3.2.

3.3 RESULTS AND DISCUSSION

The search for packets was not extensive and a total of six packets with auto-generation were identified in 30 continuous flow fields separated by 2.25 time wall units each. Here only six packets are shown due to the difficulties associated with identifying packets and auto-generation. Among the six, only the hairpin packet shown in Figure 3.1 will be discussed in the present chapter and other four auto-generation cases are shown in section B.1. Figure 3.1 consists of three vortices at time $t^+ = 15.75$, where, the downstream vortex 'E1' is followed by vortices 'E2' and 'E3' upstream, respectively and these vortices lie above the low speed zone given by $u'^+ = -4.0$[2] (see Fig. 3.1a).

Figure 3.2 and 3.3 shows the generation of a new cane-shaped vortex 'E3' in two different planes. The mechanism of the generation of the vortex 'E3' is as follows. Initially, due to the ejection events under the vortex 'E2' a shear-layer is formed upstream (see Fig 3.2a). From figures 3.2b-d, shear-layer blocks the incoming flow from the outer region leading to its deformation. This along with the existing ejection event upstream of 'E2' leads to the shear-layer roll-up, which develops into the new vortex 'E3'. This mechanism is similar to the description of the auto-generation mechanism by Goudar et al.[38] for both symmetric and asymmetric vortices (see Chapter 2). Hence, this observation along with experimental observations[36] support the hairpin packet model proposed by Adrian et al.[1] and the auto-generation model by Zhou et al.[28].

The main objective of this study is to obtain the time associated with auto-generation, which was determined based on the above mentioned method. The time taken for the auto-generation shown in the Figure 3.2 was approximately 11.25 time wall units. Additionally, the time computed for the other five detected auto-generation cases was

---

[2] The superscript $'$ refers to the perturbation velocity.

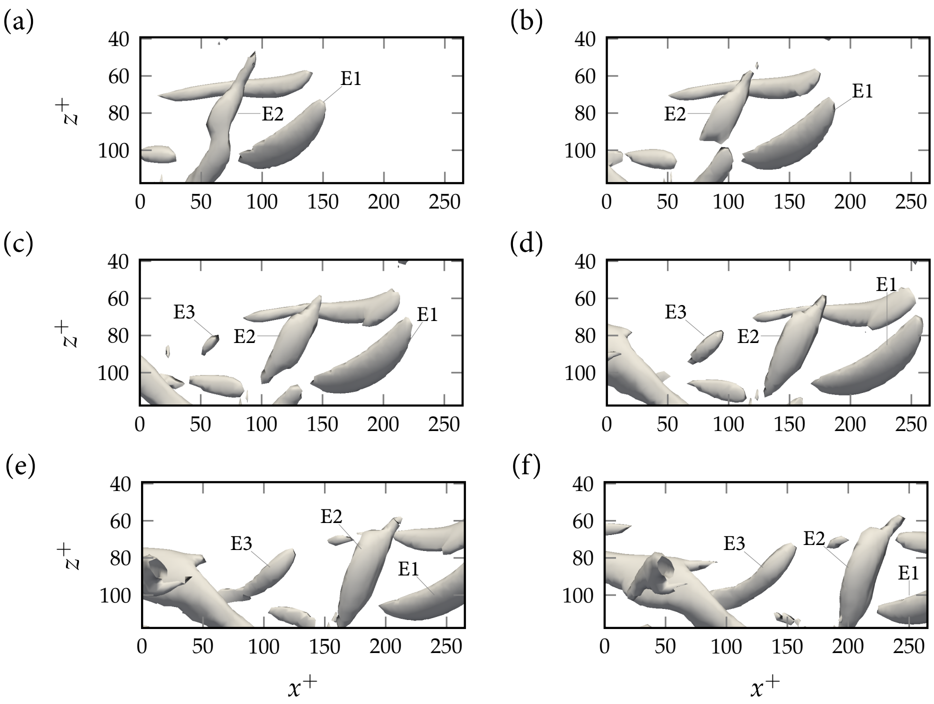

FIGURE 3.3: Top view of a small section of the turbulent channel flow domain showing vortices by the iso-surface of local swirling strength squared (5% of the maximum). Figures (a)-(f) show the generation of a new vortex 'E3' from the vortex packet '(E1 E2)'. The frames represent the relative times $t^+ = 4.5, 6.75, 9.0, 11.25, 13.5$ and 15.75, respectively.

between $11 - 18$ time wall units (see table 3.1). This time scale is about one half of the $20 - 30$ time wall units observed in the experiments of the turbulent boundary layer flow[36]. Also, it is an order of magnitude lower than the time reported in the idealized auto-generation simulations[28, 33, 38], which is $80 - 250$ time wall units.

TABLE 3.1: Time taken to generate new vortex for four examples shown in Appendix B.1.

	Example 1	Example 2	Example 3	Example 4
Time (t^+)	13.5	15.75	18.0	11.25

As mentioned above, the shear-layer roll-up upstream of a vortex in a packet develops into a new vortex. This shear-layer roll-up can be compared with vortex-sheet roll-up in a Kelvin-Helmholtz (KH) instability. In KH instability, there is velocity difference ΔU across the vortex-sheet, which is comparable to the velocity jump ΔU^+

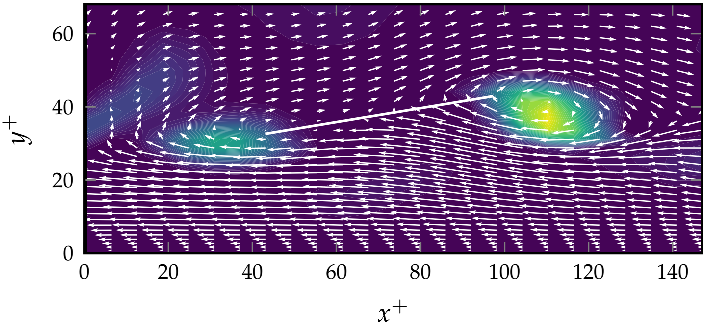

FIGURE 3.4: The 2-d contour plot of swirling strength showing the two vortices E3 and E2 (from left to right) in the hairpin packet shown in Fig. 3.1. The solid white line indicates the shear-layer.

across the shear-layer. By neglecting viscous and wall effects, time required to auto-generate a new vortex is compared to the time taken to form a vortex by vortex-sheet roll-up by Kelvin-Helmholtz instability. The predicted time for the vortex roll-up in an inviscid flow by Kelvin-Helmholtz instability[54] is given by

$$T^+ \approx 0.4 \times 2\lambda^+/\Delta U^+ \tag{3.1}$$

where $2\lambda^+/\Delta U^+$ refers to shear-layer characteristic time scale[55], λ^+ represents the wavelength or the distance between two adjacent vortices and ΔU^+ is the velocity difference across the sheet. Representative values for λ^+ and ΔU^+ are determined as follows.

Figure 3.4 shows the two vortices (E3,E2) in the stream-wise–wall-normal plane cutting through the center of a low-speed streak. The stream-wise distance between the vortices (E3,E2) is 75 wall units, which is taken as the wavelength λ^+. Typically, the distance between two vortices in packets is reported to be $100-140$ wall units[1, 24, 29] which is slightly higher than the present observation. The velocity difference ΔU^+ is defined based on stream-wise velocity component on either side of the shear-layer. As the vortices shown in Fig. 3.4 are above the low-speed streak defined by $u'^+ = -4.0$, the stream-wise velocity below the shear-layer is fixed to -4.0. Similarly, the stream-wise velocity above the shear-layer in Fig. 3.4 is found to be 1.5. This results in the velocity difference $\Delta U^+ \approx 5.5$. With these values, the time (T^+) required for KH vortex roll-up (Eq. 3.1) is 11 time wall units. Furthermore, using the reported vortex separation of $100-140$ wall units in the literature, assuming similar velocity difference ($\Delta U^+ = 5.5$), the roll-up time is around $14-20$ time wall units.

This estimated time scale for the vortex roll-up is close to the time scale of auto-generation observed in actual turbulent flows, i.e., $10 - 15$ time wall units. This suggests that the auto-generation maybe similar to the shear-layer roll-up. Additionally, this small time scale can explain how quickly a cluster of vortices is formed in a boundary layer, thereby, strengthening the hairpin packet model[1].

Here only six auto-generation events were considered. A full statistical study of the time scale of auto-generation and the number of vortices generated remains to be done. Such statistical study would benefit from an automated and more objective detection of packets and auto-generation, which will be explored further in Chapter 4.

3.4 CONCLUSION

To conclude, six hairpin packets along with auto-generation in a fully developed turbulent channel flow were shown. The time scale for the generation of a new vortex in a packet was observed to be $10 - 15$ time wall units. This time scale was consistent with the theoretical predictions for a Kelvin-Helmholtz instability, but was an order of magnitude lower than the existing estimates based on the idealized simulations of auto-generation. As the new vortex is associated with the growth of an ejection event, this time scale can be associated with the production of Reynolds shear stress, hence turbulent drag. Therefore, active flow control strategies aiming at generating turbulence or reducing drag are expected to be effective when forcing at this time scale.

4

THE TALE OF TWO CO-ROTATING VORTICES

The hairpin packets were visually identified in the previous chapter. However, an automated objective method could help in studying the statistical relevance of hairpin packets and to examine the time scale of auto-generation statistically. Hence to develop a new method, at first, a link between the instantaneous flow structures extracted from the vortex packets in turbulent channel flow and the average shear-layer structure is explored. Further, the dynamics of the extracted instantaneous flow structure is studied. With this information a new method to identify hairpin packets is proposed. This chapter is a proof of concept study, where, a link between hairpin packets and shear-layer structure is explored.

4.1 INTRODUCTION

The structure of turbulence has been studied in many different ways, for instance, in terms of coherent structures[1, 2], local flow topologies[3–7], the invariants of the velocity gradient tensor[6], and vorticity strain interactions[8]. With improved experimental and numerical tools and techniques in recent decades, a substantial progress has been made in different ways of understanding turbulence. However, the description of turbulence still remains incomplete, due to many unanswered questions in these different ways of understanding turbulence. One approach to solve these questions could be to link the different ways of studying turbulence, thereby creating a coherent view of what are the relevant fluid motions in a turbulent flow. For example, a connection between universal features, namely, vorticity-strain alignment and the PDF's of the velocity gradient tensor, and a coherent flow structure was established by Elsinga and Marusic[7].

Elsinga and Marusic[7] utilized the universal feature of the preferential alignment of vorticity with the intermediate eigenvector of the strain-rate tensor[8] to extract

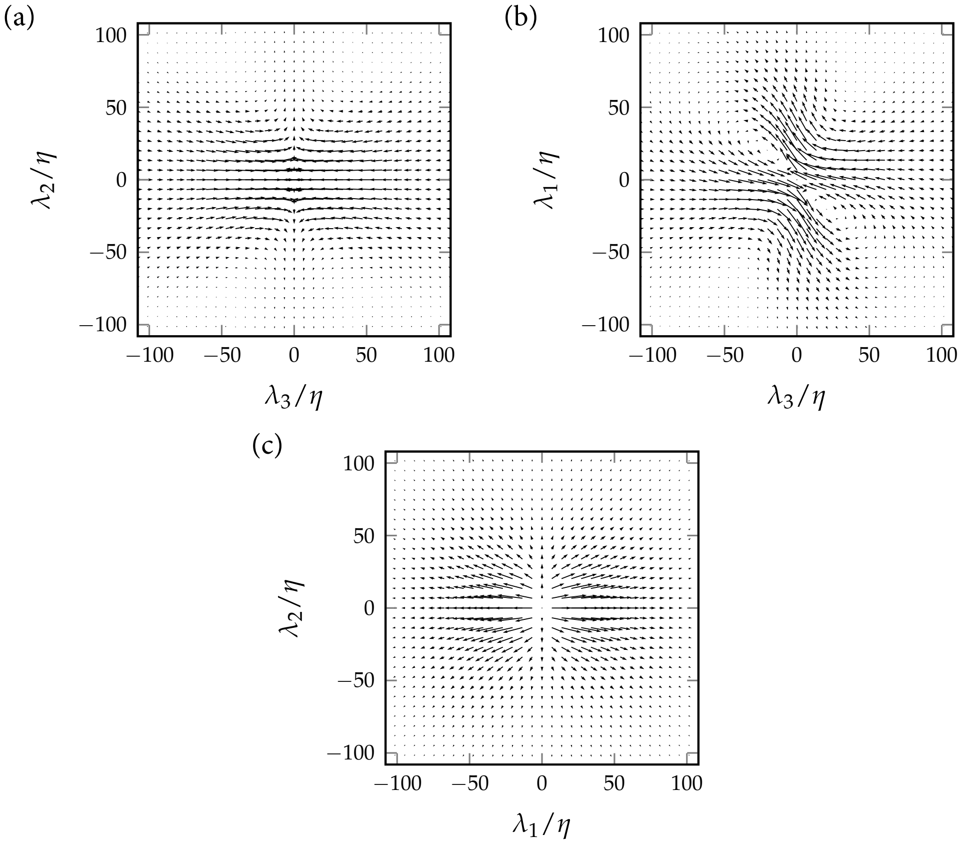

FIGURE 4.1: Average shear-layer structure[7] extracted from a channel flow at friction Reynolds number $Re_\tau = 180$. Figures (a-c) represent velocity vector plots in the cross planes $\lambda_1 = 0$, $\lambda_2 = 0$, and $\lambda_3 = 0$, respectively.

the associated flow structure, which here is referred as the shear-layer structure (SLS). The SLS is an *average structure* extracted from the actual fully developed turbulent flow, and it is shown in Figure 4.1. This average structure has been observed in all kinds of flows and even at high Reynolds numbers. Hence, it is regarded as an universal structure. Additionally, this anisotropic structure depicts $k^{-5/3}$ energy spectrum scaling in nearly all directions[56].

The shear-layer structure consists of two co-rotating vortices coincident with a shear-layer. Similarly, a hairpin packet contains co-rotating heads of hairpin-like, or arch shaped vortices inside a shear-layer[1, 9, 38] (see Chapter 2 and 3). However, the shear-layer structure proposed by Elsinga and Marusic[7] is an average structure, while vortex packets in turbulent channel flow are instantaneous in nature. Hence in the first part of the study, the instantaneous flow structure will be extracted from a vortex packet and will be compared to the average SLS. This is done by identifying a vortex packet in a turbulent channel flow and then extracting the flow structure based on the procedure mentioned in section 4.2.1. Then, the flow structure is compared to the average SLS to understand if the average SLS is the result of combining different turbulent structures in an averaging process.

If the instantaneous flow structure extracted from a hairpin (vortex) packet is similar to the the average SLS, then there is a possibility for vortex (hairpin) packets to exist in different kinds of flows as the SLS is found in all kinds of flows. This also means that certain aspects of the hairpin packet model can be generalized further for all flows, thereby moving towards a more complete description of turbulence. Here it should be noted that the vortices in the packet are not necessarily hairpin like, they could be arch-shaped, single legged vortices or worm-like in a general turbulent flow. Hence, the term 'hairpin' is replaced by vortex hereafter and 'hairpin packet' or 'hairpin packet model' will be referred as 'vortex packet' or 'vortex packet model', respectively.

Furthermore, the link between the SLS and the vortex packets can be exploited to develop more objective and automated method to detect packets. Even though few methods have been proposed to identify packets[1, 53], but they are not robust and completely objective due to the uncertainties in setting the threshold to identify low-speed streaks or vortices. However, this study could offer a new method to identify packets which further can help in studying their statistical relevance (see Chapter 3).

Finally, this study will be extended to explore the evolution of the instantaneous SLS in time. This offers an opportunity to study the dynamics of the SLS in a general frame of reference, which ultimately can be utilized to compare different turbulent flows. However in the present proof of concept study, the shear-layer dynamics in the vortex auto-generation is explored, as the shear-layer plays a role in creating new vortices (See Chapter 2). Additionally, this study in time could help in developing an automated method to detect auto-generation. Hence, the connection between the evolution of the SLS and auto-generation in section 4.3.2 is explored. Then, the implication and future developments of these results will be discussed in section 4.3.3. Followed by conclusions in section 4.4.

4.2 METHODOLOGY

The connection between the average SLS and a vortex packet, which is an instantaneous flow structure, is explored in the direct numerical simulation (DNS) database of fully developed turbulent channel flow (TCF) at $Re_\tau = 180$. The details of the DNS, the TCF database utilized here, the method to visualize vortices, and the symbols used to refer different quantities are the same as those described in the section 3.2, hence they will not be repeated here.

From this database, a vortex packet and auto-generation are detected based on the procedure described in the section 3.2.1. Additionally, the vortex packet and auto-generation considered in this chapter are same as the one from the previous chapter. For simplicity, the vortex packet from previous chapter is again shown in figure 4.2. Finally, the shear-layer structure is extracted and the procedure to extract it is discussed in the following section.

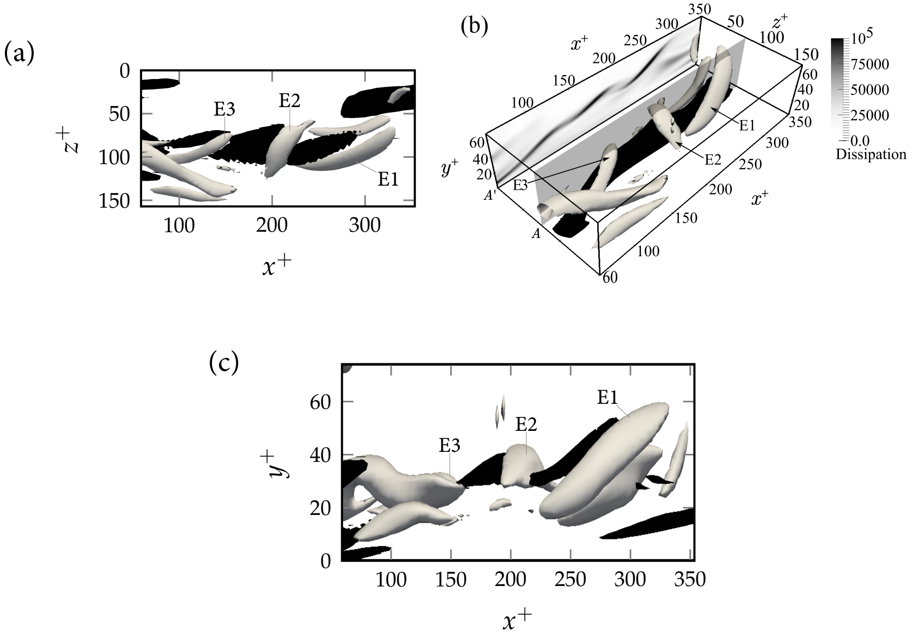
(a)
0
50
100
150
z^+
E3
E2
E1
100
200
300
x^+
(b)
x^+
100
150
200
250
300
350
50
z^+
100
150
60
40
20
350
y^+
60
40
20
A'
A
E3
E2
E1
300
250
200
150
100
60
x^+
10^5
75000
50000
25000
0.0
Dissipation
(c)
60
40
20
0
y^+
E3
E2
E1
100
150
200
250
300
350
x^+

FIGURE 4.2: A vortex packet containing three vortices in fully developed turbulent channel flow at a relative time $t^+ = 11.25$. This is the same packet as shown in Fig. 3.1. Vortices (in gray) represent the iso-surface of the 5% of the maximum swirling strength squared. The black iso-contours in (a) and (c) show 35% of the maximum dissipation (ϵ) and indicate the low-speed streak at $u'^+ = -4$ in (b). ‘E1’ represents the downstream vortex, followed by upstream vortices ‘E2’ and ‘E3’, respectively. (a) Top view of the packet. (b) Isometric view of the packet. Dissipation contour on the cross-stream plane A is projected onto the plane A'. (c) Side view of the packet.

4.2.1 *Shear-layer structure (SLS) extraction*

The instantaneous flow structure will be extracted from a vortex packet observed in the turbulent channel flow. The method to extract the instantaneous flow structure is similar to the one mentioned in the papers by Elsinga and Marusic[7] and Wei et al.[57] apart from a minor modification as explained below. Also, the flow structure in the present case is an instantaneous one as opposed to an average structure[7, 57]. The procedure will be discussed in detail in the following paragraph.

At first, the two co-rotating vortices in an identified vortex packet were constrained into a rectangular box (in the xyz coordinate system) as shown in Figure 4.3. Then, as the origin of the average structure is a node-saddle critical point (see Fig. 4.1), a similar point is probed between the vortices in the box (Point O). The method to locate the origin will be discussed in the next paragraph in detail. Then at the origin (O), the eigenvalues and eigenvectors ($\boldsymbol{\lambda}_i$) of the strain rate tensor s_{ij} are computed, where $\boldsymbol{\lambda}_1$, $\boldsymbol{\lambda}_2$, and $\boldsymbol{\lambda}_3$ indicate the most stretching, the intermediate and the most compressing directions, respectively. Then, the positive direction of the $\boldsymbol{\lambda}_2$ and the $\boldsymbol{\lambda}_3$ directions is defined. The positive direction for $\boldsymbol{\lambda}_2$ is fixed by aligning it with the vorticity vector[7, 57]. And $\boldsymbol{\lambda}_3$ is aligned with the positive stream-wise (x) direction of the flow, which leads to the appearance of the wall of the channel on one particular side in the extracted SLS. With this, $\boldsymbol{\lambda}_1$ is computed to complete the right handed coordinate system. The present definition of the positive $\boldsymbol{\lambda}_1$ and $\boldsymbol{\lambda}_3$ directions is different from that of Wei et al., where $\boldsymbol{\lambda}_1$ was aligned with the positive stream-wise direction and $\boldsymbol{\lambda}_3$ was adjusted to maintain a right handed system. Finally, a 3-d uniform rectangular grid is created in this new coordinate system ($\boldsymbol{\lambda}_i$) as shown in figure 4.3, and the flow field is linearly interpolated onto this grid. λ_i represent coordinates along $\boldsymbol{\lambda}_i$ directions in new coordinate system.

In the average shear-layer structure[56], sheet-like dissipation exists between the two co-rotating vortices. A similar dissipation pattern is observed between the co-rotating vortices in the vortex packet shown in Figure 4.2. Additionally, the dissipation at the origin of the average shear-layer structure is maximal. Along with this, the axis of the co-rotating vortices is aligned with the $\boldsymbol{\lambda}_2$ direction at the origin of the SLS[7]. Hence, the maximum dissipation location between two co-rotating vortices in a vortex packet could be utilized as the origin if the $\boldsymbol{\lambda}_2$ direction is aligned with the axis of the co-rotating vortices. This alignment is tested statistically. In the vortex packet model[1], the axes of the heads of the vortices in the packet are aligned with the span-wise (z) direction. Hence, the associated vorticity is aligned in the span-wise direction. Consequently for a SLS type structure to exist it is expected $\boldsymbol{\lambda}_2$ to align also with the

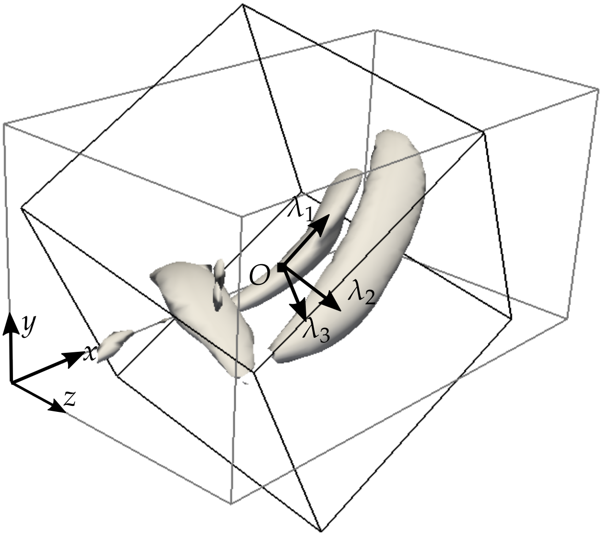

FIGURE 4.3: Boxes indicating the flow (xyz) and the shear-layer structure ($\boldsymbol{\lambda}_i$) coordinate systems. Point 'O' indicates the origin of SLS. Here minus indicates the negative direction of the axis.

span-wise direction in the sheet-like dissipation that exists between two co-rotating vortices (see Fig. 4.2). Therefore, the alignment of the $\boldsymbol{\lambda}_2$ direction with the span-wise direction is examined conditioned on dissipation.

This alignment is investigated by plotting the joint probability density function (JPDF) between the normalized dissipation and the angle between $\boldsymbol{\lambda}_2$ and span-wise direction (z) as shown in Figure 4.4. The JPDF was computed from the points with dissipation lower than $8\langle\epsilon\rangle$ lying between $10-90$ wall units in the wall-normal direction. The dissipation (ϵ) was normalized by the mean dissipation ($\langle\epsilon\rangle$) in the channel. Here, $8\langle\epsilon\rangle$ corresponds to 35% of maximum dissipation and was observed to form sheets in present vortex case (see Fig. 4.2). The points between $10-90$ wall units were chosen for JPDF because three-dimensional structures are not observed below 10 wall units and all the considered structures in this chapter are below 90 wall units. The JPDF in Figures 4.4(a,c) and (b,d) consider data points with positive and negative span-wise vorticity, respectively. Figures 4.4(a) and (b) illustrate the parts of the JPDFs for the low dissipation range up to $2\langle\epsilon\rangle$ and Figures 4.4(c) and (d) represent the parts of the JPDFs for dissipation range between $2\langle\epsilon\rangle$ and $8\langle\epsilon\rangle$. The details on the number

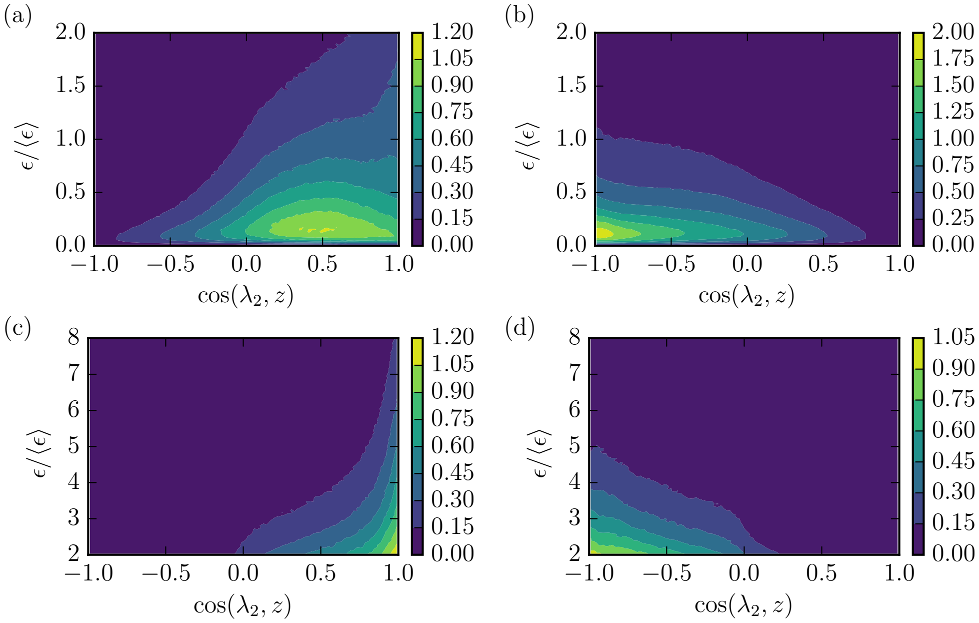

FIGURE 4.4: Joint PDF of dissipation and the cosine of the angle between the $\boldsymbol{\lambda}_2$ direction and the span-wise direction (z) of the channel flow. The span-wise vorticity is positive in case of Fig. (a) and (c) and negative in case of Fig. (b) and (d). The points utilized to plot were lying between $10 - 90$ wall units in the wall-normal direction.

of points considered for the JPDF and their contribution to the total dissipation are shown in table 4.1.

TABLE 4.1: Details utilized to compute JPDF. 23.3% of the total number of points in the channel contributing 22.2% to the total dissipation in the channel were used in the JPDF plots. The utilized points lie between $10 - 90$ wall units in the wall-normal direction.

Span-wise vorticity	Condition	% of total points $\mathcal{O}(10^8)$	% of total dissipation
Positive	$\epsilon < 2\langle\epsilon\rangle$	8.0	5.1
	$2\langle\epsilon\rangle < \epsilon < 8\langle\epsilon\rangle$	1.9	6.9
Negative	$\epsilon < 2\langle\epsilon\rangle$	12.1	6.1
	$2\langle\epsilon\rangle < \epsilon < 8\langle\epsilon\rangle$	1.2	4.1

At the high dissipation, Figure 4.4(c,d), the intermediate eigenvector oriented with vorticity, i.e, $\boldsymbol{\lambda}_2$ is strongly aligned in the positive or negative span-wise direction (z)

depending on the sign of the span-wise vorticity component. When considering the positive span-wise vorticity (Figure 4.4(c)) the alignment at high dissipation is much stronger than that of the negative span-wise vorticity (Figure 4.4(d)). Hence in general, at the points of high dissipation, $\boldsymbol{\lambda}_2$ is aligned with the span-wise direction. This alignment of $\boldsymbol{\lambda}_2$ together with the observation that the dissipation is high between the co-rotating vortices in packets is consistent with the average SLS. Therefore, the origin of the instantaneous shear-layer structure will be identified based on the maximum dissipation between two co-rotating vortices in a packet. This origin is indicated in Figure 4.3 as point O.

4.3 RESULTS AND DISCUSSION

At first, the connection between an average shear-layer structure to an instantaneous flow structure in a fully developed channel flow at $Re_\tau = 180$ is explored. This is done by extracting an instantaneous structure from a vortex packet by the procedure mentioned in section 4.2.1. Then, it is compared to an average shear-layer structure and will be discussed in section 4.3.1. Next, in section 4.3.2, the evolution of the instantaneous flow structure or the instantaneous SLS in time is examined by applying the structure extraction procedure to vortex auto-generation. Finally, the implications and possible future developments based on the observations are discussed in the section 4.3.3.

4.3.1 *Instantaneous shear-layer structure*

The instantaneous flow structure is extracted from the vortex packet (Figure 4.2) based on the procedure described in the section 4.2.1. The location of the maximum dissipation in the box constraining two vortices in the packet was identified as the origin of the flow structure and further the velocity field was extracted. This extracted instantaneous flow structure is illustrated in Figure 4.5, where Figure 4.5(a-c) and 4.5(d-e) show the streamlines and the velocity vector plots in different planes, namely $\lambda_2 = 0$, $\lambda_1 = 0$, and $\lambda_3 = 0$, respectively. The dashed black lines are drawn to indicate the origin of the structure (point $0, 0$). The colored streamlines from blue to green to yellow indicate low to high local swirling strength squared.

The vortex in the second quadrant in figure 4.5(a) and 4.5(d) is the vortex 'E2' (from Fig. 4.2) and similarly, vortex 'E1' is observed in the fourth quadrant. The streamlines in figure 4.5(b) show the existence of the two counter-rotating vortices in quadrants 1 and 4. These vortices correspond to the leg of the vortex 'E1' and the adjacent stream-

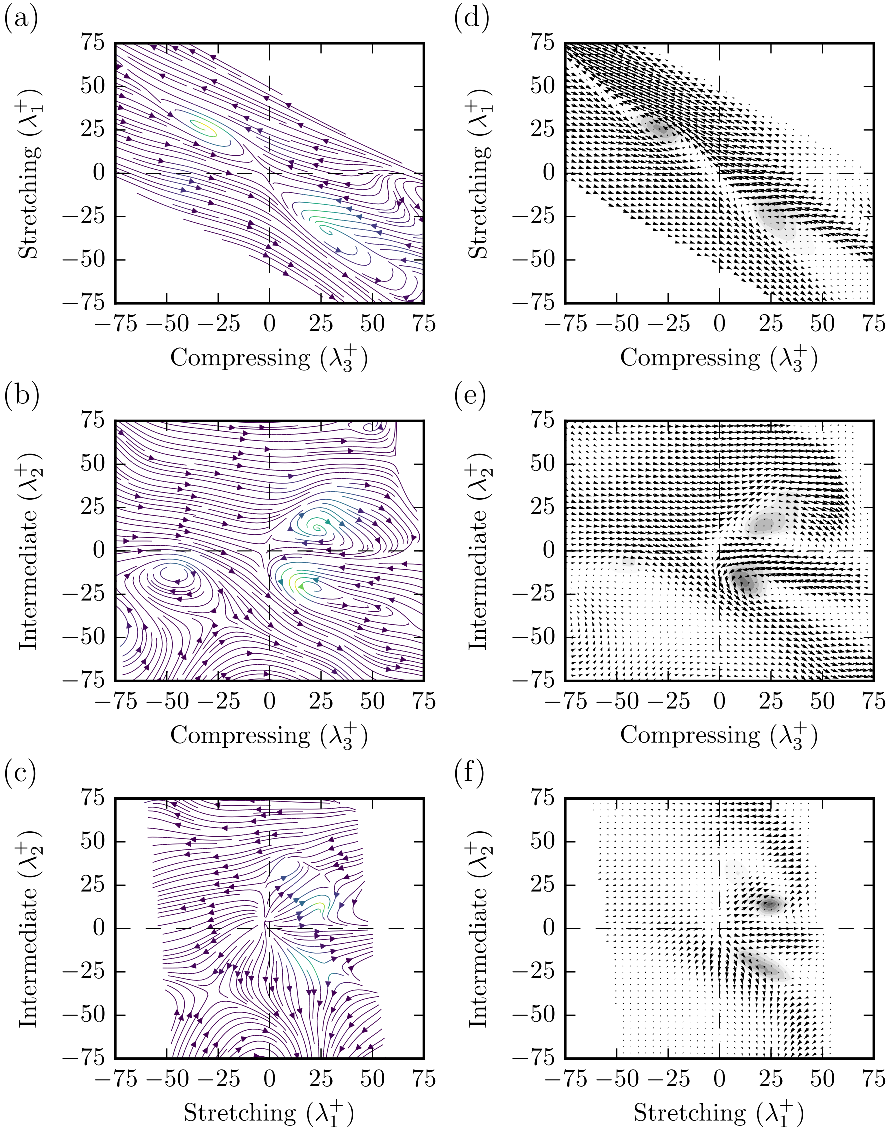

FIGURE 4.5: Figures (a-c) and (d-f) represent the extracted instantaneous shear-layer structure in the planes $\lambda_2 = 0$, $\lambda_1 = 0$, and $\lambda_3 = 0$, respectively at time $t^+ = 2.25$ from the vortex packet (see Fig. 4.2). Figures (a-c) show the streamlines and line colors from blue to green to yellow represent increasing local swirling strength squared. Figures (d-f) show the corresponding velocity vector plots and dark contours indicate local swirling strength to indicate the the vortices.

wise vortex in the span-wise direction as observed in the figure 4.2. Third vortex is also observed in figure 4.5(b) in quadrant 3, however in the velocity vector plots (see Fig. 4.5(d)) it can be noted that the velocity magnitude is too low. Additionally, the local swirling strength was found to be very low.

The instantaneous shear-layer and the two vortices in the $\lambda_2 = 0$ plane (figure 4.5(a,d)) are qualitatively similar to the average SLS structure observed in Elsinga and Marusic[7] and in Fig. 4.1(a). The flow pattern till about 15 wall units from the origin in all directions in the other two planes ($\lambda_1 = 0$ and $\lambda_3 = 0$) is similar to the average structure. However, it deviates from the average shear-layer structure as the distance from the origin increases. For instance, the two counter-rotating vortices in the λ_1 plane (Fig. 4.5b) are not observed in the average structure. Also, the instantaneous flow pattern does not reveal a 180 degree rotational symmetry in the planes $\lambda_3 = 0$ and $\lambda_1 = 0$ in figures 4.5(b) and (c), respectively, as compared to the average structure (Fig. 4.1(a) and (c)). This difference is attributed to the averaging procedure where, only one direction (λ_2) is fixed (aligned with vorticity) and other two directions are chosen arbitrarily. When averaging, these unconstrained directions lead to the random orientation of the flow field with respect to these directions, resulting in a symmetric flow field as observed in figure 4.1.

From these observations, it descents that the two co-rotating vortices in vortex packet could be viewed as an instantaneous shear-layer structure. This is further tested for different pairs of co-rotating vortices in the vortex packet by observing the $\lambda_2 = 0$ plane of the extracted shear-layer structure. From this point, instantaneous shear-layer structure will simply be referred as the *shear-layer structure*. And the average structure will continue to be referred to as the average shear-layer structure.

The figures 4.6a and 4.6b illustrate the SLS extracted at time $t^+ = 11.25$ from the vortex packet between the vortex pairs (E1,E2) and (E2,E3), respectively (see Fig. 4.2). The black solid slanted line on the right side of the figures indicates the wall of the channel. This is the consequence of constraining the λ_3 direction by aligning it with stream-wise direction (x), which simplifies the identification of the wall and the correspondence between the vortices of the packet and those in the SLS.

The velocity vector plots indicate two co-rotating vortices coincident with a shear layer similar to the average structure. However, the location of the vortices is not symmetric as observed in the averaged SLS (see Fig. 4.1(a)). Also, the shear-layer is not perfectly straight as seen in average SLS. This is because the location of the maximum dissipation shifts with time relative to the two vortices. Additionally, the plane $\lambda_1 = 0$ provides some insights about the straining motions in the shear layer. The two counter-rotating vortices, i.e., the stream-wise leg of vortex ‘E1’ and the one beside it

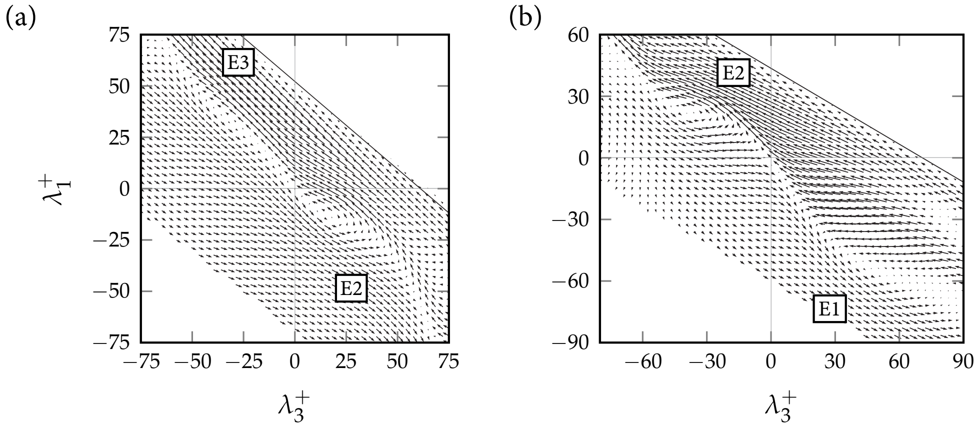

FIGURE 4.6: Vector plot in the plane $\lambda_2 = 0$ of the extracted shear-layer structure from a vortex packet. (a) The origin of the shear-layer structure is the maximum dissipation point between the vortices E2 and E3. The vortices in quadrant 4 and 2 are the vortices E2 and E3, respectively. (b) The origin of the shear-layer is the maximum dissipation point between E1 and E2. The vortex in quadrant 4 is vortex E1 and and quadrant 2 is vortex E2 in the packet shown in figure 4.2.

(see Fig. 4.2) are observed in $\lambda_1 = 0$ plane in 4.5b. These counter-rotating vortices are responsible for compressive straining motions, which cannot be observed in the average SLS. The SLS extracted from other two vortex packets produced similar results (see Appendix B.2). Hence, the SLS does exist instantaneously in a turbulent channel flow and the two vortices in the $\lambda_2 = 0$ plane are not just a consequence of averaging. Additionally, the pair of co-rotating vortices in the vortex packet can be viewed as a SLS which is extracted based on the universal feature of alignment of the intermediate eigenvector with vorticity. This links the packet structures to the universal features.

Further, the evolution of the instantaneous SLS in time is studied, which, in the future could help in understanding shear-layer dynamics and can be utilized to detect auto-generation in a general frame of reference. This is a proof of concept study, which is applied to the generation of new vortices in vortex packets[1] and will discussed in the following section.

4.3.2 *Auto-generation and shear-layer structure*

The dynamics of a parent vortex generating a new co-rotating vortex in a vortex packet is examined in the shear-layer structure frame of reference. This is studied by extract-

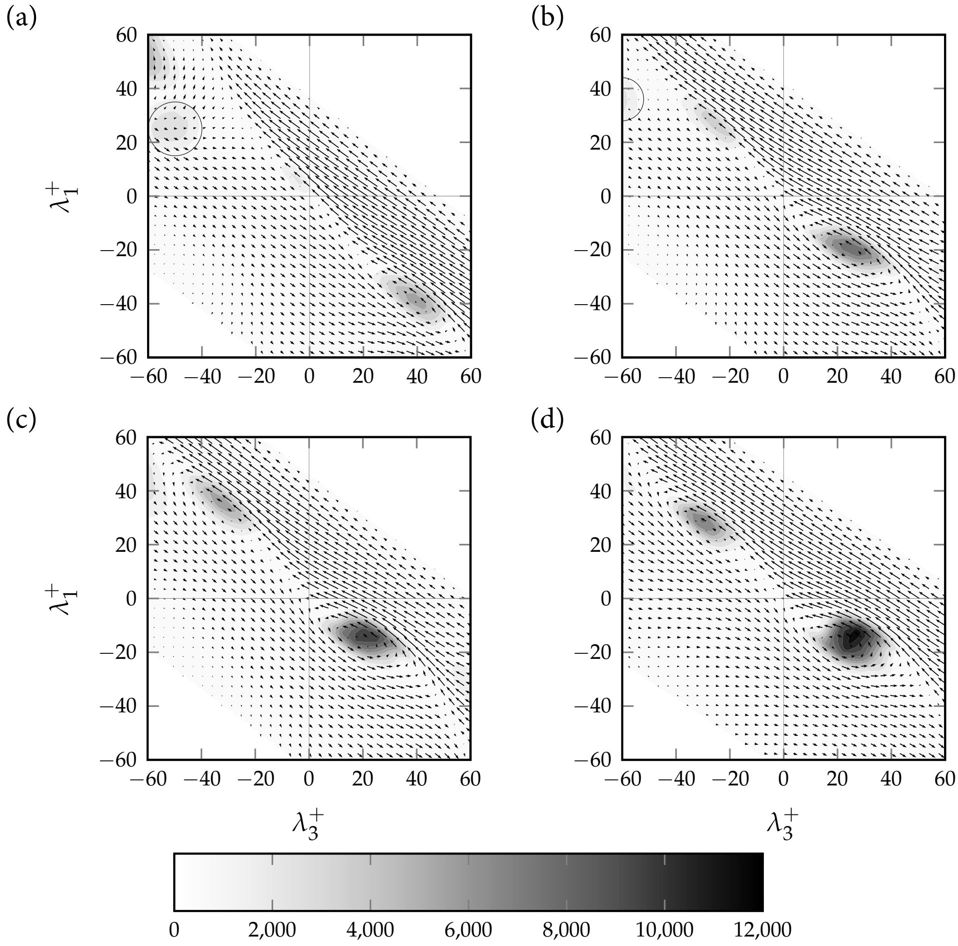

FIGURE 4.7: Time series of auto-generation in the intermediate eigenvector plane $\lambda_2 = 0$ of the extracted shear-layer structure. Contours indicate the square of the local swirling strength. Figures (a)-(d) show the generation of vortex 'E3' in the second quadrant from the parent vortex 'E2' in the fourth quadrant. The relative times of the plots correspond to $t^+ = 0,\ 4.5,\ 9.0$, and 13.5, respectively. The local swirling contours in circle in (a) at location (-50,25) are same as the contours in arc in (b) at (-0,30). This is plotted to avoid the confusion that the contours in circle in (a) evolve into a vortex in quadrant 2.

ing the SLS from the identified auto-generation case in actual channel turbulent flow (see Fig. 3.2 and 3.3 in Chapter 3). The SLS was extracted based on the procedure described in section 4.2.1. However, there is one difference from the procedure in section 4.3.1. The point of maximum dissipation, i.e., the origin, was located in a plane instead of a constrained box containing two vortices, because at the start of auto-generation there is only one parent vortex. Hence, a suitable cross-stream plane (xy) cutting through the low speed streak was identified as before, which is shown in figure 4.2(b). Then, the maximum dissipation point in this plane was located upstream of the parent vortex and was utilized as origin to extract the shear-layer structure. This maximum dissipation point or the origin upstream of the vortex is detected in time, which means that the maximum dissipation point is followed in time. Then, the shear-layer structure was extracted.

Figure 4.7 illustrates the generation of the vortex 'E3' in time from a parent vortex 'E2' (Figure 3.2), in the SLS frame of reference. The time step between each figure from Fig. 4.7(a) to Fig. 4.7(d) is 4.5 time wall units.

Contours of local swirling strength in figure 4.7(a) show one vortex 'E2', i.e., the parent vortex, in the fourth quadrant. The shear-layer in the figure is observed to be approximately straight. With increasing time, the shear-layer in the fourth and the second quadrant continuously deforms. The shear-layer deformation is observed in auto-generation simulations[38], which is associated with the inrush of fluid upstream of the parent vortex (presently 'E2'). Also, the vortex 'E2' grows larger in diameter and their local swirling strength increases with time as observed in figures. At time $t^+ = 9$, from vector plots it is seen that a new vortex 'E3' comes into existence in the second quadrant (see Fig. 4.7(c)). And with time, it grows in diameter and its swirling strength increases as observed in Figure 4.7(d). Hence, this dynamics of generation of a new vortex can be viewed in the SLS frame of reference as a shear-layer deformation and roll-up.

4.3.3 *Implications and future developments*

A trial and error method was used to set the threshold to identify vortices and the low-speed streaks, which are further utilized to identify the vortex packets. Some adjustments of the thresholds was needed, because if a too low threshold is used to identify vortices, then many and largely overlapping vortices are spotted. This makes it difficult to identify individual vortices in 3-d. On the other hand, a higher threshold leads to fewer vortices, and loss of vortices in the vortex packets. A similar observation could be made for the low-speed streaks. Also, the uncertainty increases when considering vortex generation, as the swirling strength of a newly generated vortex is low and an additional dimension, *time*, gets added. Hence, it is necessary to determine a different method to identify the packets and auto-generation, which does not rely on arbitrary thresholds.

The present study shows that the two co-rotating vortices in a vortex packet in a turbulent channel flow are qualitatively similar to the vortices of the average shear-layer structure. This information could be utilized to identify packets. For instance, one may consider a group of points, where the intermediate eigenvector, $\boldsymbol{\lambda_2}$, is aligned with the span-wise direction. If the identified points are close to each other, then a point with high dissipation is considered as the origin. At this point, a flow structure in the strain eigenframe $(\lambda_1, \lambda_2, \lambda_3)$ is extracted. Next, the two co-rotating vortices can be probed based on vector plots in the $\lambda_2 = 0$ plane. If the vortices exist and the flow topology at the origin is a node-saddle point, then a shear-layer structure is identified. With few of these SLS points in a certain pattern, a vortex packet could be identified. This eliminates the uncertainty in defining the threshold to locate vortices or low-speed streaks. Hence, the present work not only links the vortices in the packet to the shear-layer structure, but it is also a small step in the creation of an objective and robust algorithm to identify these packets and furthermore, the generation of new vortices in a packet.

The averaged shear-layer structure has been detected in many different kinds of turbulent flows[7]. And in this study, the existence of the shear-layer structure in an instantaneous turbulent channel flow has been shown. Similarly, the existence of shear-layer structures can be probed in other instantaneous flows based on the procedure mentioned in this study. And if they are detected in other kinds of flows, then, there is the possibility of finding vortex packets in isotropic turbulence as the dissipation is observed to form long and large sheets[58], which is similar to the observations in channel flow. However, this is a hypothesis, which needs to be tested by detecting a series of shear-layer structures.

4.4 CONCLUSIONS

The link between the average shear-layer structure, which may be considered a universal feature of turbulence, and the instantaneous vortex packets in a turbulent channel flow at low Reynolds number was shown. First, the vortex packet was identified in a fully developed turbulent channel flow at $Re_\tau = 180$. Then, two co-rotating vortices were constrained in a box and an instantaneous flow structure was extracted in the strain eigenframe with the location of maximum dissipation as the origin of the structure.

It was found that the instantaneous flow structure was similar to the average SLS. Additionally, the instantaneous flow structure or instantaneous SLS was observed in every pair of consecutive co-rotating vortices in the different vortex packets. Hence, the two vortices in the $\lambda_2 = 0$ plane and in the average SLS do exist in an instantaneous turbulent flow, and they are not just the result of the averaging procedure. Moreover, a pair of co-rotating vortices in a vortex packet could be viewed in a different frame of reference as a shear-layer structure.

The generation of a new vortex in a vortex packet also could be viewed in the frame of reference attached to the shear-layer structure. In the beginning of the generation of a new vortex, the shear-layer was found to be straight, and with time it is slowly deformed. At the same time, the swirling strength of the parent vortex increased, and also it grew in diameter. Simultaneously, a new vortex was generated inside the shear-layer. Subsequently, the newly generated vortex also grew in diameter and swirling strength increased in time.

This connection between vortex packets and the shear-layer structure could be utilized to develop an objective method to identify vortex packets in wall-bounded flows. Also, as the average shear-layer structure is observed in all kinds of flows and is considered universal, its instantaneous existence in different flows could be explored in future. This method of detecting structures offers a basis to compare different flows and possibly generalize results.

To conclude, a pair of co-rotating vortices in a vortex packet at low Reynolds number in a turbulent channel flow could be viewed in different frame of reference as a shear-layer structure, which is further related to universal features of turbulence.

5

TRACER PARTICLE DISPERSION AROUND ELEMENTARY FLOW PATTERNS

The relevance of coherent structures, such as vortices and shear-layers in three dimensional turbulence, was studied in previous chapters. In the present chapter, the influence of such structures on the dispersion of tracer particles is examined. Three representative flow structures, namely a shear-layer structure, a node-saddle topology and a Burgers' vortex, are considered as they correspond to elliptical and hyperbolic critical points. Different tracer dispersion statistics, such as pair dispersion, tetrad dispersion, and material lines, are explored and compared with the actual turbulent flow.

5.1 INTRODUCTION

The role of the carrier fluid in the transport of scalar quantities (e.g., particles or chemicals) is important in many natural and industrial processes. Generally, turbulence is implicitly present in the carrier fluid in processes such as cloud formation, pollination, and pollutant dispersion. In the case of combustion and chemical mixing, induction of turbulence is desired to enhance the mixing of scalar quantities. So, the understanding of the scalar transport by the turbulent carrier fluid is important. The simplest quantitative description of the scalar motion is the statistical evolution of the displacement of two marked particles[59–62]. This displacement, expressed in terms of the mean-square particle separation, indicates the average distance traveled by the particles around their center of mass after time t. The study of the orientation of material lines[62–65] helps in understanding the geometry of turbulence, as well as the orientation of passive scalars. More complicated descriptions are measured by the evolution of geometrical properties, such as, the shape and the size of the scalar field, which are characterized by four particle or tetrad dispersion statistics[66–72]. In the available literature, the Lagrangian particle dispersion is mostly discussed in terms of these particle statistics. Little attention is given to understand the underlying turbulent fluid motions and the relevance of Eulerian flow structures present in turbulence.

Flow structures in three-dimensional turbulent flows are identified and studied as the result of the advancement in experimental techniques and computational power in the last few decades. Few examples are the vortex structures[9], a possibly universal shear-layer structure[7], and the node-saddle topology[5]. These structures provide insights into the local geometrical and topological features of turbulence[5, 7, 9], which has led to new ideas to model fluctuating velocities in turbulence[9, 73]. Similarly, studying particle motion around these structures may help in understanding particle dynamics in turbulence and also in describing the scalar dispersion. This may lead to model dispersion alongside the turbulence in the structure based models. Additionally, the particle motion also provides an insight into the dynamics behind the particle separation in a flow. However, in the literature, there are few studies on the particle dispersion around structures[74].

A two-dimensional turbulence study[37] linked the dynamics of the two particle statistics to the critical points, which are further associated with flow patterns. The particle pair separation was described in a step-by-step process around the critical points. These points were hyperbolic zero-acceleration points, i.e., saddle points, and elliptical zero acceleration points corresponding to straining strips of zero vorticity and vortex centers, respectively. The paper[37] showed that the particle pairs stayed together in the proximity of elliptical points and separated in the vicinity of saddle points. Furthermore, based on this observation, a model was constructed to predict the temporal evolution of the pair dispersion statistics. However, this work was done in two dimensions.

In this chapter, similar studies will be performed in three dimensions around idealized flow structures. The pair and tetrad dispersion, and the orientation of material lines are studied around different flow patterns containing critical points, such as a saddle point and an elliptical zero acceleration point. Three flow patterns containing these critical points were considered, namely a Burgers' vortex, a shear-layer structure, and a node-saddle topology. The Burgers' vortex[75] is often utilized to describe small scale vortices and intense vorticity structures in turbulent flows[76, 77]. Also, the center of the Burgers' vortex is an elliptical point. Secondly, the shear-layer structure[7] containing a saddle point along with a shear-layer at its center is considered. This average shear-layer structure has been observed in different turbulent flows[7]. It is considered as it represents the average velocity field around a point in a turbulent flow, when the coordinate system is aligned with the principal straining directions. Finally, the mentioned shear-layer structure is symmetrized, yielding the same strain field as the shear-layer, but with a different node-saddle topology. The dispersion statistics are studied around these structures and compared with the actual turbulent flows. If the statistics are similar, it may suggest that these structures are responsible for the dispersion of the tracer particles in a turbulent flow.

The description of the different flow structures and the method to generate them is described in Section 5.2. In Section 5.3, the details of the particle simulation and the computed dispersion statistics are explained. First, the pair dispersion[59–62, 74, 78–81] is described in terms of the root mean square of relative separation, and the compensated relative dispersion whose theory is discussed in detail in Section 5.3.1. In Section 5.3.2, the orientation of material lines is computed based on the velocity gradient at the critical point. Finally, the tetrad dispersion[68, 72] is characterized by the evolution of the size and shape of a tetrahedron. The quantification of the shape and size of the tetrahedrons is explained in Section 5.3.3. The results are presented in Section 5.4, where the statistics are compared to actual turbulent flows. Furthermore, the snapshots of the particle distribution at specific times are plotted to illustrate the dispersion of the particles around the different flow structures. Finally, the conclusions will be discussed in Section 5.5.

5.2 FLOW STRUCTURES

The tracer particle motion is simulated around three different flow structures: a Burgers' vortex, a shear-layer structure, and a node-saddle topology. The Burgers' vortex (BV) is analytically computed from the equations, while the shear-layer structure (SLS) and the node-saddle topology (NST) are extracted from an isotropic turbulent flow. The details of generating and extracting these structures are discussed in the following paragraphs.

5.2.1 *Burgers' vortex (BV)*

The velocity field of a Burgers' vortex[75], an exact solution of the Navier-Stokes equation, is given by

$$u_z = \alpha z, \qquad u_r = -\frac{\alpha r}{2}, \qquad u_\theta = \frac{\Gamma}{2\pi r}\left[1 - \exp\left(-\frac{\alpha r^2}{4\nu}\right)\right] \tag{5.1}$$

where α, Γ, and ν represent the rate of strain, vortex circulation, and viscosity, respectively. u_z, u_r, and u_θ correspond to the velocity components in the axial (z), radial (r), and azimuthal (θ) directions, respectively. The Reynolds number of the vor-

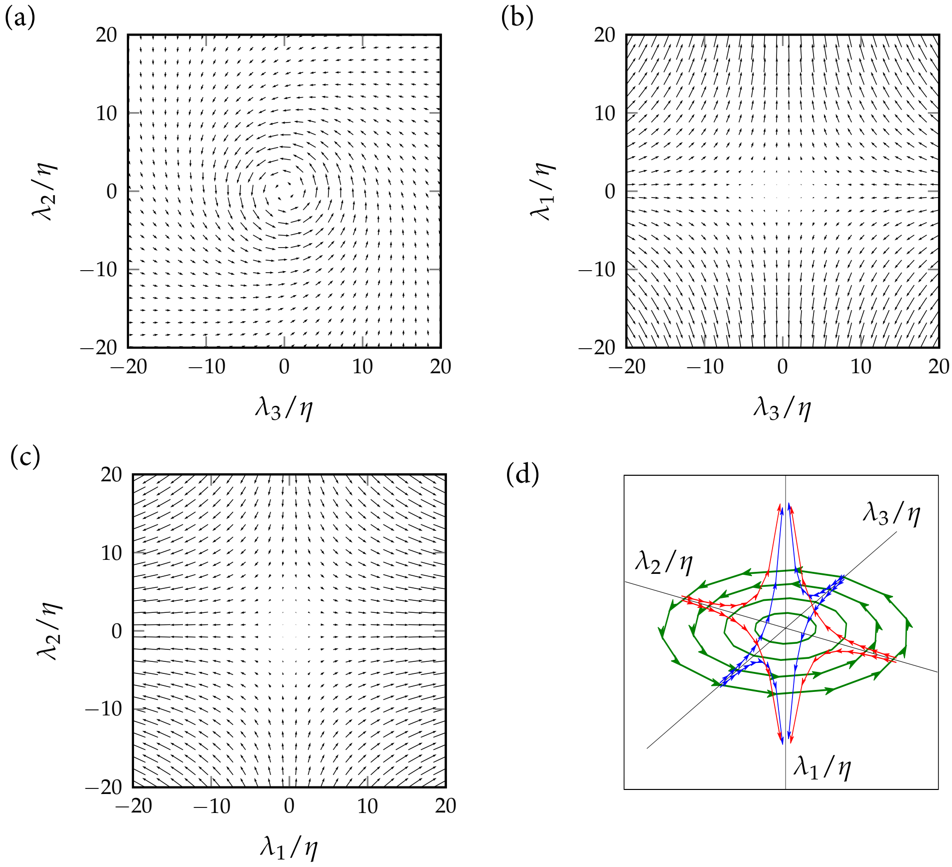

FIGURE 5.1: Burgers' vortex in a Cartesian coordinate system. Figures (a-c) represent velocity vector plots in $\lambda_1 = 0$, $\lambda_2 = 0$ and $\lambda_3 = 0$ planes, respectively. All length scales are normalized by the Kolmogorov length scale (η).

tex based on the circulation is defined as $Re_\Gamma = \Gamma/(2\pi\nu)$ and the radius is given as $r_m = 2\sqrt{\nu/\alpha}$. Jimenez and Wray[76] and Silva et al.[77], among others, have shown that the core of the intense vorticity structures (IVS) in homogeneous isotropic turbulence and jet flows can be described by the Burgers' vortex model. The characteristics of the IVS, such as, the mean value of the vortex core radius, the mean maximum azimuthal velocity, and the Reynolds number based on circulation (Re_Γ), have been reported in Silva et al.[77]. The Burgers' vortex is described completely by three parameters. Here, the vortex core radius ($r_m/\eta = 4.65$), vortex circulation ($\Gamma/u_\eta\eta = 415.67$), and rate of strain ($\alpha\eta/u_\eta = 0.25$) values were computed using the data presented in Silva et al.[77] for the forced homogeneous isotropic turbulence

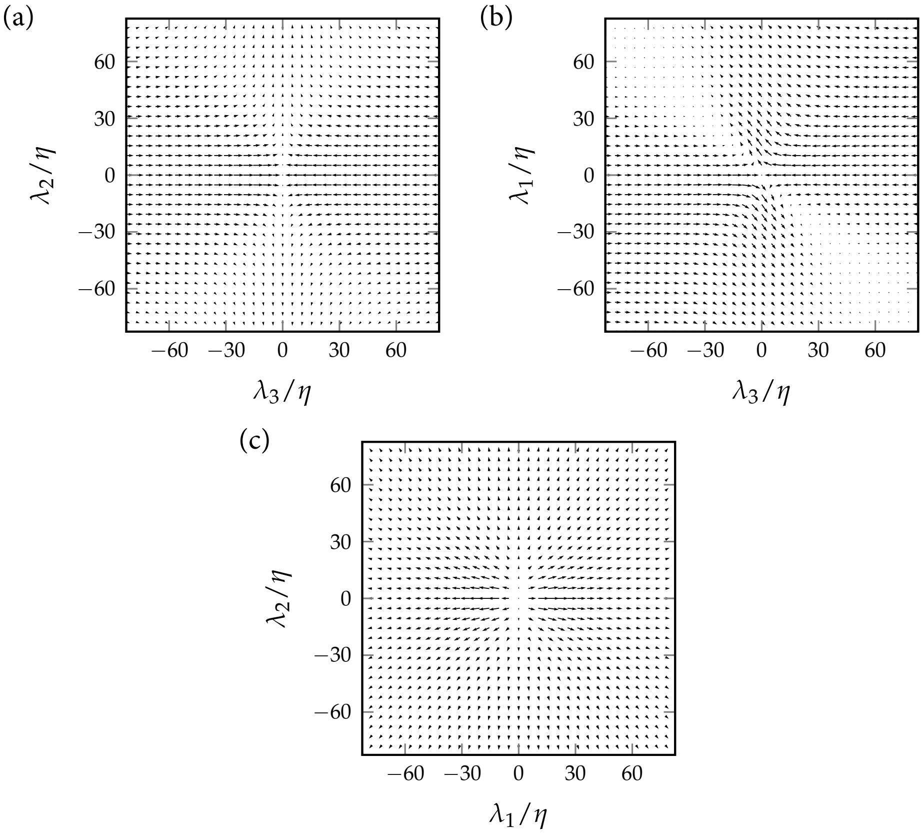

FIGURE 5.2: Shear-layer structure[7] extracted from the isotropic turbulent flow[82] at $Re_\lambda = 433$. Figures (a-c) represent velocity vector plots in the cross planes $\lambda_1 = 0$, $\lambda_2 = 0$, and $\lambda_3 = 0$, respectively. All the length scales are normalized by the Kolmogorov length scale (η).

(HIT) at a Taylor Reynolds number $Re_\lambda = 111$. The Kolmogorov length (η) and velocity (u_η) scales are used for normalization. Figure 5.1 illustrates the Burgers' vortex computed from Equation (5.1) using the above mentioned values. All the length and velocities scales are converted from the cylindrical to a Cartesian coordinate system ($\lambda_1, \lambda_2, \lambda_3$) to simplify the comparison between different structures. Here λ_2 and λ_3 are radial/compressive strain directions and λ_1 corresponds to the stretching strain direction, which coincides with the vortex axis, i.e., the z-axis in Equation (5.1).

5.2.2 *Shear-layer structure (SLS)*

The shear-layer structure (SLS) is extracted from a direct numerical simulation (DNS) of a homogeneous isotropic turbulent flow[82] at a Taylor Reynolds number $Re_\lambda = 433$ using the averaging procedure described in Elsinga and Marusic[7]. The SLS appeared qualitatively similar in different kinds of turbulent flows, hence, considered universal[7]. The flow field around the origin of this structure describes the average flow field around a point in the flow when the observer is aligned with the local directions of principal strain. A brief explanation of the averaging procedure to extract this structure is as follows.

First, the strain rate tensor is computed from the velocity gradients ($\partial u_i/\partial x_j$) at a point $\mathbf{x}_p$ in turbulent flow database. Then, the eigenvalues and the principal directions (i.e., eigenvectors) of the strain rate tensor are calculated. The principal directions $\mathbf{e}_1$, $\mathbf{e}_2$, and $\mathbf{e}_3$ represent the most stretching, the intermediate, and the most compressing straining directions, respectively. A new coordinate system (λ_i) is formed based on these principal directions. Furthermore, the positive intermediate straining direction ($\mathbf{e}_2$) is chosen such that its dot product with the vorticity vector is positive. A unit vector corresponding to $\mathbf{e}_3$ is fixed as the third direction (λ_3). To complete the right handed coordinate system, the first direction (λ_1) is computed as the cross product between the second (λ_2) and third (λ_3) direction. The flow velocities ($\mathbf{u}$) on the new coordinate system ($\lambda_1, \lambda_2, \lambda_3$) relative to the point $\mathbf{x}_p$ are computed by linear interpolation. The components u_i represent velocities along the corresponding λ_i directions. This 3-d velocity field in the new coordinate system is calculated at different points in the flow and averaged to obtain the shear-layer structure as illustrated in Figure 5.2. One of the main features of this structure is a shear layer, which spans from the top left corner in Figure 5.2b to the bottom right corner.

5.2.3 *Node-Saddle topology*

The node-saddle topology (NST) is obtained by applying planar symmetry to all velocities (u_1, u_2, u_3) in the previously discussed shear-layer structure. The velocity component u_1 is made symmetric about the plane $\lambda_1 = 0$. Similarly, u_2 and u_3 are made symmetric about the planes $\lambda_2 = 0$ and $\lambda_3 = 0$, respectively. The velocity vector plot in the different cross planes is shown in Figure 5.3. The difference between the node-saddle topology and the shear-layer structure can be seen by comparing Figures 5.2 and 5.3. The shear-layer in Figure 5.2b vanishes in Figure 5.3b due to the planar symmetry, resulting in a pure node-saddle critical point with no vorticity at the origin.

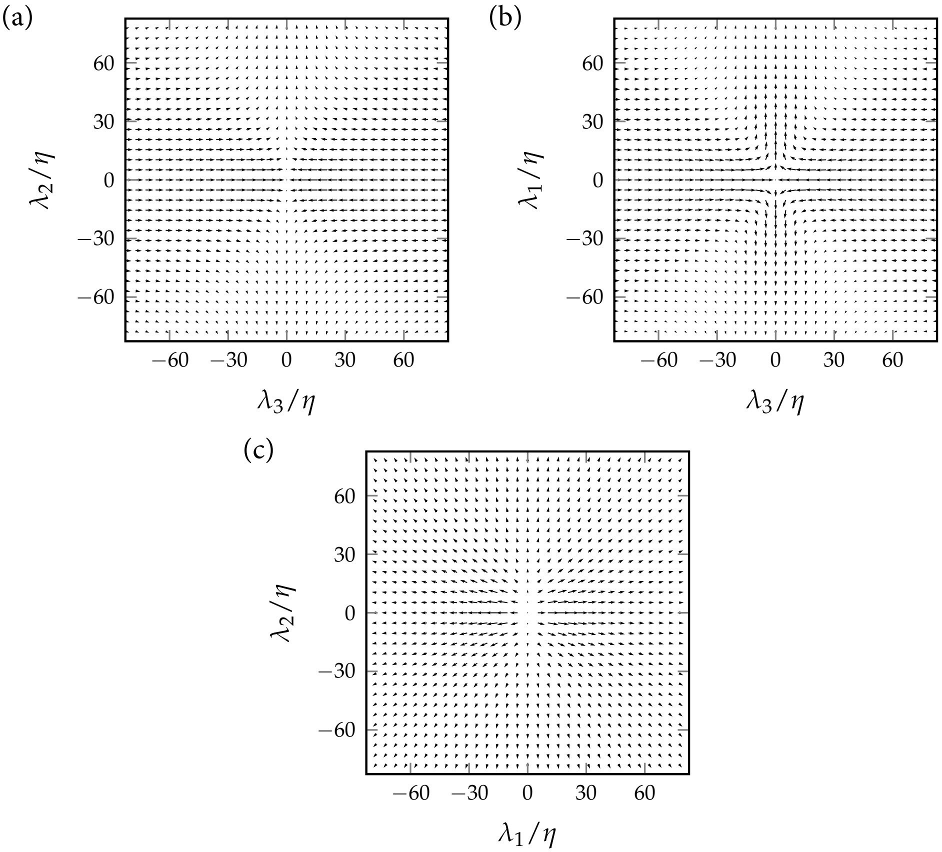

FIGURE 5.3: Node-saddle topology obtained by symmetrizing the shear-layer structure presented in Figure 5.2. Figures (a-c) represent velocity vector plots in the cross planes $\lambda_1 = 0$, $\lambda_2 = 0$, and $\lambda_3 = 0$ planes, respectively. All the length scales are normalized by the Kolmogorov length scale (η).

5.3 PARTICLE SIMULATION AND STATISTICS

The point particles considered in the pair and tetrad dispersion are passive tracers or marked fluid parcels. Their motion is simulated according to

$$\frac{d\mathbf{x}_p(t)}{dt} = \mathbf{u}(\mathbf{x}_p(t)), \tag{5.2}$$

where $\mathbf{u}(\mathbf{x}_p)$ represents the fluid velocity at the instantaneous particle position $\mathbf{x}_p$. The explicit fourth-order Runge-Kutta scheme is employed to integrate the equation in time. The velocity on the right-hand side is calculated by the tri-linear interpolation of the velocity field of the steady flow structure. To study pair dispersion, 5000 particle pairs are uniformly distributed on a sphere around the origin[83], where, the center of mass of each pair coincided with the origin of the extracted flow structures as shown in figure 5.4. The particle distribution is chosen around the origin of structures as they correspond to critical points mentioned by Goto and Vassilicos[37]. Subsequently, the particle motion follows from the above equation. Due to the symmetries in the considered flow structures the center of mass of a particle pair remains at the origin in all cases and at all times. The initial separation distance between the two particles of a pair is defined as the diameter of the sphere, i.e., twice the distance between the particle and the origin, where the center of the mass of the pair is located. Similar to the pair dispersion, tetrad dispersion is studied by kinematically simulating 4000 regular tetrahedrons (same edge length) around the origin of the flow structures. The origin of the structure coincides with the centroid of the tetrahedron. The quantities to describe the pair and tetrad dispersion are explained in the following Sections 5.3.1 and 5.3.3, respectively. The details concerning the simulations of material lines and the statistics of their orientation will be discussed in the Section 5.3.2.

5.3.1 *Pair dispersion*

The pair dispersion describes the average separation of particles. This is characterized by the evolution of the mean square of the relative separation (MSRS) between two particles[59, 60], which is expressed as $\langle|\mathbf{r}(t)-\mathbf{r}(0)|^2\rangle$, where $\mathbf{r}(t)$ represents the separation vector at time t, $\mathbf{r}(0)$ is the initial separation vector, and, $\langle\cdot\rangle$ and $|\cdot|$ describe the mean and the Euclidean norm, respectively. The separation vector $\mathbf{r}(t)$ is computed as $\mathbf{x}_1(t)-\mathbf{x}_2(t)$, where $\mathbf{x}_1(t)$ and $\mathbf{x}_2(t)$ are the positions of the two particles at time t. In the inertial range of the turbulent flow, Batchelor[60] predicted the mean square of the relative separation as

$$\langle|\mathbf{r}(t)-\mathbf{r}(0)|^2\rangle = \begin{cases} \dfrac{11}{3}C_2(\epsilon r_0)^{2/3}t^2 & \text{for} \quad t \ll t_B = r_0^{2/3}\langle\epsilon\rangle^{-1/3} \\ \dfrac{3}{2}g\epsilon t^3 & \text{for} \quad t_B \ll t \ll T_L, \end{cases} \tag{5.3}$$

where C_2 is the Kolmogorov constant in the second-order Eulerian structure function, ϵ is the average dissipation rate of the flow, r_0 is the initial separation between the particle pair, t_B is the Batchelor's timescale after which dispersion is not influenced by r_0, g is the Richardson's constant, which is assumed to be a fundamental constant in turbulence, and T_L is the integral time scale of the flow. The first sub-range where $t \ll t_B$ (see Eq. (5.3)) is referred to as Batchelor's ballistic regime. In the literature,

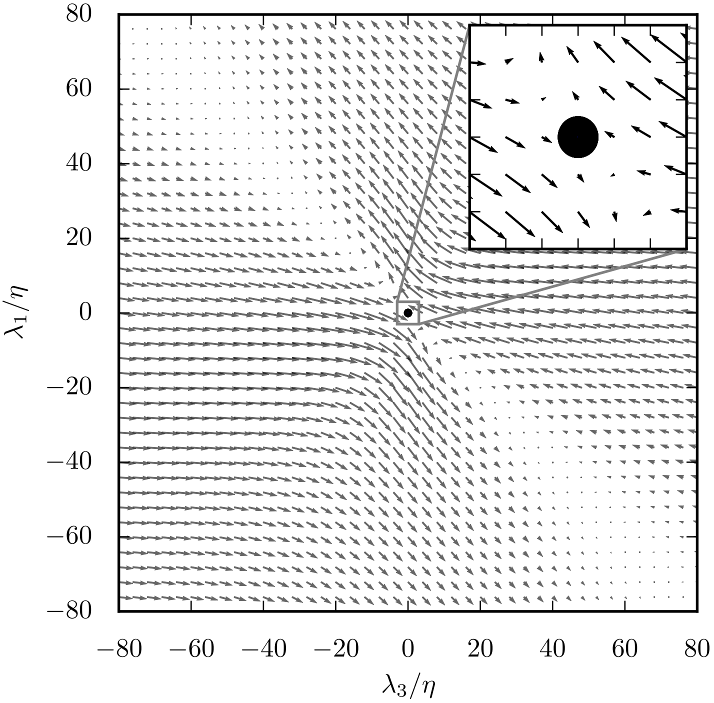

FIGURE 5.4: Projection of 5000 particles on the $\lambda_2 = 0$ plane at time $t = 0$. The particles are distributed on the surface of a sphere centered at the origin of the shear-layer structure with initial separation $|\mathbf{r}_0| = \eta$. The projection of particles onto a plane leads to overlapping of particles to form a circle.

t_B is considered as the time where the two particles remain within the same eddy of size r_0. When the particles leave the eddy, i.e, at times $t > t_B$, the particle separation transitions into Richardson's t^3 scaling (see Eq. (5.3)).

The mean square of the relative separation is computed for different initial separations in different structures. The compensated relative dispersion results are compared with the data from actual turbulence[79] in Section 5.4.1. Additionally, the existence of the Batchelor's ballistic regime and the Richardson's t^3 scaling is probed.

5.3.2 *Material lines*

A material line is an infinitesimal line composed of the same fluid particles, when evolved in time, hence studying their orientation aids in the understanding of turbulence mixing[62]. The evolution of the orientation of the material lines is studied similar to Guala et al.[65]. The orientation is examined to understand the differences between different structures. Furthermore, the results are compared with the actual turbulent flow. Material lines evolve with time according to[64, 65, 84] :

$$\frac{dl_i(t)}{dt} = \frac{\partial u_i}{\partial x_j} l_j(t), \tag{5.4}$$

where l_i represents the infinitesimal material line, $\partial u_i / \partial x_j$ refers to the velocity gradient tensor computed at the center of l_i. In the present study, material lines are assumed to continuously evolve around the origin, as the flow structures are stationary and the velocity at the origin is zero. This implies that the initially placed infinitesimal line elements at the origin do not advect, but reorient according to the same stationary velocity gradient tensor. Hence, the velocity gradient in equation (5.4) is constant in time and is computed at the origin of each flow structure. The alignment of the material lines with the straining directions is given by $\cos(\mathbf{l}, \mathbf{e}_i) = (\mathbf{l} \cdot \mathbf{e}_i)/(|\mathbf{l}||\mathbf{e}_i|)$, where $\mathbf{e}_i$ represents the eigenvectors of the strain rate tensor at the origin of the structure. A total of 10^4 material lines are considered in the present study, and their alignment for all structures is compared in Section 5.4.3 with the data presented by Guala et al.[65].

5.3.3 *Four-particle dispersion*

The tetrad dispersion is quantified by the evolution of the size and shape of the particle cloud, which are based on the separation between the different particles in a tetrahedron. The procedure to characterize the size and shape of the tetrahedron is similar to Biferale et al.[68]. At first, the coordinates are changed to obtain a new set of separation vectors[67, 68, 71], which eliminates the statistical dependence on the center of mass $\mathbf{X}_0$, where $\mathbf{X}_0 = (\mathbf{x}_1 + \mathbf{x}_2 + \mathbf{x}_3 + \mathbf{x}_4)/2$. Note that the center of mass $\mathbf{X}_0$ coincides with the origin of the structure initially. The three separation vectors are defined as[67, 68, 71]

$$\begin{aligned} \mathbf{X}_1 &= (\mathbf{x}_2 - \mathbf{x}_1)/\sqrt{2}, \\ \mathbf{X}_2 &= (2\mathbf{x}_3 - \mathbf{x}_2 - \mathbf{x}_1)/\sqrt{6}, \\ \mathbf{X}_3 &= (3\mathbf{x}_4 - \mathbf{x}_3 - \mathbf{x}_2 - \mathbf{x}_1)/\sqrt{12}. \end{aligned} \tag{5.5}$$

Then, an inertia matrix ($\mathbf{I}$) is computed as $\mathbf{I} = \boldsymbol{\rho}\boldsymbol{\rho}^T$ where the columns of the matrix $\boldsymbol{\rho}$ are the separation vectors $(\mathbf{X}_1, \mathbf{X}_2, \mathbf{X}_3)$. Then the shape and size of the tetrahedron is described by the three eigenvalues (g_i) of the inertia matrix, where $g_1 \geq g_2 \geq g_3$. The size of the tetrahedron is given by the gyration radius $R \equiv \sqrt{Tr(\mathbf{I})} = \sqrt{\sum g_i}$ and the tetrahedron volume (V) is defined as $V = \frac{1}{3}\det(\boldsymbol{\rho}) = \frac{1}{3}\sqrt{g_1 g_2 g_3}$. And finally, the shapes are characterized by $S_i = g_i/R^2$, where $S_i = 1/3$ for $i = 1, 2$ and 3 for a regular tetrahedron. If all four points are coplanar then $S_3 = 0$ and if collinear $S_2 = S_3 = 0$.

The evolution of the shape and the size of the tetrahedrons around the idealized structures is computed in terms of the eigenvalues g_i and compared to the actual turbulence cases[67, 68] in section 5.4.4.

5.4 RESULTS

Dispersion around different generic structures is investigated quantitatively and qualitatively to learn how they compare to statistics obtained in the actual turbulent flows. This is done by kinematically simulating the tracer particles around different structures, namely the shear-layer structure (SLS), the node-saddle topology (NST), and the Burgers' vortex (BV) as explained in Sections 5.2 and 5.3. The number of particle pairs (5000), material lines (10^4) and tetrahedrons (4000) investigated are fewer, but sufficient to obtain converged statistics, compared to the actual turbulent studies, where, the number is usually above 10^5. The statistics are considered converged if the convergence rate is below 10^{-4}. The convergence rate is defined as the change in statistical value with respect to the increase in the number of particle pairs or material lines or tetrahedrons. The results are discussed in the following paragraphs.

5.4.1 *Pair dispersion*

The pair dispersion is quantified in terms of the evolution of the mean square of the relative separation (MSRS) $\langle|\mathbf{r}(t) - \mathbf{r}(0)|^2\rangle$. A comparison of the MSRS for the three different structures and for initial separations $r_0/\eta = 1, 4,$ and 16 is shown in Figure 5.5. The relative separation and time (t) are normalized by the Kolmogorov length (η) and timescale (τ_η), respectively. Qualitatively, similar slopes are observed for the MSRS for the Burgers' vortex (BV), the shear-layer structure (SLS) and the node-saddle topology (NST) for time $t/\tau_\eta < 1$ and for all initial separations considered (see Fig. 5.5). However, quantitatively the relative separation for the Burgers' vortex is higher compared to the SLS and the NST. For time $t/\tau_\eta > 1$, the MSRS increases smoothly for the SLS and the NST. However, an oscillatory behavior is observed for the Burgers' vortex before rapidly increasing at later times. This oscillatory behavior is due to the circular motion of the particles in the BV, which results in the

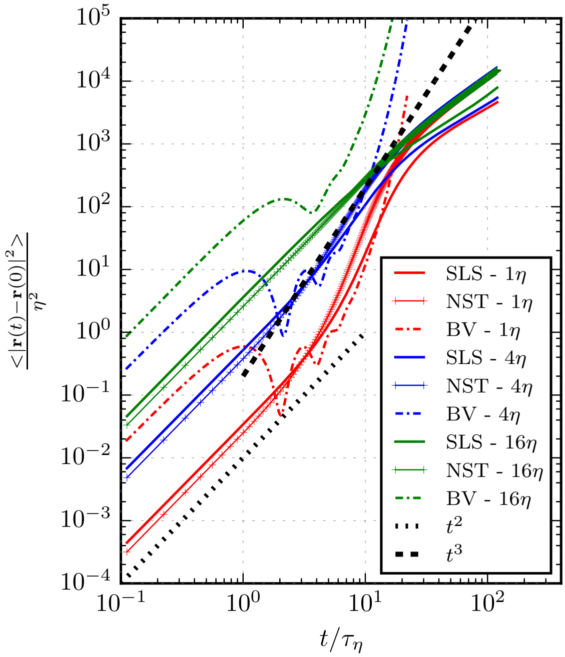

FIGURE 5.5: The comparison of the evolution of the mean square of relative separation, normalized by Kolmogorov length (η), for different structures and for different initial separations ($r_0/\eta = 1$, 4, and 16). Time t is normalized by Kolmogorov time scale (τ_η). The straight black dotted line corresponds to the Batchelor's t^2 scaling and dash-dotted line to Richardson's t^3 scaling. Dashed-dotted lines refer to the Burgers' vortex (BV), solid lines to the shear-layer structure (SLS) and lines with '+' marker to the node-saddle topology (NST).

particles approaching the initial position after every revolution. With time the oscillation fades, as the particles approach the vortex core and the stretching in the axial direction starts to dominate the particle separation. It is also noted that the statistics for the SLS and the NST are found to be approximately similar for all initial separations till $t/\tau_\eta = 20$.

The Batchelor scaling is represented by the t^2 curve in Figure 5.5. In the Burgers' vortex case, the relative separation scales with t^2 for time $t/\tau_\eta < 1$. For the SLS and the NST, the t^2 scaling is observed till $t/\tau_\eta \approx 3-4$ for the initial separations $r_0/\eta = 1$ and 4. For $r_0/\eta = 16$, Batchelor's regime is observed for a longer time, upto $t/\tau_\eta \approx 9-10$. However, there was no evidence for the Richardson's regime in the BV, SLS and NST. From all these observations, it is deduced that Batchelor's regime, where particles are influenced by their initial separation, is observed in the all three flow structures. However, the statistics around the Burgers' vortex quantitatively and qualitatively differ from the SLS and the NST after time $t/\tau_\eta = 1$.

Furthermore, the dispersion around the shear-layer structure and the node-saddle topology is compared to actual homogeneous isotropic turbulence at Taylor Reynolds number $Re_\lambda = 650$ [79]. The evolution of the compensated relative dispersion ($\langle \mathbf{r}(t)^2 - \mathbf{r}(0)^2 \rangle / \epsilon t^3$) with time is shown in Figure 5.6. Here, the dissipation ϵ is taken from the

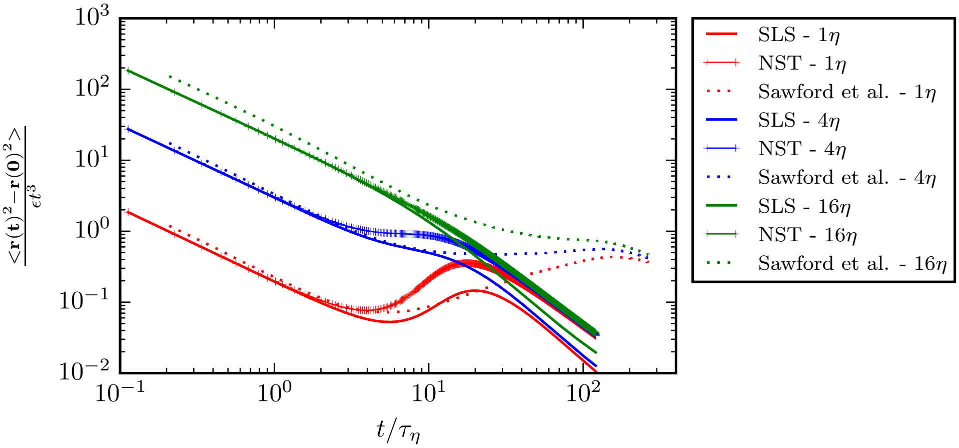

FIGURE 5.6: Comparison of the compensated relative dispersion for the shear-layer structure (SLS), node-saddle topology (NST) and actual isotropic turbulence (from Sawford et al. [79]). Results are shown for initial separations distances $r_0 = 1\eta$, 4η, and 16η.

same database employed to extract structures[82]. The initial separations investigated are $r_0/\eta = 1$, 4, and 16.

The compensated relative dispersion (Fig. 5.6) in the actual turbulence case and the SLS collapse onto each other until the time $t/\tau_\eta = 20$ for the initial separation 1η and till time $10\tau_\eta$ for $r_0/\eta = 4$ and 16. In the case of the node-saddle topology, the compensated relative dispersion is similar to the actual turbulence case till $4 - 5\tau_\eta$ for initial separations $r_0/\eta = 1$ and 4. For $r_0/\eta = 16$, the NST shows a similar trend as the SLS. Also, it can be observed that, qualitatively, the SLS is closer to actual turbulence till $t/\tau_\eta \approx 20$ than the node-saddle topology (NST) for $r_0/\eta = 1$ and 4. During the time $t/\tau_\eta \approx 30 - 100$, the compensated relative dispersion for different initial separations in the actual turbulence case undergoes transition and attains a plateau. This plateau indicates the Richardson's regime[79] and the value of the compensated relative dispersion is equal to the Richardson constant ($g \approx 0.6$, see Eq. (5.3))[79]. However, the scaling in the SLS and the NST changes to the diffusive regime, where the mean-square separation of the particles scales with t. Nevertheless, the qualitative trend of the transition from t^2 to the point where the curves for the initial separations η and 4η approach each other is similar to actual turbulence, but much shorter. The transition occurs at $t/\tau_\eta \approx 3 - 13$ in the case of the SLS and the NST compared to $t/\tau_\eta \approx 3 - 40$ for actual turbulence[79]. This quantitative difference could be due the absence of additional structures in the SLS and the NST. Batchelor[60] conjectured that the particles enter different structures when the scaling changes from the Batchelor's regime to the Richardson's regime. In the present simulations, as only single structures are considered, it is, therefore, unlikely to observe the Richardson's regime.

From all these observations, it is understood that the shear-layer structure and the node-saddle topology have quantitatively similar pair dispersion statistics to the actual turbulent flow up to $t/\tau_\eta \approx 3 - 10$, which corresponds to the Batchelor's regime. Additionally, the SLS is observed to follow the actual turbulence more closely than the NST till $t/\tau_\eta \approx 20$. However, due to the absence of multiple structures, an actual Richardson's regime cannot be observed.

5.4.2 *Instantaneous distribution of particles*

While the relative dispersion of particles by the SLS and the NST is qualitatively similar, the underlying particle distribution in physical space appears to be different, which is illustrated in this section. The distribution of particles in time for the initial separation distance $r_0/\eta = 1$ is shown for the SLS and the NST in Figures 5.7 and 5.8, respectively. The three rows of plots in these figures represent the projections on the three Cartesian planes, namely $\lambda_3 = 0$, $\lambda_2 = 0$, and $\lambda_1 = 0$ from top to bottom. The three columns from left to right show the time evolution of particles at times $t/\tau_\eta = 4$, 10, and 50, respectively.

The first row in figures 5.7 and 5.8 shows the particle distribution on the plane spanned by the extensive principal straining directions λ_1 and λ_2 for the SLS and the NST, respectively. Initially at $t/\tau_\eta = 0$, the particles are distributed on a sphere leading to the circular distribution in the projections (see Fig. 5.4). With time, the projected distribution of particles develops an ellipsoidal shape due to the higher rate of stretching in the λ_1 direction compared to the intermediate λ_2 direction ($t/\tau_\eta =$ 4 and 10). Furthermore, the size of the ellipse increases, because the stretching rate in both directions is positive. At later times, the ellipsoid splits into two (e.g. at $t/\tau_\eta =$ 50).

The second row in the Figure 5.7 correspond to the particle distribution on the plane with the most extensive and the compression principal strain rates. The particles get stretched along the shear layer (see Fig. 5.9 for the associated velocity vectors) with increasing time. In this projection, the particles are distributed along a line, which is at an 18 degree angle with respect to the direction of the most stretching principle strain λ_1 at $t/\tau_\eta = 4$ (see Fig. 5.7d). At later time $t/\tau_\eta = 50$, the projected particle distribution approaches the 45 degree diagonal (Fig. 5.7f). However for the NST, the

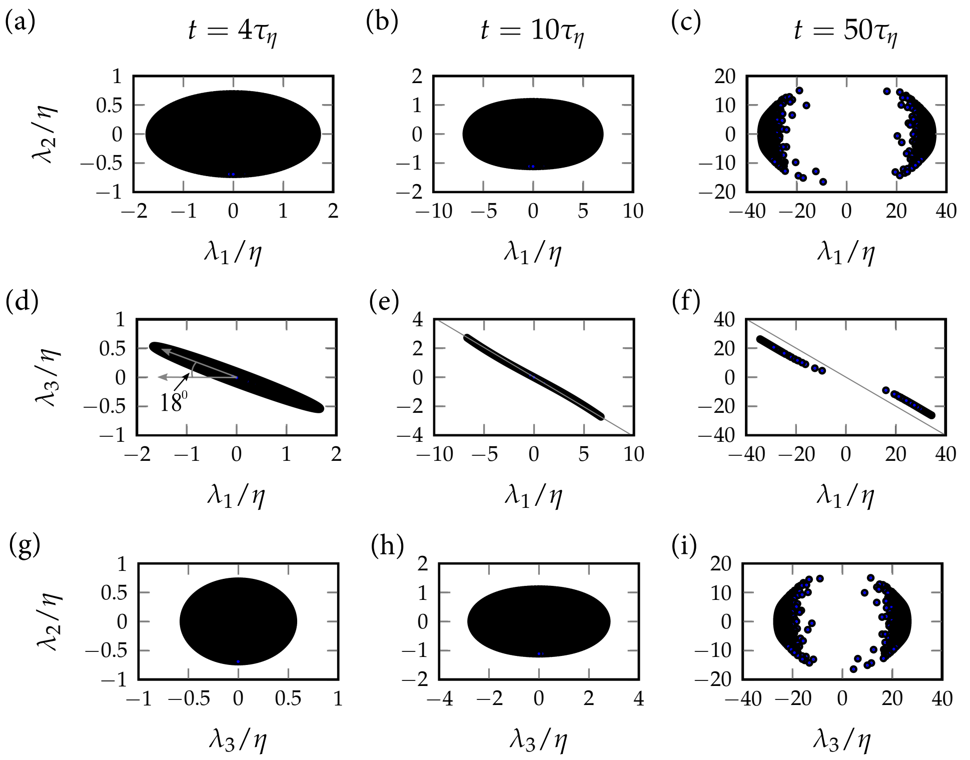

FIGURE 5.7: Evolution of 5000 particles in the shear-layer structure with time (columns) projected on three different planes (rows). Columns from left to right show particle distribution at times $t/\tau_\eta = 4,$ 10 and 50. The projections of the 5000 particles overlap, which initially appear as one ellipsoid.

particles on the same plane are stretched along the λ_1 and compressed in the λ_3 direction (Fig. 5.8). This is attributed to the absence of rotation/vorticity in the node-saddle topology. The NST particle distribution essentially forms a line in the λ_1 direction, as observed in the second row of the Figure 5.8.

The distribution of particles for the SLS and the NST is also different in the ($\lambda_1 = 0$) plane, which is observed in the third row of Figures 5.7 and 5.8, respectively. The difference is again attributed to the presence of rotation in the shear-layer. Due to the rotation in the SLS, the particles get distributed along the shear-layer, thereby, actually spreading the particles in the direction of compressive strain (λ_3). However, the absence of rotation in the NST causes the particles to collapse approximately onto a line along the λ_2 axis at time $t/\tau_\eta = 50$ (see Fig. 5.8g-i).

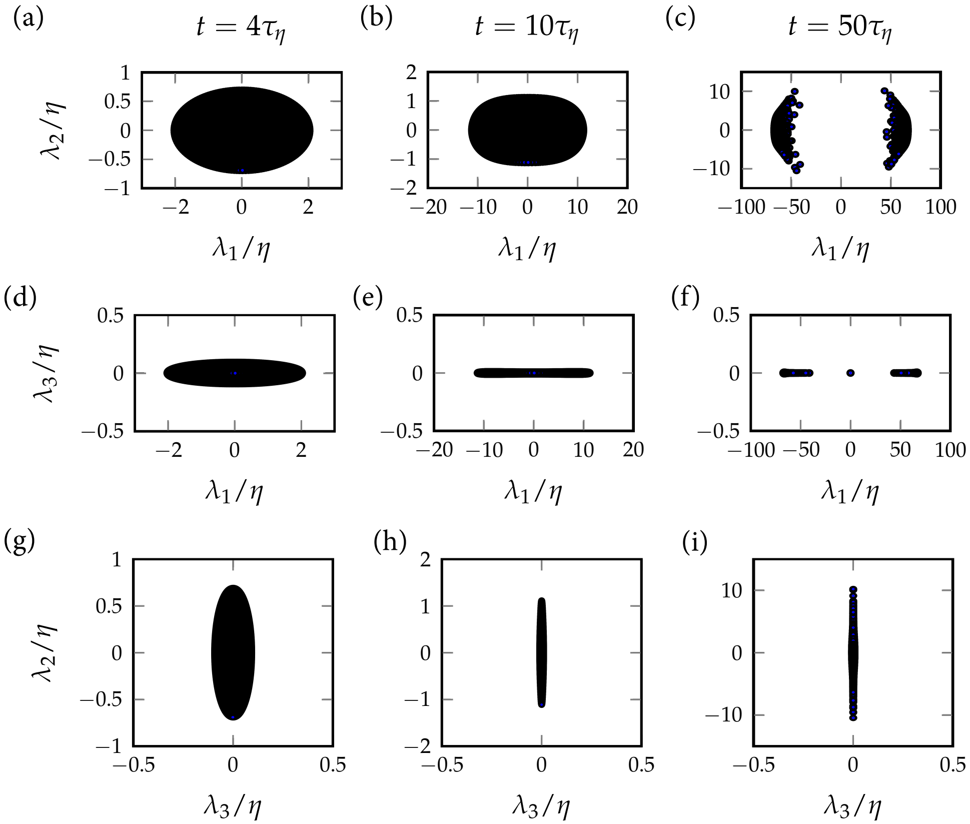

FIGURE 5.8: Evolution of 5000 particles in the node-saddle topology with time (columns) projected on three different planes (rows). Columns from left to right show particle distribution at times $t/\tau_\eta = 4,$ 10 and 50. The projections of the 5000 particles overlap, which initially appears as one ellipsoid.

From these observations, it is concluded that the particles in the node-saddle topology at $t/\tau_\eta > 10$ form a sheet spanning the λ_1 and λ_2 directions. In contrast, the particle sheet in the shear-layer structure is at an angle with the λ_1 and λ_3 directions, while it is still aligned with the λ_2 direction. Hence, the particles are observed to spread in the direction of the most compressive strain λ_3. The pair dispersion statistics i.e., the mean square of relative separation, of the NST and the SLS are found to be similar even though the particles in the node-saddle topology do not move away from the origin in the compression direction. However, the observed differences in particle sheet formation are important when considering the orientation of material lines and the geometry of four particle dispersion as shown below.

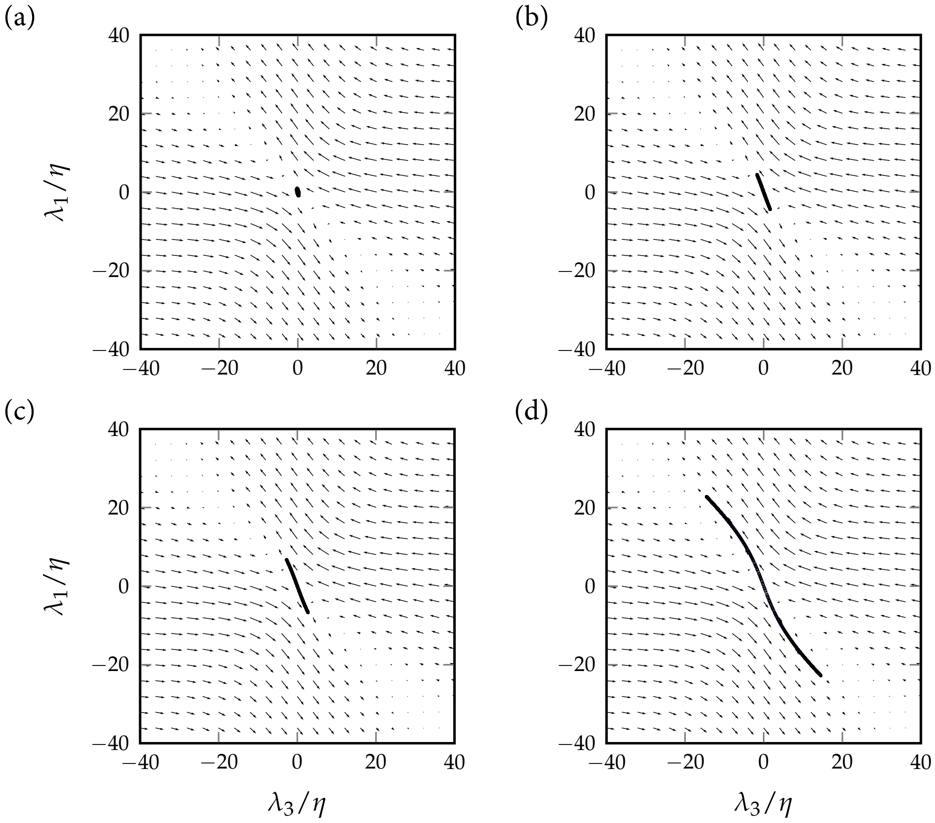

FIGURE 5.9: (a)-(d) correspond to the distribution of particles in the shear-layer structure projected on the plane $\lambda_2 = 0$ at times $t/\tau_\eta = 4,\ 8,\ 10,$ and 25, respectively. The initial separation is 1η. With time, the particles align themselves along the shear-layer forming a sheet.

5.4.3 *Material lines*

The probability density function (PDF) of the orientation of the material lines ($\mathbf{l}$) with respect to the straining directions ($\mathbf{e}_i$), as given by $cos(\mathbf{l}, \mathbf{e}_i)$, is computed for different structures. Initially, the material lines are randomly oriented, hence, the PDF of $cos(\mathbf{l}, \mathbf{e}_i)$ is flat for all angles and will not be shown in the figure. With time, the alignment of the material lines changes with respect to the straining directions. The alignment at time $t/\tau_\eta = 4.0$ is shown in Figure 5.10 and will be discussed in the following paragraphs. The material line alignment will be compared to the particle distributions (Fig. 5.7 and 5.8) as the distance traveled by particles is small and is still dependent on the initial conditions.

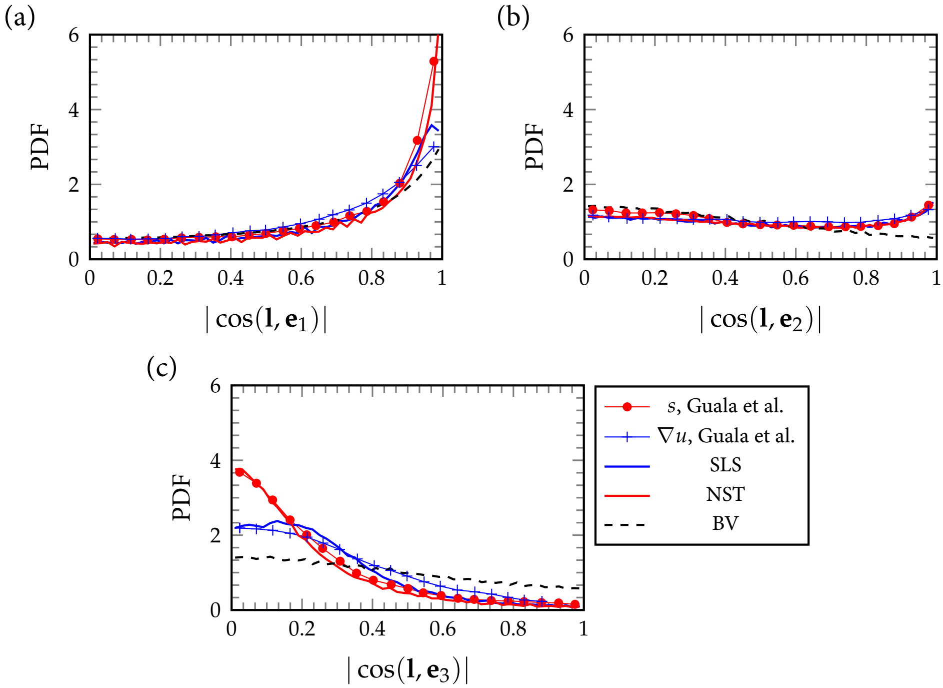

FIGURE 5.10: Probability density function of $cos(\mathbf{l}, \mathbf{e}_i)$ at $t/\tau_\eta = 4.0$ for the shear-layer structure (SLS), the node-saddle topology (NST) and the Burgers' vortex (BV). The lines 's' and '∇u' represent the alignment computed using the strain-rate tensor and the velocity gradient tensor in actual turbulence, respectively, which is data from Guala et al.[65]

Figure 5.10a describes the PDF of the alignment of the material lines with the most stretching direction, i.e., $cos(\mathbf{l}, \mathbf{e}_1)$. The material lines develop a strong preferential alignment with the most stretching direction for all structures. The alignment is strongest in the case of the node-saddle topology compared to the shear-layer structure and is weakest in the case of the Burgers' vortex. This can also be observed in the particle distribution plots in Figures 5.7 and 5.8 at $t/\tau_\eta = 4$, where, the particles are strongly aligned in the most stretching direction in the NST (see Fig. 5.8) compared to the weaker alignment in the SLS (Fig. 5.7). Also, the peak in the PDF occurs at $|cos(\mathbf{l}, \mathbf{e}_1)| = 0.97$ for the SLS, which corresponds to a 14 degree angle. Similarly in the particle distribution plots at the corresponding time instant, the angle between the particle distribution and the most stretching direction is 18 degrees (Fig. 5.7d). For the NST, however, the peak is at $|cos(\mathbf{l}, \mathbf{e}_1)| = 1$, which corresponds to 0 degrees. This is consistent with the clustering of particles along the λ_1 axis for the NST (Fig. 5.8d).

The PDF of the alignment of the material lines with the intermediate straining direction is shown in Figure 5.10b. The material lines in the shear-layer structure and the node-saddle topology show a slight tendency for alignment with the intermediate direction, which has a finite positive strain. This can also be observed in the particle distribution at $t/\tau_\eta = 4$ (Figures 5.7 and 5.8). However, the material line alignment with $\mathbf{e}_2$ in the Burgers' vortex decreases as $\mathbf{e}_2$ corresponds to the compressive strain.

Figure 5.10c shows material line alignment with the compression direction ($\mathbf{e}_3$). For all structures, it can be observed that the material lines tend to align perpendicular to the compression direction ($\mathbf{e}_3$). The material lines in the NST show the strongest perpendicular alignment with the compression direction compared to the SLS and the BV. This behavior can also be observed in the $\lambda_2 = 0$ plane of the particle distribution plots at time $t/\tau_\eta = 4$. In case of the NST, the particles are clustered and stretched along the λ_3 direction, which is perpendicular to the direction of the compressive strain (see Fig. 5.8d). However in the SLS (see Fig. 5.7d), the projected particles on $\lambda_2 = 0$ plane are distributed along a line at an angle of 72 degrees with the compressive strain direction. This is consistent with the PDF of $cos(\mathbf{l}, \mathbf{e}_3)$ where the peak occurs between 0.1 and 0.2, which corresponds to $84 - 78$ degrees. Since, this angle is computed in three dimensional space, it is slightly higher than the angle (72 degrees) computed based on the 2-d projection of the particles.

The material line alignments reported in actual turbulent flows[65] are also shown in Fig. 5.10. Guala et al.[65] considered two different velocity gradient tensors, namely the strain-rate tensor (s) and the velocity gradient tensor (∇u), to compute the evolution of material lines (see right-hand side of Eq. (5.4)). For the case studied by Guala et al.[65], s and ∇u evolve in time, whereas for the SLS, the BV and the NST the velocity gradient is fixed. From Fig. 5.10, it can be observed that the alignments for the SLS and the NST are comparable to the alignments computed using the '∇u' and the 's' in actual turbulent flows[65], respectively. The similarity observed between the SLS and the actual turbulent flow (∇u) could be due to the fact that the SLS represents the average flow field around a point in a turbulent flow and includes both strain and rotation. The NST is obtained by symmetrizing the SLS (Section 5.2.3), so it only contains strain and no rotation. Again due to the symmetrization, the velocity gradient tensor used to compute alignments in the NST is same as the strain-rate tensor of the SLS. Hence, this could explain the similarity between the NST and the alignment computed from the strain-rate tensor (s) in actual turbulent flow (see Fig. 5.10).

From these observations, it is clear that the SLS and the NST show differences in the alignment of material lines, which is consistent with the particle distributions observed in Section 5.4.2. These differences are explained by the fact that the SLS contains vorticity, whereas the NST does not. On the other hand, the Burgers' vortex (BV) clearly differed from the SLS and the NST cases, because it has rotational symmetry and two compression directions ($\mathbf{e}_2$, $\mathbf{e}_3$) leading to the identical alignment of material lines with $\mathbf{e}_2$ and $\mathbf{e}_3$. In contrast, the SLS and the NST have two extensive directions $\mathbf{e}_1$ and $\mathbf{e}_2$. Additionally, the alignments in the SLS and the NST, where the flow field does not evolve in time, are comparable to the results of Guala et al., which are computed in a continuously evolving turbulent flow. Therefore, it is concluded that the SLS structure yields similar material line alignment as the actual turbulent flows, at least up to $t/\tau_\eta = 4$.

5.4.4 *Four particle dispersion*

The evolution of four particle dispersion is characterized by the shape and size of the tetrahedrons, which is further quantified in terms of the eigenvalues (g_i) of the inertia matrix ($\boldsymbol{\rho}$) as discussed in Section 5.3. Figure 5.11 shows the evolution of the eigenvalues $\langle g_i \rangle$ for four cases namely, the Burgers' vortex (BV), the shear-layer structure (SLS), the node-saddle topology (NST), and actual isotropic turbulence ($Re_\lambda = 280$) from Biferale et al.[68]. The volume ($V = \frac{1}{3}\sqrt{g_1 g_2 g_3}$) of the tetrahedrons up to $t = 4\tau_\eta$ was found to be constant in the case of the BV, the SLS, and the NST, which is similar to the results presented in Biferale et al.[68] for actual isotropic turbulence.

The largest eigenvalue, g_1, is qualitatively and quantitatively similar till $10\tau_\eta$ in all considered cases (see Fig. 5.11a). However, for g_2 and g_3 the Burgers' vortex shows a different trend compared to the other cases (Figures 5.11b and 5.11c). For the BV, both eigenvalues, hence the shape parameters S_2 and S_3 approach zero with time. This means that the particles of a tetrahedron become collinear, which is due to the compression of the particles in two compressive straining directions (see Section 5.3.3). For the SLS and the NST, the second eigenvalue g_2 increases with time and follows the actual turbulence curve till $t/\tau_\eta \approx 4 - 5$. At later times, g_2 remains similar for the SLS and the NST, but deviates in terms of its magnitude from the actual turbulence case[68]. Finally, the value of the third eigenvalue, g_3, decreases initially for all cases. While g_3 decreases and tends to go to zero, g_1 and g_2 are increasing for the SLS, the NST, and the actual turbulence, which means that the particles of the tetrahedron are becoming more coplanar. This is observed in Figures 5.7 and 5.8, where particles form a sheet in the case of the SLS and the NST, respectively. Furthermore, the eigenvalue g_3 for the NST decreases and then slowly tends to zero after time $10\tau_\eta$, which is different from the SLS, where g_3 decreases and then increases again. The increase in g_3 is qualitatively similar to actual turbulence. The eigenvalue g_3 increases in the SLS as the

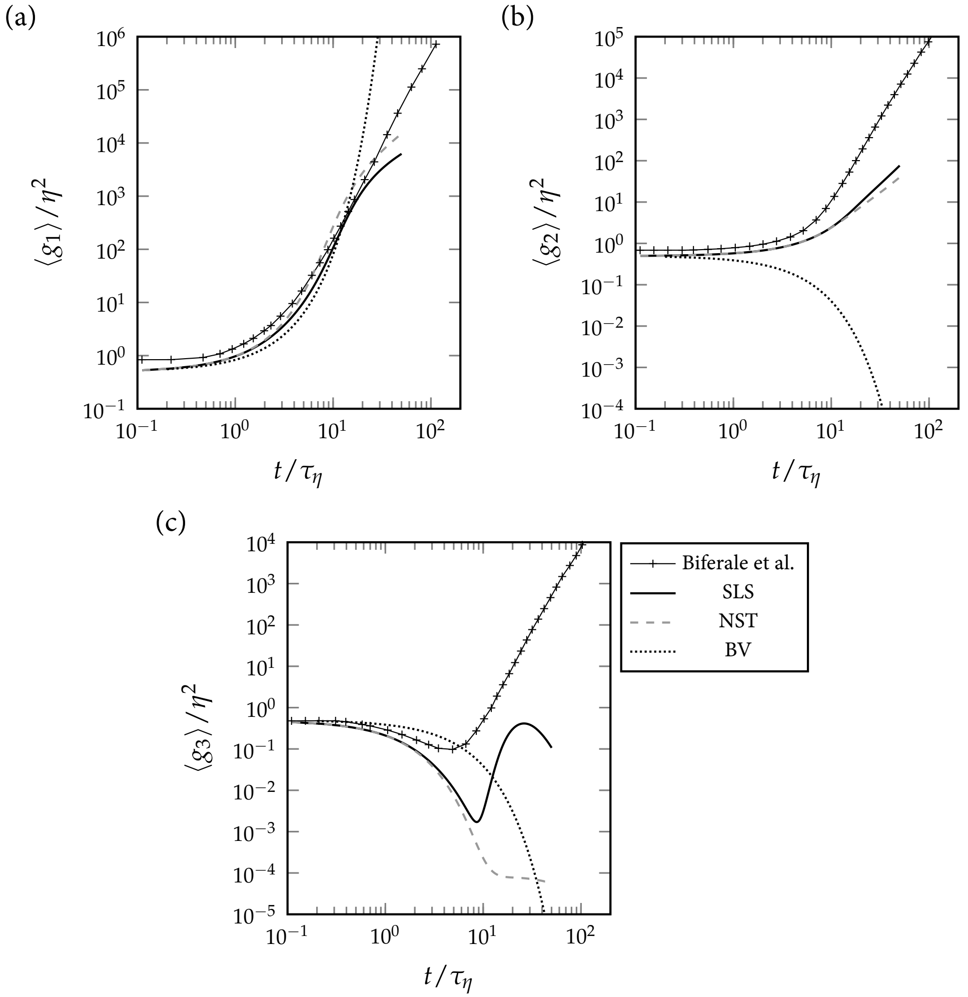

FIGURE 5.11: The comparison of the eigenvalues (g_i) of the inertia matrix with time (t/τ_η) between the shear-layer structure (SLS), the node-saddle topology (NST), the Burgers' vortex (BV) and the data from the actual isotropic turbulence case by Biferale et al.[68] for the tetrahedrons of edge length η. Time (t) and eigenvalues are normalized by means of the Kolmogorov timescale (τ_η) and length scale (η).

particles sheet deforms leading to the loss of coplanarity. This can also be observed in the plane $\lambda_2 = 0$ in Figure 5.9, where the straight particles sheet ($t/\tau_\eta = 4$) starts deforming and develops a slight undulation at time $t/\tau_\eta = 10$ and is fully deformed at $t/\tau_\eta = 25$ leading to the loss of coplanarity. The deformation of the sheet is associated with the particles moving away from the saddle point at the origin of the SLS and approaching the adjacent vortices[7](Fig. 5.9). This causes a change in the particle velocity in the direction perpendicular to the shear-layer, which causes the loss in coplanarity. The formation of two sheets (see Fig. 5.7f) may be the reason for the decrease in eigenvalue g_3 after $t/\tau_\eta = 25 - 30$ in the SLS. Hence, the shear-layer structure qualitatively shows a similar trend to that of the actual turbulence case up to $t/\tau_\eta = 20$, whereas the NST and the BV deviate.

5.5 CONCLUSIONS

In this chapter, the dispersion of tracer particles by idealized flow structures was studied qualitatively and quantitatively and compared to the actual turbulent flow. The dispersion was described by the pair and the tetrad dispersion statistics and the evolution of material lines. The flow structures considered were the Burgers' vortex (BV), the shear-layer structure (SLS), and the node-saddle topology (NST). All the simulations were kinematic in nature as the flow structures did not evolve in time.

The pair dispersion was quantified in terms of the mean square of relative separation. The pair dispersion statistics were qualitatively similar in all three structures for very short time, up to $t = 1\tau_\eta$. Moreover, the Batchelor's regime (t^2 scaling), where the particles are influenced by their initial separation, was observed in all flow structures. However, the relative separation for the Burgers' vortex was qualitatively and quantitatively different from the shear-layer structure and the node-saddle topology after time $t/\tau_\eta = 1$. In particular, the separation showed an oscillatory behavior for the Burgers' vortex, which was attributed to the circular motion of the particles, causing the particles to approach their initial position after every revolution. The compensated relative dispersion for actual turbulence[79] was compared to the SLS and the NST. The SLS and the NST exhibited quantitatively similar statistics as actual turbulent flow[79] till $t/\tau_\eta \approx 3 - 10$ depending on the initial separation, which corresponded to the Batchelor's regime. Richardson's regime was not observed in the statistics of the SLS and the NST. This could be attributed to the absence of other structures, as opposed to the actual turbulence cases, which are composed of many flow structures.

The probability density functions of the orientation of material lines with respect to the principal straining directions was computed for the different structures and compared to actual turbulent flow data[65]. Again, the Burgers' vortex clearly differed due to the presence of two compressive straining directions as opposed to two stretching directions in the case of the SLS and the NST. The SLS and the NST exhibited similar PDFs as the actual turbulence case[65] at $t = 4\tau_\eta$. As the SLS represents the average flow around a point in the turbulent flow, the alignments in the SLS were found to be comparable to the evolution of material lines computed using the velocity gradient tensor in actual turbulent flows. On the other hand, the velocity gradient utilized to compute alignments in the NST is the symmetric part of the velocity gradient tensor used in the SLS. Hence, the velocity gradient tensor in the NST only contains strain as opposed to strain and rotation in the SLS. This could be the reason for similarity between the NST and the evolution of material lines computed using the strain-rate tensor in actual turbulent flows[65]. Additionally, the preferential alignment angles for the material lines in the SLS were found to be similar to the angles at which the particles clustered in the particle distribution plots.

Finally, the tetrad dispersion was quantified by the eigenvalues of the inertia tensor of the tetrahedron, which characterized the evolution of the size and shape of the tetrahedron. Their evolution was computed for all structures and compared to the statistics for actual turbulent flow from Biferale et al.[68]. The largest eigenvalue g_1 was similar in all the three cases. For the Burgers' vortex the eigenvalues g_2 and g_3 approached zero with time, which meant the particles of the tetrahedron became collinear. The intermediate eigenvalue g_2 in the SLS and the NST was identical to the actual turbulence case for time $4-5\tau_\eta$, after which the eigenvalue deviated quantitatively. Finally, the third eigenvalue initially decreased for all cases. However, it increased again for the SLS after time $10\tau_\eta$, which is qualitatively similar to actual turbulence. The initial decrease in g_3 in the SLS and NST lead to coplanarity as the shape parameter S_3 tended to zero. This was also observed in the particle distribution plots. Then, the increase in the third eigenvalue in the SLS was attributed to the loss of coplanarity due to the deformation of particle sheet as observed in the particle distribution plots at the corresponding times.

To conclude, the shear-layer structure showed many quantitative (till $2-4\tau_\eta$) and qualitative (till $20\tau_\eta$) similarities when compared to the actual turbulence case (see Fig. 5.6 and 5.11). The Burgers' vortex deviated the most, both quantitatively and qualitatively. The node-saddle topology did exhibit some similarities to actual turbulent flow statistics in terms of the particle pair dispersion, but it did not capture a number of geometrical features associated with the material lines and tetrad dispersion.

6

CONCLUSIONS AND RECOMMENDATIONS

In this thesis, turbulence was studied in terms of coherent structures. Among the coherent structure descriptions of turbulence, the hairpin packet or vortex packet model was considered due to its association with Reynolds shear stress, which is further connected to the drag. Few unsolved questions in the vortex packet model and its dynamics were addressed in this study. In this chapter, the main conclusions are briefly summarized as they are described in detail in every chapter. In the following paragraphs conclusions and future work linked to each chapter will be discussed.

6.1 AUTO-GENERATION IN WALL-TURBULENCE

The question of how threshold strength vortices may come into existence, and the role of low-speed streaks in auto-generation was addressed in Chapter 2 by performing simulations in an ideal scenario. It was shown that the two non-auto-generating vortices could merge to create a threshold strength vortex and subsequently generate a new vortex. Additionally, some non-merging cases were also observed to auto-generate, when the stream-wise separation between vortices was small ($\Delta x^+ < 120$ wall units). Thus, the auto-generation from two weak eddies was found to be dependent on the initial stream-wise separation as a small separation emulates the increase in threshold strength by the superposition of their associated velocity fields. From these observations, it was concluded that the interaction of weak vortices could lead to auto-generation either by merging, which leads to the creation of a threshold strength vortices, or by amplification of the perturbation velocity due to the small initial stream-wise separation.

Furthermore, the addition of a low-speed streak to a non-auto-generating vortex did not result in the generation of new vortices. From this and the above observations, the onset of auto-generation was probed in detail, which resulted in modifying the existing auto-generation mechanism. The modified mechanism highlighted that the ejection events and their interaction with surrounding flow is important for auto-generation. This differed from the work of Zhou et al.[28] where the kink formation in legs of the hairpin vortex leading to the auto-generation is due to mutual and self induction of stream-wise legs. Whereas in the modified mechanism presented in this thesis, the kink formation is the consequence of the shear layer roll-up and ejection events. Also, this modified mechanism can describe the onset of auto-generation for both, a vortex with a single stream-wise leg and a vortex with two stream-wise legs unlike previous descriptions. This strengthens the vortex packet model as single legged vortices are more widely observed in actual turbulent flows than two legged vortices.

It should be noted that few parts of the study in Chapter 2 are qualitative in nature. The threshold strength required to generate a new vortex from an extracted parent vortex at different wall-normal heights at low Reynolds numbers has been quantitatively studied by Zhou et al.[28] and Kim et al.[33]. However, this has not been quantified extensively at high Reynolds numbers. Additionally, the initial condition containing two stream-wise legs has not been extracted at high Reynolds numbers. Hence, initial condition needs to be extracted at high Reynolds numbers, and also a detailed exploration needs to be performed to understand the effect of the wall-normal distance and Reynolds numbers scaling on auto-generation in ideal simulations. This information could help in identifying the threshold strength vortices in actual turbulent flows. Secondly, the modified auto-generation mechanism is described qualitatively, where the vortex head is rapidly lifted up by the ejection events, which further blocks the incoming flow leading to auto-generation. Hence, a quantitative description of the threshold value for an ejection event required to lift the vortex head and cause auto-generation needs to be studied.

The generation of new vortices was studied in transitional boundary layers[39, 45, 85–87]. In these studies, it has been shown that a varicose-like breakdown leads in the formation of $\wedge$ or horse-shoe structures[39, 86], which are also referred as hairpin vortices. This varicose-like breakdown is based on Kelvin-Helmholtz instability. Additionally, similar to the present study on auto-generation, shear-layers were observed in these studies. Hence, in the future one could explore a possible connection between the varicose-like breakdown and auto-generation. If such a connection exists, it could result in integrating different views on boundary layer turbulence, thus improving our understanding of turbulence.

6.2 AUTO-GENERATION IN TURBULENT FLOW AND ITS TIMESCALE

The generation of new vortices from cane-shaped or asymmetric vortices was observed in actual fully developed turbulent channel flow at friction Reynolds number $Re_\tau = 180$ (see Chapter 3). The modified auto-generation mechanism for single legged vortices (asymmetric vortices) was found to be consistent with the observations. Furthermore, the timescale of auto-generation was observed to be $10 - 15$ time wall units, which was similar to experimental results by Jodai and Elsinga[36]. However, this timescale is an order of magnitude smaller than the idealized simulations. This small time scale shows how quick the vortices can be generated in a packet. Thus explaining one way how vortices can get clustered in a vortex packet, thereby improving the existing model. Additionally, this timescale also represents the generation of ejection events, hence, it could be utilized to modify flow in the case of active drag reduction or to create turbulence. However, due to the difficulties associated with the objective and automated identification of auto-generation and vortex packets, the timescale presented in this study is not a statistical one.

The development of an objective method to detect auto-generation in the future is important to confirm the timescale of auto-generation. Additionally, a link between this time scale and the time scale of the generation of ejection events studied by hot-wire measurements[88–91] needs to be explored. This link could simplify the three-dimensional study of the timescale of auto-generation to one-dimension.

6.3 SHEAR-LAYER STRUCTURE AND VORTEX PACKET

The average shear-layer structure (SLS), which appears in different turbulent flows as shown by Elsinga and Marusic[7], was identified in an instantaneous turbulent channel flow, thereby demonstrating the structure is not the result of averaging. It was also shown that the two consecutive co-rotating vortices in a vortex packet can be viewed in a different frame of reference as the shear-layer structure.

One of the main implication of this study is that this could aid in developing an objective method to identify vortex packets and auto-generation as discussed in Section 4.3.3. Further, this objective method could be utilized to study the statistical relevance of the vortex packets and auto-generation.

The average SLS has been detected in many different kinds of turbulent flows. So in the future, the instantaneous existence of SLS can be probed in other flows following the method described in this thesis. And if it exists in different flows, for example in isotropic flows, then, there is a possibility of finding vortex packets as the dissipation forms long and large sheets[58] similar to the observations of vortex packets in the channel flow. Additionally, similar study on the temporal evolution of generation of a vortex could also be performed.

6.4 DISPERSION AROUND IDEALIZED FLOW PATTERNS

Tracer dispersion was studied around different idealized flow structures, namely, the Burgers' vortex, the shear-layer structure, and the node-saddle topology. It was shown that the shear-layer structure resembled the actual turbulent flows quantitatively for times $2 - 4\tau_\eta$ and qualitatively up to $20\tau_\eta$, respectively. The node-saddle topology showed few similarities. However, the Burgers' vortex deviated the most, both quantitatively and qualitatively.

A few studies[92–95] on pollution dispersion in urban environments have shown that the low-momentum zones in the flow are associated with the removal of pollutants between high-rise buildings and narrow streets. Even though low momentum zones in actual flows has been studied in two-dimensions[1, 96], however it is difficult to identify and study them in three-dimensions. These low momentum zones are shown to be associated with vortex packets[1], where, two successive co-rotating vortices can be viewed as the shear-layer structure. Hence, a low momentum zone could be modeled as bounded by the shear-layer structure and the dispersion around it can be studied in an idealized way, which, further could be utilized in modeling urban environments.

To conclude, some aspects of turbulence were studied at low Reynolds number in terms of coherent structures and the existing vortex packet model was improved in the following ways. First, the interaction of weak vortices was shown to create a threshold strength vortex, which further could auto-generate. Second, three-dimensional vortex packets in simulated turbulent flows were observed, thereby strengthening the relevance of the vortex packets to describe actual three-dimensional flows. Third and final, the time scale of auto-generation in the simulated turbulent flow at $Re_\tau = 180$ was found to be short, i.e., $10 - 15$ wall time units (ν/u_τ^2). Additionally, a vortex packet was linked to the shear-layer structure, and thereby showing two co-rotating vortices in a packet can be viewed in different frame of reference as shear-layer structures. Finally, the tracer particle dispersion statistics around the shear-layer structure were observed to better resemble actual turbulent flow statistics for short times compared to the statistics for the node-saddle topology and the Burgers' vortex.

A

APPENDIX : DIRECT NUMERICAL SIMULATION

In this appendix, few details on the direct numerical simulation code are given. And then the turbulent statistics are compared and validated against the data provided on website http://turbulence.ices.utexas.edu/[51].

A.1 DNS CODE DETAILS

The skew-symmetric, non-dimensional Navier-Stokes equations are solved in the code. The skew-symmetric form is used because it is energy conserving. In the following subsections, time integration scheme is described and the details on spatial-discretization are given.

A.1.1 *Non-dimensionalized Navier Stokes equation*

$$\begin{aligned}
&\frac{\partial u_i}{\partial x_i} = 0 \\
&\frac{\partial u_i}{\partial t} + \frac{1}{2}\left(u_j\frac{\partial u_i}{\partial x_j} + u_i\frac{\partial u_j}{\partial x_j} + \frac{\partial(u_j u_i)}{\partial x_j}\right) = -\frac{\partial p_i}{\partial x_i} + \frac{1}{Re_\tau}\frac{\partial^2 u_i}{\partial x_i^2}
\end{aligned}$$

where Re_τ is given by $u_\tau H/\nu$. Non-dimensional scales used in above equations are:

- Full channel height (H) for length.
- friction velocity $u_\tau(=\sqrt{\tau_w/\rho})$ for velocity.
- ρu_τ^2 for pressure.
- H/u_τ for time.

A.1.2 *Time Integration: Runge-Kutta scheme*

Few definitions :

$$
\begin{aligned}
&\mathrm{C}(u_i) = \frac{1}{2}\left(u_j \frac{\partial u_i}{\partial x_j} + u_i \frac{\partial u_j}{\partial x_j} + \frac{\partial (u_j u_i)}{\partial x_j}\right) \\
&\mathrm{D}(u_i) = \frac{1}{Re_\tau} \frac{\partial^2 u_i}{\partial x_i^2} \\
&\frac{\partial p_b}{\partial x_i} \text{ a constant pressure gradient} \\
&n - \frac{1}{2} \text{ is given by m} \\
&n + \frac{1}{2} \text{ is given by m+1}
\end{aligned}
$$

Runge-Kutta: Step 1

$$
\begin{aligned}
u_i^* &= u_i^n + dt \cdot \frac{32}{60}\left(-\frac{\partial p_b}{\partial x_i} - \frac{\partial p^m}{\partial x_i} - C(u_i^n) + D(u_i^n)\right) \\
\frac{\partial^2(\delta p)}{\partial x_i^2} &= \frac{1}{dt(\frac{32}{60})} \cdot \frac{\partial u_i^*}{\partial x_i} \\
p^{m*} &= p^m + \delta p \\
u_i^{n*} &= u_i^* - dt \cdot \frac{32}{60} \cdot \frac{\partial(\delta p)}{\partial x_i}
\end{aligned}
$$

Runge-Kutta: Step 2

$$
\begin{aligned}
u_i^{**} &= u_i^{n*} + dt \cdot \frac{8}{60}\left(-\frac{\partial p_b}{\partial x_i} - \frac{\partial p^{m*}}{\partial x_i}\right) + dt \cdot \frac{25}{60}\left(-C(u_i^{n*}) + D(u_i^{n*})\right) \\
&\quad - dt \cdot \frac{17}{60}\left(-C(u_i^n) + D(u_i^n)\right) \\
\frac{\partial^2(\delta p)}{\partial x_i^2} &= \frac{1}{dt(\frac{8}{60})} \cdot \frac{\partial u_i^{**}}{\partial x_i} \\
p^{m**} &= p^{m*} + \delta p \\
u_i^{n**} &= u_i^{**} - dt \cdot \frac{8}{60} \cdot \frac{\partial(\delta p)}{\partial x_i}
\end{aligned}
$$

Runge-Kutta: Step 3

$$\begin{aligned}
u_i^{***} &= u_i^{n**} + dt \cdot \frac{20}{60}\left(-\frac{\partial p_b}{\partial x_i} - \frac{\partial p^{m**}}{\partial x_i}\right) + dt \cdot \frac{45}{60}\left(-C(u_i^{n**}) + D(u_i^{n**})\right) \\
&\quad - dt \cdot \frac{25}{60}\left(-C(u_i^{n*}) + D(u_i^{n*})\right) \\
\frac{\partial^2(\delta p)}{\partial x_i^2} &= \frac{1}{dt(\frac{20}{60})} \cdot \frac{\partial u_i^{***}}{\partial x_i} \\
p^{m+1} &= p^{m**} + \delta p \\
u_i^{n+1} &= u_i^{***} - dt \cdot \frac{20}{60} \cdot \frac{\partial(\delta p)}{\partial x_i}
\end{aligned}$$

A.1.3 *Spatial discretisation*

Discrete fast Fourier transforms (FFTW)[48] are used to compute first and second order derivatives in the periodic directions x, y. In wall normal direction(z), 6^{th} order compact finite-difference schemes described in Boersma[49, 50] are used. Velocities u, v and pressure p are located at cell centers. Wall normal velocity (w) is in staggered configuration and is located at nodes. Momentum equation is calculated at respective velocity points. Continuity equation or Poisson equation is solved at pressure points. Time-step is computed from the CFL condition mentioned in Simens et al.[97].

A.2 CODE VALIDATION

Present DNS code was compared and validated against the data provided on website http://turbulence.ices.utexas.edu/[51]. Details comparing the domain size, grid size, friction Reynolds number and simulation time is given in table A.1.

In present simulations, 'Low res' and 'High res' refer to low and high resolution (number of grids), respectively. Figures A.1 to A.4 show the comparison between the turbulent statistics. On the top of each plot, the difference (Δ) between the data obtained from Lee and Moser[51] and the present simulations is plotted ($\Delta =$ (Lee & Moser)-(Present simulations)). The data of Lee and Moser[51] was linearly interpolated to get data at the grid points of present simulations. From all the figures, it is observed that the present DNS statistics are in good agreement with the statistics of Lee and Moser[51]. And the difference plots (above every plot) show no trend, except sometimes the Lee and Moser[51] statistics are slightly higher than present statistics, which could be due to higher Re_τ. It is observed that $\langle u'^{+}_{rms} \rangle$ for Lee & Moser is higher

TABLE A.1: Comparison of the simulation parameters in the present DNS and Lee and Moser[51]. Here $Re_\tau = u_\tau h/\nu$ represents friction Reynolds number based on half channel height (h). Domain and grid sizes in stream-wise and span-wise directions is given by L_x & Δx^+, and L_z & Δz^+, respectively. Δy_w^+ and Δy_c^+ represent grid sizes at wall and channel core, respectively. Finally, simulation time is given by tu_τ/h.

Simulation	Re_τ	L_x/h	L_z/h	Δx^+	Δy_w^+	Δy_c^+	Δz^+	tu_τ/h
Lee and Moser	182	8π	3π	4.5	0.074	3.4	3.1	31.9
Present (Low res)	180	4π	$4\pi/3$	11.78	0.75	3.87	5.89	60
Present (High res)	180	4π	$4\pi/3$	5.89	0.75	3.87	3.93	25

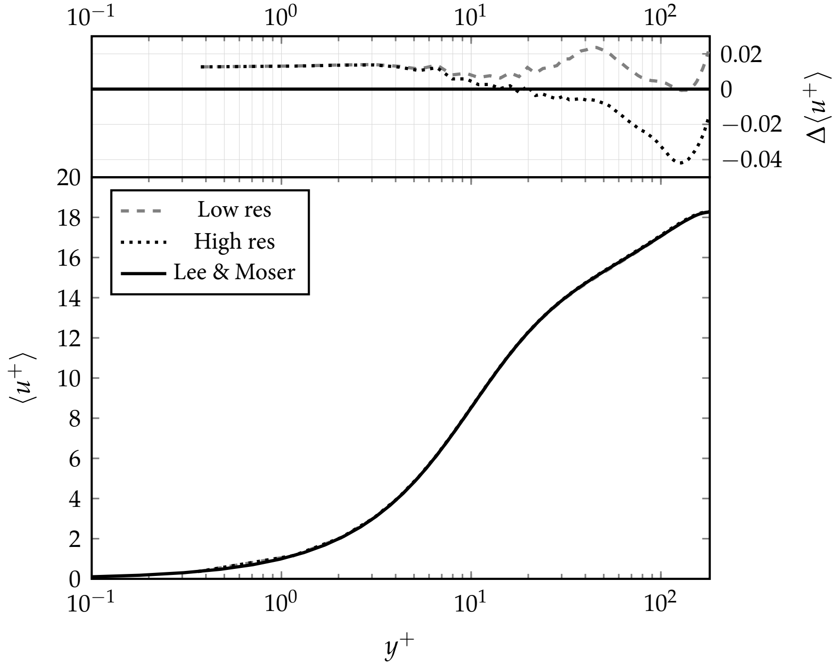

FIGURE A.1: Comparison of mean stream-wise velocity (u^+) along the channel height. On top, the $\Delta\langle u^+\rangle$ represent the difference between the data of Lee & Moser and present simulations.

than the present simulations. This is attributed to the slightly higher Reynolds number in their case. The differences in the other observed statistics could be due to the algorithms used, the simulation time, the finer resolution, and the large computational domain size. Additionally, it should be noted that the linear interpolation of Lee and Moser[51] data also introduces interpolation errors.

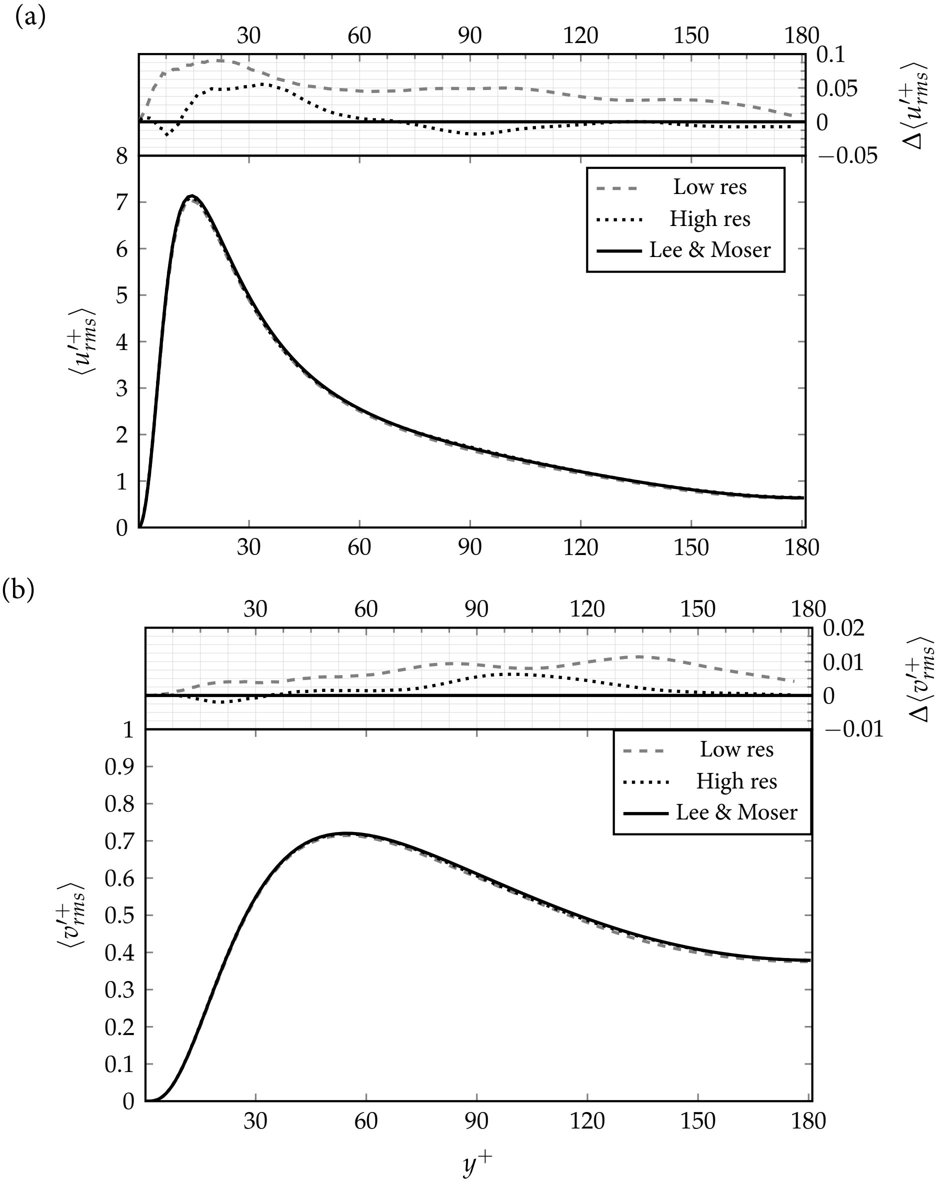

FIGURE A.2: Comparison of root mean square velocities along the channel height. On top of each plot (a,b), the $\Delta\langle u'^{+}_{rms}\rangle$ and $\Delta\langle v'^{+}_{rms}\rangle$ represent the difference between the data of Lee & Moser and present simulations.

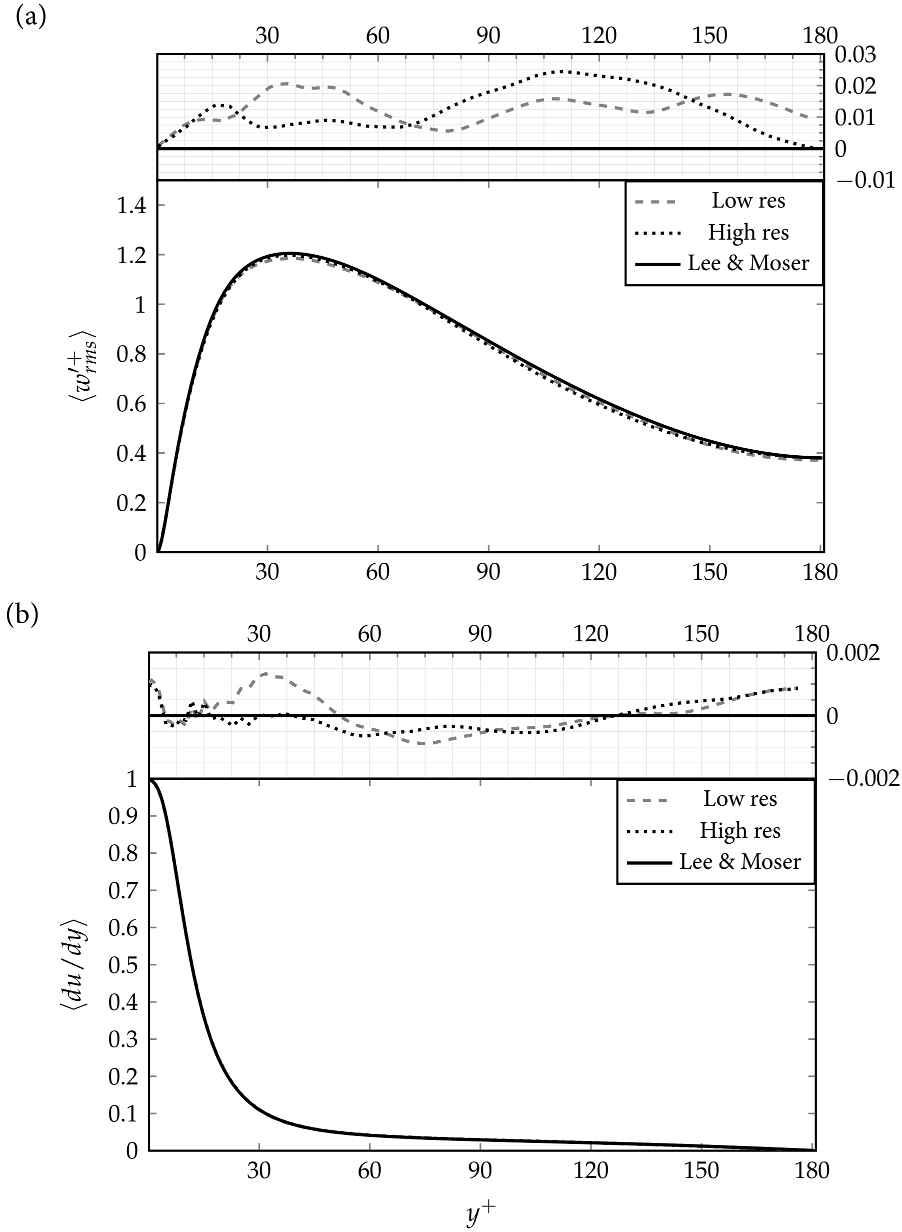

FIGURE A.3: Comparison of root mean square velocity and mean shear stress along the channel height. On top of each plot (a,b), the $\Delta\langle w'^{+}_{rms}\rangle$ and $\Delta\langle du/dy\rangle$ represent the difference between the data of Lee & Moser and present simulations.

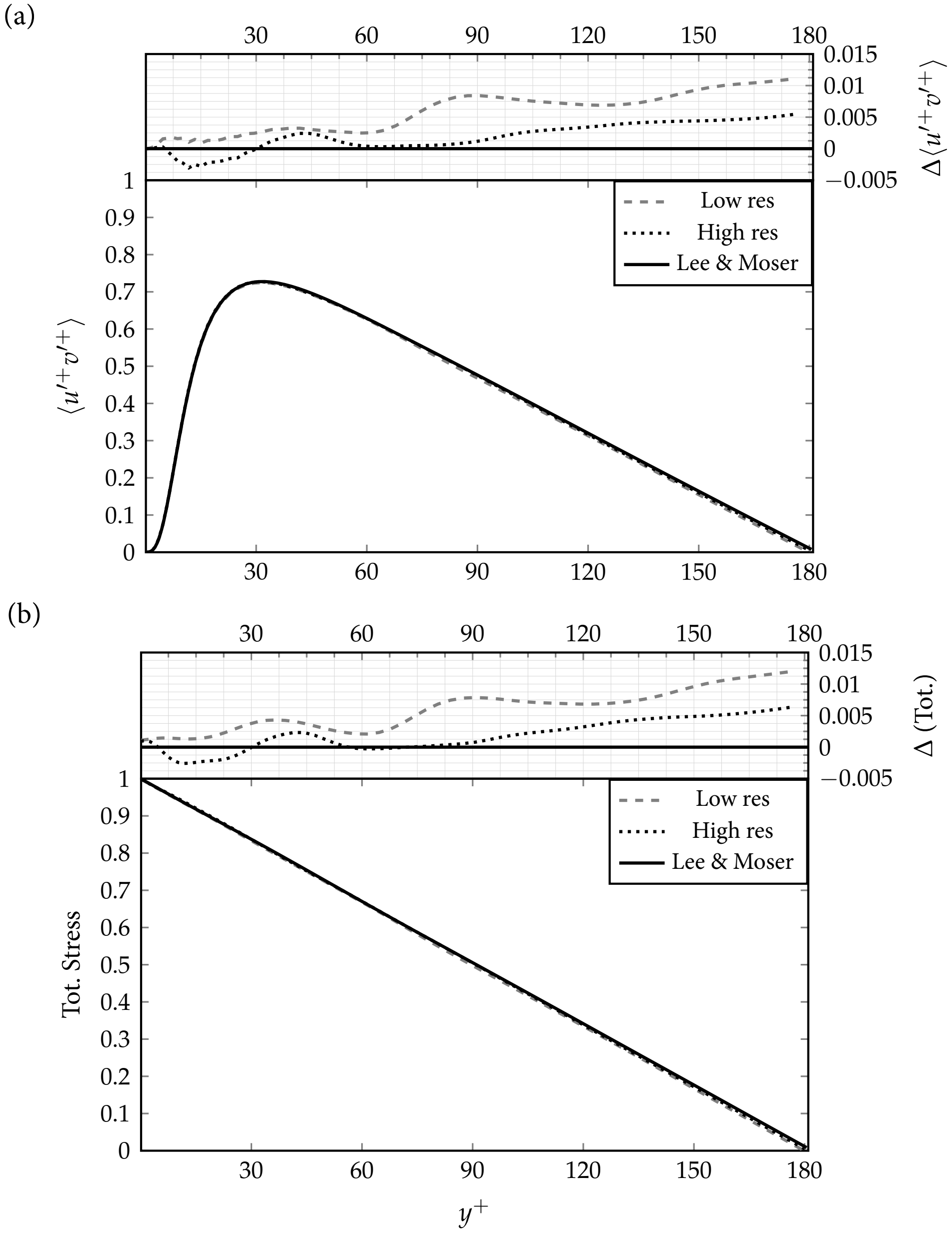

Figure A.4: Comparison of Reynolds shear stress and total stress along the channel height. On top of each plot (a,b), the $\Delta\langle u'^{+}v'^{+}\rangle$ and Δ (Tot.) represent the difference between the data of Lee & Moser and present simulations.

B

APPENDIX : ADDITIONAL EXAMPLES

This chapter provides few additional examples of the generation of new vortices (Chapter 3) and shear-layer structure extracted from vortex packets (Chapter 4). Four examples of auto-generation are shown in section B.1. And the shear-layer structures extracted from two different vortex packets are shown in section B.2.

B.1 AUTO-GENERATION

Among the four examples of auto-generation, three are slightly different from each other. The differences highlight the difficulties in identifying auto-generation. Each auto-generation example is illustrated by figures in two different planes, namely, vector plots of the perturbation velocities (u'^{+}, v'^{+}) in the cross-stream plane (xy) and the low-speed streak along with iso-surface of swirling strength in xz plane.

Auto-generation examples 1 and 2 were easy to detect, due to the high thresholds to identify low-speed streaks and vortices. This leads to fewer vortices and smaller low-speed streaks to track in time in three dimensional channel flow. Whereas, in examples 3 and 4 the thresholds were low, leading to large low-speed streaks and large overlapping vortices, which made it difficult to identify auto-generation visually. Additionally in example 4, the low-speed streak and the parent vortex are at an angle with the stream-wise direction. Hence it becomes difficult to identify the start and the end of auto-generation in xy plane, as the plane needs to be at an angle which requires interpolation and projection of velocities. This is also the reason the xy plane is not shown for example 4.

Time taken for the generation of a new vortex in all four examples was shown in table 3.1. It can be observed that the parent vortex with very low swirling strength (example 3) took longer to auto-generate, when the low-speed streak and vortex was aligned in stream-wise direction. When the alignment is at an angle (example 4), the auto-generation is observed to be faster. However, not many cases are studied to understand the mechanism behind it.

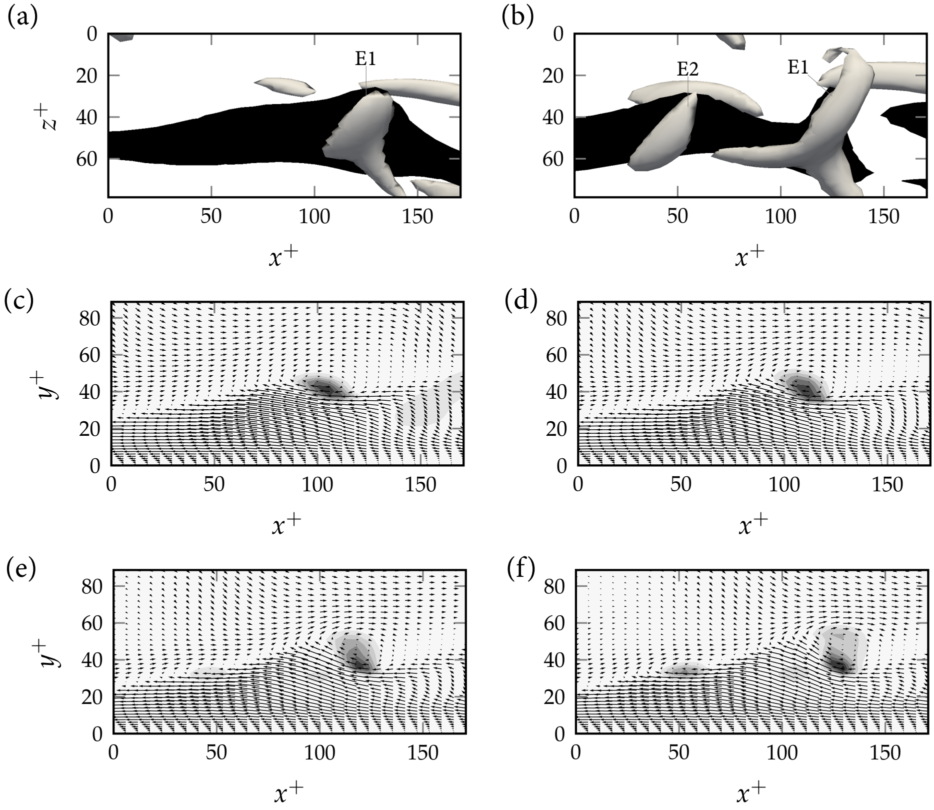

Figure B.1: Auto-generation example 1: Time taken to generate new vortex is 13.5 time wall units. Figures (a) and (b) represent relative times $t^+ = 0$ and 13.5, respectively. The black iso-surfaces represent low-speed streak at $u'^+ = -4$ and vortices are shown by gray iso-surfaces, which, represent 5% of the maximum local swirling strength squared. 'E1' and 'E2' are parent vortex and newly generated vortex, respectively. Figure (d)-(f) represent vector plots in xy plane at $z^+ = 45$ (see Fig a) at relative times $t^+ = 0,$ 4.5 ,9.0 and 13.5, respectively. Iso-contours from black to light gray in these figures show decreasing local swirling strength.

B.2 SHEAR-LAYER STRUCTURES AND VORTEX PACKETS

Two examples showing the link between vortex packets and shear-layer structure are presented here. The procedure to extract shear-layer structure is explained in section 4.2.1 of chapter 4.

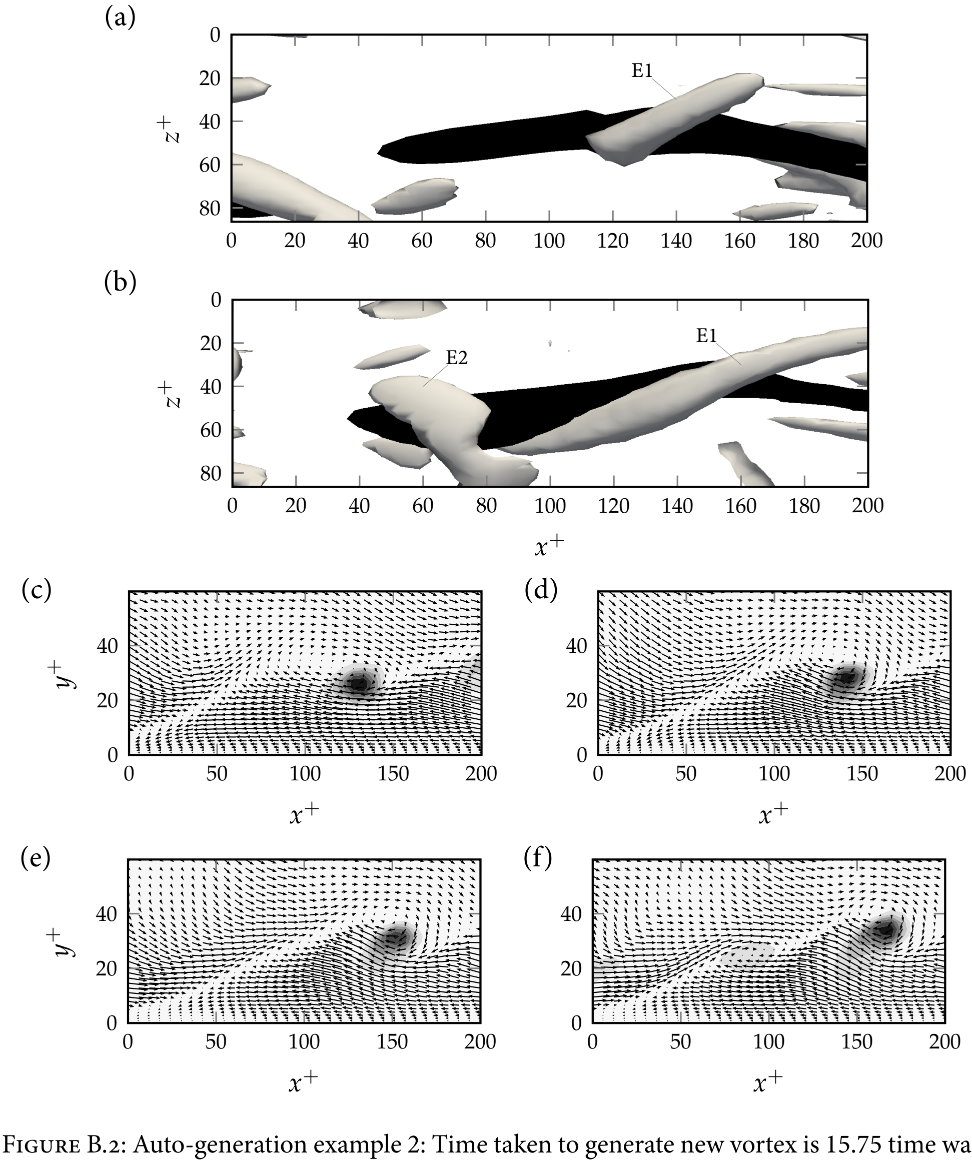

Figure B.2: Auto-generation example 2: Time taken to generate new vortex is 15.75 time wall units. Figures (a) and (b) represent relative times $t^+ = 0$ and 15.75, respectively. The black iso-surfaces represent low-speed streak at $u'^+ = -4$ and vortices are shown by gray iso-surfaces, which, represent 5% of the maximum local swirling strength squared. 'E1' and 'E2' are parent vortex and newly generated vortex, respectively. Figure (d)-(f) represent vector plots in xy plane at $z^+ = 45$ (see Fig a) at relative times $t^+ = 0,\ 6.75$, 11.25 and 15.75, respectively. Iso-contours from black to light gray in these figures show decreasing local swirling strength.

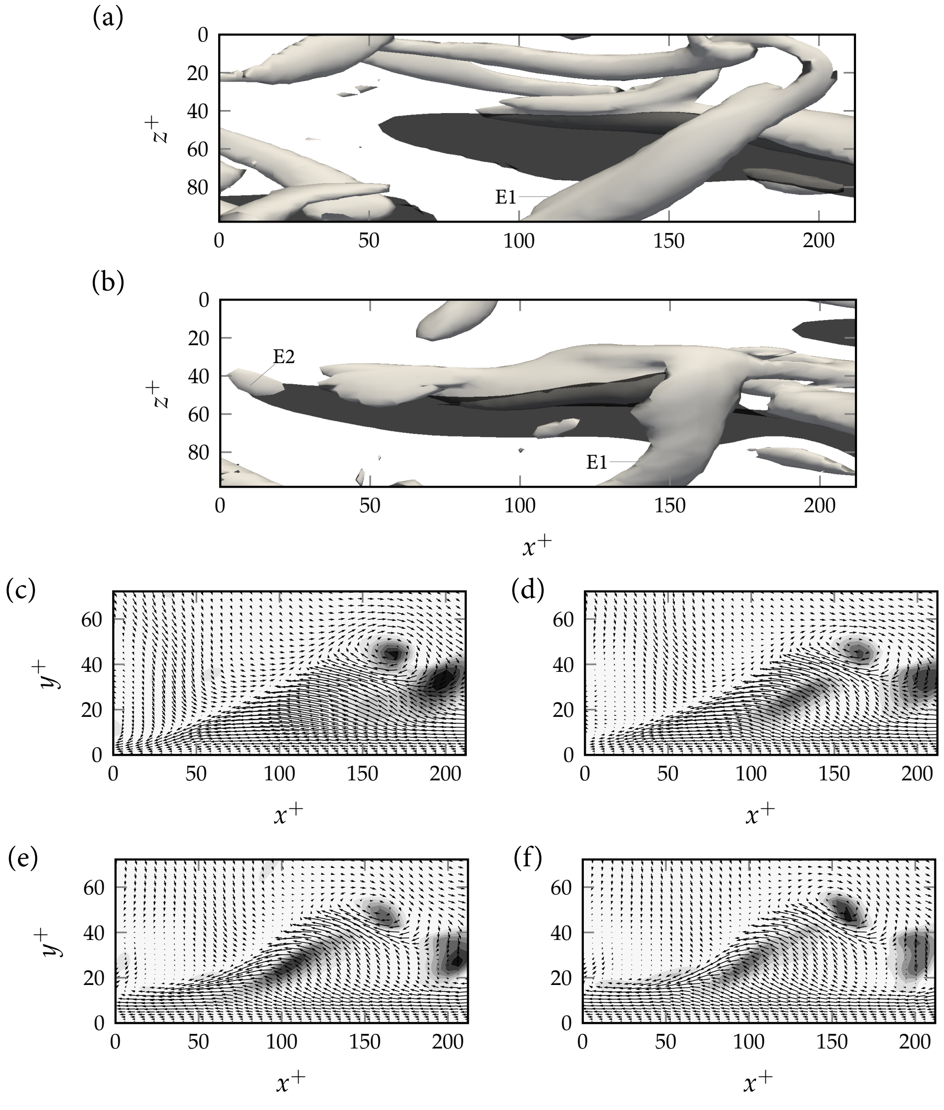

Figure B.3: Auto-generation example 3: Time taken to generate new vortex is 18.0 time wall units. Figures (a) and (b) represent relative times $t^+ = 0$ and 18.0, respectively. The black iso-surfaces represent low-speed streak at $u'^+ = -2.5$ and vortices are shown by gray iso-surfaces, which, represent 1% of the maximum local swirling strength squared. 'E1' and 'E2' are parent vortex and newly generated vortex, respectively. Low-speed streaks are made translucent to show the stream-wise legs on other side of the streaks. Figure (d)-(f) represent vector plots in xy plane at $z^+ = 48$ (see Fig a) at relative times $t^+ = 0,\ 6.75$, 13.5 and 18.0, respectively. Iso-contours from black to light gray in these figures show decreasing local swirling strength.

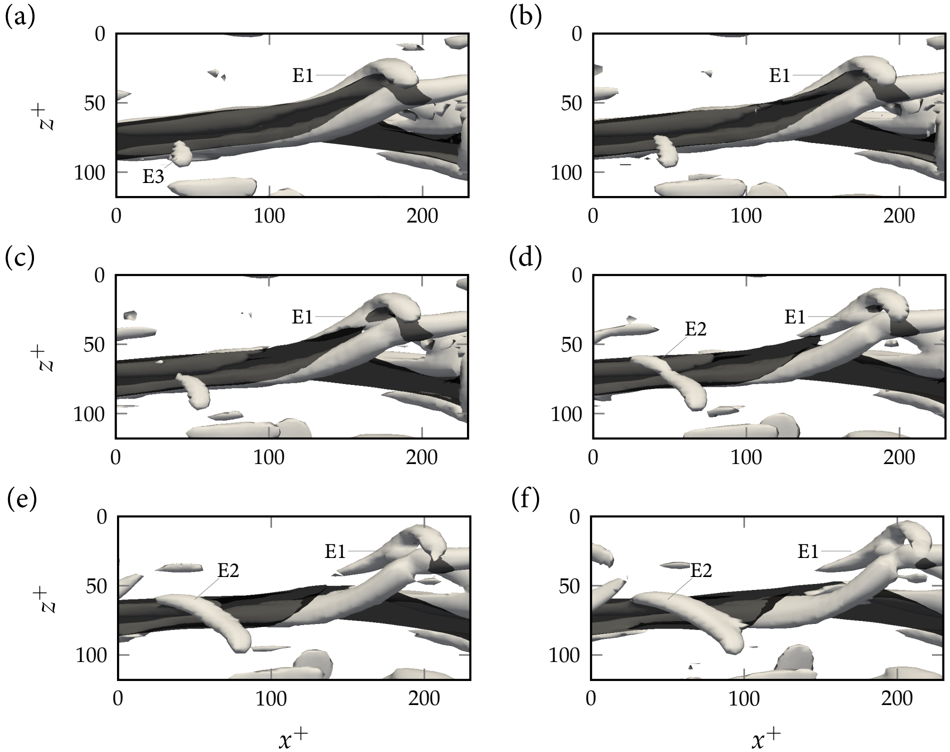

Figure B.4: Auto-generation example 4: Time taken to generate new vortex is 9.0 time wall units. Figures (a) and (f) represent relative times $t^+ = 0,\ 2.25,\ 4.5,\ 6.75,\ 9.0$ and 11.25, respectively. The black iso-surfaces represent low-speed streak at $u'^+ = -3.5$ and vortices are shown by gray iso-surfaces, which, represent 2% of the maximum local swirling strength squared. Low-speed streaks are made translucent to show the stream-wise legs on other side of the streaks. 'E1' and 'E2' are parent vortex and newly generated vortex, respectively. Vortex 'E3' is at a higher wall normal location and gets connected with 'E2' at $t^+ = 6.75$. And a swirl in the velocity vectors (not shown here) is observed at $t^+ = 11.25$.

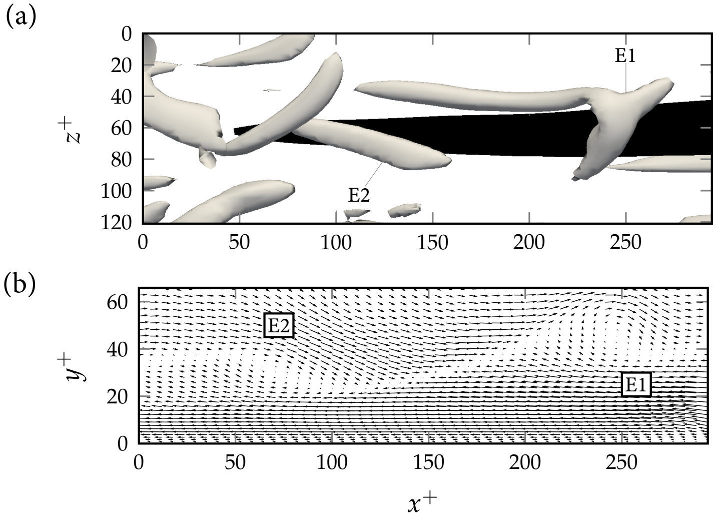

Figure B.5: Example vortex packet 1 : It consists of two vortices ‘E1’ and ‘E2’. The black iso-surfaces represent low-speed streak at $u'^+ = -4$ and vortices are shown by gray iso-surfaces, which, represent 5% of the maximum local swirling strength squared in plane xz in Fig (a). Fig (b) shows the perturbation velocity vectors in xy plane at $z^+ = 60$ (see Fig (a)).

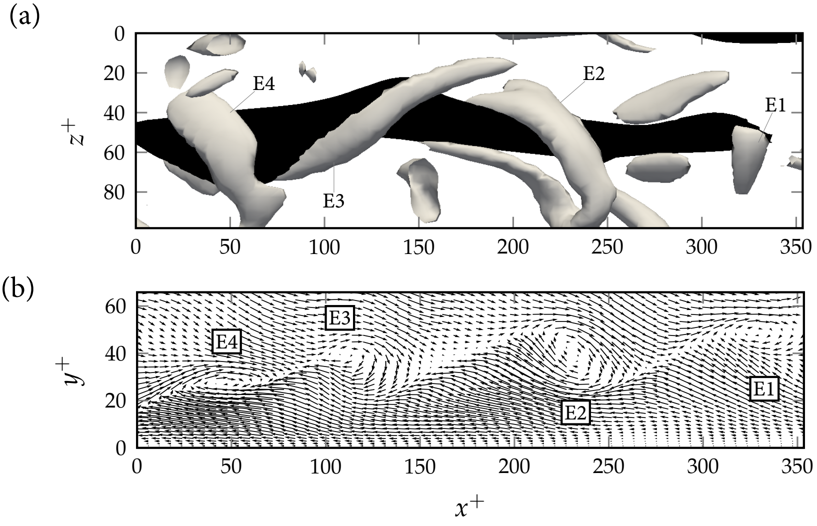

Figure B.6: Example vortex packet 2 : It consists of four vortices ‘E1’, ‘E2’, ‘E3’ and ‘E4’. The black iso-surfaces represent low-speed streak at $u'^+ = -4$ and vortices are shown by gray iso-surfaces, which, represent 5% of the maximum local swirling strength squared in plane xz in Fig (a). Fig (b) shows the perturbation velocity vectors in xy plane at $z^+ = 60$ (see Fig (a)).

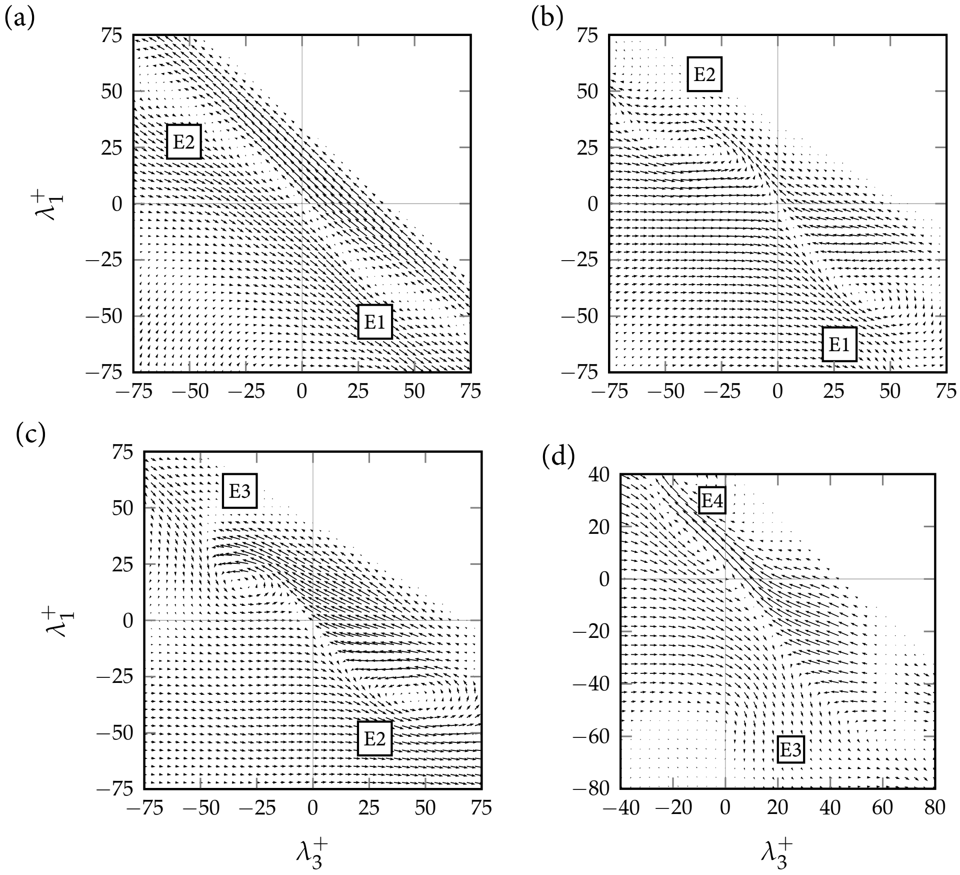

FIGURE B.7: Figure (a) and (b-d) show the vector plot in plane $\lambda_2 = 0$ of the extracted shear-layer structure from a vortex packet shown in figures B.5 and B.6, respectively. Wall of the channel can be observed on the top right side of the figure, where the vectors cease to exist.

REFERENCES

---

[1] R. J. Adrian, C. D. Meinhart, and C. D. Tomkins. "Vortex organization in the outer region of the turbulent boundary layer." *Journal of Fluid Mechanics* 422, pp. 1–54, 2000.

[2] A. Lozano-Durán and J. Jiménez. "Time-resolved evolution of coherent structures in turbulent channels: Characterization of eddies and cascades." *Journal of Fluid Mechanics* 759, pp. 432–471, 2014.

[3] B. J. Cantwell. "Organized motion in turbulent flow." *Annual Review of Fluid Mechanics* 13, pp. 457–515, 1981.

[4] A. E. Perry and M. S. Chong. "A description of eddying motions and flow patterns using critical-point concepts." *Annual Review of Fluid Mechanics* 19, pp. 125–155, 1987.

[5] M. S. Chong, A. E. Perry, and B. J. Cantwell. "A general classification of three-dimensional flow fields." *Physics of Fluids A: Fluid Dynamics* 2, pp. 765–777, 1990.

[6] H. M. Blackburn, N. N. Mansour, and B. J. Cantwell. "Topology of fine-scale motions in turbulent channel flow." *Journal of Fluid Mechanics* 310, pp. 269–292, 1996.

[7] G. E. Elsinga and I. Marusic. "Universal aspects of small-scale motions in turbulence." *Journal of Fluid Mechanics* 662, pp. 514–539, 2010.

[8] W. T. Ashurst, A. R. Kerstein, R. M. Kerr, and C. H. Gibson. "Alignment of vorticity and scalar gradient with strain rate in simulated Navier-Stokes turbulence." *Physics of Fluids (1958-1988)* 30, pp. 2343–2353, 1987.

[9] R. J. Adrian. "Hairpin vortex organization in wall turbulence." *Physics of Fluids* 19, p. 041301, 2007.

[10] K.-S. Choi. "Near-wall structure of a turbulent boundary layer with riblets." *Journal of Fluid Mechanics* 208, pp. 417–458, 1989.

[11] D. C. Chu and G. E. Karniadakis. "A direct numerical simulation of laminar and turbulent flow over riblet-mounted surfaces." *Journal of Fluid Mechanics* 250, pp. 1–42, 1993.

[12] Y. P. Tang and D. G. Clark. "On near-wall turbulence-generating events in a turbulent boundary layer on a riblet surface." *Applied scientific research* 50, pp. 215–232, 1993.

[13] Y. Suzuki and N. Kasagi. "Turbulent drag reduction mechanism above a riblet surface." *AIAA Journal* 32, pp. 1781–1790, 1994.

[14] Y. Sumitani and N. Kasagi. "Direct numerical simulation of turbulent transport with uniform wall injection and suction." *AIAA journal* 33, pp. 1220–1228, 1995.

[15] D. Goldstein, R. Handler, and L. Sirovich. "Direct numerical simulation of turbulent flow over a modeled riblet covered surface." *Journal of Fluid Mechanics* 302, pp. 333–376, 1995.

[16] P. K. Ptasinski, B. J. Boersma, F. T. M. Nieuwstadt, M. A. Hulsen, B. H.A.A.V. D. Brule, and J. C. R. Hunt. "Turbulent channel flow near maximum drag reduction: simulations, experiments and mechanisms." *Journal of Fluid Mechanics* 490, pp. 251–291, 2003.

[17] Y. Dubief, V. E. Terrapon, C. M. White, E. S. G. Shaqfeh, P. Moin, and S. K. Lele. "New answers on the interaction between polymers and vortices in turbulent flows." *Flow, Turbulence, and Combustion* 74, pp. 311–329, 2005.

[18] S.-J. Lee and Y.-S. Choi. "Decrement of spanwise vortices by a drag-reducing riblet surface." *Journal of Turbulence* 9, N23, 2008.

[19] C. M. White and M. G. Mungal. "Mechanics and prediction of turbulent drag reduction with polymer additives." *Annual Review of Fluid Mechanics* 40, pp. 235–256, 2008.

[20] B. Dean and B. Bhushan. "Shark-skin surfaces for fluid-drag reduction in turbulent flow: a review." *Philosophical Transactions of the Royal Society A: Mathematical, Physical and Engineering Sciences* 368, pp. 4775–4806, 2010.

[21] Y. Kametani and K. Fukagata. "Direct numerical simulation of spatially developing turbulent boundary layer for skin friction drag reduction by wall surface-heating or cooling." *Journal of Turbulence* 13, N34, 2012.

[22] P. Bandyopadhyay. "Large structure with a characteristic upstream interface in turbulent boundary layers." *Physics of Fluids* 23, p. 2326, 1980.

[23] M. R. Head and P. Bandyopadhyay. "New aspects of turbulent boundary-layer structure." *Journal of Fluid Mechanics* 107, pp. 297–338, 1981.

[24] M. S. Acarlar and C. R. Smith. "A study of hairpin vortices in a laminar boundary layer. Part 2. Hairpin vortices generated by fluid injection." *Journal of Fluid Mechanics* 175, pp. 43–83, 1987.

[25] B. Ganapathisubramani, E. K. Longmire, and I. Marusic. "Characteristics of vortex packets in turbulent boundary layers." *Journal of Fluid Mechanics* 478, pp. 35–46, 2003.

[26] R. J. Adrian. "Stochastic estimation of conditional structure: A review." *Applied Scientific Research* 53, pp. 291–303, 1994.

[27] R. J. Adrian. "Stochastic estimation of the structure of turbulent fields." In: *Eddy Structure Identification*. Ed. by J. P Bonnet, pp. 145–195. CISM International Centre for Mechanical Sciences. Springer-Verlag, 1996.

[28] J. Zhou, R. J. Adrian, S. Balachandar, and T. M. Kendall. "Mechanisms for generating coherent packets of hairpin vortices in channel flow." *Journal of Fluid Mechanics* 387, pp. 353–396, 1999.

[29] R. J. Adrian, S. Balachandar, and Z. C. Liu. "Spanwise growth of vortex structure in wall turbulence." *KSME International Journal* 15, pp. 1741–1749, 2001.

[30] C. R. Smith, J. D. A. Walker, A. H. Haidari, and U. Sobrun. "On the dynamics of near-wall turbulence." *Philosophical Transactions of the Royal Society A: Mathematical, Physical and Engineering Sciences* 336, pp. 131–175, 1991.

[31] A. H. Haidari and C. R. Smith. "The generation and regeneration of single hairpin vortices." *Journal of Fluid Mechanics* 277, pp. 135–162, 1994.

[32] G. Eitel-Amor, R. Örlü, P. Schlatter, and O. Flores. "Hairpin vortices in turbulent boundary layers." *Physics of Fluids* 27, 025108, 2015.

[33] K. Kim, H. J. Sung, and R. J. Adrian. "Effects of background noise on generating coherent packets of hairpin vortices." *Physics of Fluids* 20, p. 105107, 2008.

[34] D. Greenblatt and I. J. Wygnanski. "The control of flow separation by periodic excitation." *Progress in Aerospace Sciences* 36, pp. 487–545, 2000.

[35] M. Sato, T. Nonomura, K. Okada, K. Asada, H. Aono, A. Yakeno, Y. Abe, and K. Fujii. "Mechanisms for laminar separated-flow control using dielectric-barrier-discharge plasma actuator at low Reynolds number." *Physics of Fluids* 27, p. 117101, 2015.

[36] Y. Jodai and G. E. Elsinga. "Experimental observation of hairpin auto-generation events in a turbulent boundary layer." *Journal of Fluid Mechanics* 795, pp. 611–633, 2016.

[37] S. Goto and J. C. Vassilicos. "Particle pair diffusion and persistent streamline topology in two-dimensional turbulence." *New Journal of Physics* 6, p. 65, 2004.

[38] M. V. Goudar, W.-P. Breugem, and G. E. Elsinga. "Auto-generation in wall turbulence by the interaction of weak eddies." *Physics of Fluids* 28, p. 035111, 2016.

[39] L. Brandt and H. C. de Lange. "Streak interactions and breakdown in boundary layer flows." *Physics of Fluids* 20, p. 024107, 2008.

[40] C. R. Smith. "A synthesized model of the near-wall behavior in turbulent boundary layers." In: *Proceedings of the Eighth Symposium on Turbulence*. Ed. by G. K. Patterson and J. L. Zakin, pp. 299–327. Department of Chemical Engineering, University of Missouri-Rolla, 1984.

[41] S. K. Robinson. "Coherent motions in the turbulent boundary layer." *Annual Review of Fluid Mechanics* 23, pp. 601–639, 1991.

[42] P. Schlatter, Q. Li, R. Örlü, F. Hussain, and D. Henningson. "On the near-wall vortical structures at moderate Reynolds numbers." *European Journal of Mechanics - B/Fluids* 48, pp. 75–93, 2014.

[43] B. A. Singer and R. D. Joslin. "Metamorphosis of a hairpin vortex into a young turbulent spot." *Physics of Fluids* 6, pp. 3724–3736, 1994.

[44] M. Asai and M. Nishioka. "Boundary-layer transition triggered by hairpin eddies at subcritical Reynolds numbers." *Journal of Fluid Mechanics* 297, pp. 101–122, 1995.

[45] S. Bake, D. G. W. Meyer, and U. Rist. "Turbulence mechanism in Klebanoff transition: A quantitative comparison of experiment and direct numerical simulation." *Journal of Fluid Mechanics* 459, pp. 217–243, 2002.

[46] G. E. Elsinga, C. Poelma, A. Schröder, R. Geisler, F. Scarano, and J. Westerweel. "Tracking of vortices in a turbulent boundary layer." *Journal of Fluid Mechanics* 697, pp. 273–295, 2012.

[47] P. K. Parthasarathy. "Dynamics of vortices in numerically simulated turbulent channel flow." MA thesis. Arizona State University, 2011.

[48] M. Frigo and S. Johnson. "The design and implementation of FFTW3." *Proceedings of the IEEE* 93, pp. 216–231, 2005.

[49] B. J. Boersma. "A 6th order staggered compact finite difference method for the incompressible Navier-Stokes and scalar transport equations." *Journal of Computational Physics* 230, pp. 4940–4954, 2011.

[50] B. J. Boersma. "A staggered compact finite difference formulation for the compressible Navier-Stokes equations." *Journal of Computational Physics* 208, pp. 675–690, 2005.

[51] M. Lee and R. D. Moser. "Direct numerical simulation of turbulent channel flow up to $Re_\tau \approx 5200$." *Journal of Fluid Mechanics* 774, pp. 395–415, 2015.

[52] G. E. Elsinga, R. J. Adrian, B. W. V. Oudheusden, and F. Scarano. "Three dimensional vortex organization in a high-Reynolds-number supersonic turbulent boundary layer." *Journal of Fluid Mechanics* 644, pp. 35–60, 2010.

[53] M. J. Ringuette, M. Wu, and M. P. Martín. "Coherent structures in direct numerical simulation of turbulent boundary layers at Mach 3." *Journal of Fluid Mechanics* 594, pp. 59–69, 2008.

[54] L. Rosenhead. "The formation of vortices from a surface of discontinuity." *Proceedings of the Royal Society A: Mathematical, Physical and Engineering Sciences* 134, pp. 170–192, 1931.

[55] P. Atsavapranee and M. Gharib. "Structures in stratified plane mixing layers and the effects of cross-shear." *Journal of Fluid Mechanics* 342, pp. 53–86, 1997.

[56] G. E. Elsinga and I. Marusic. "The anisotropic structure of turbulence and its energy spectrum." *Physics of Fluids* 28, p. 011701, 2016.

[57] L. Wei, G. E. Elsinga, G. Brethouwer, P. Schlatter, and A. V. Johansson. "Universality and scaling phenomenology of small-scale turbulence in wall-bounded flows." *Physics of Fluids* 26, p. 035107, 2014.

[58] T. Ishihara, Y. Kaneda, and J. C. R. Hunt. "Thin shear layers in high Reynolds number turbulence DNS results." *Flow, Turbulence and Combustion* 91, pp. 895–929, 2013.

[59] L. F. Richardson. "Atmospheric diffusion shown on a distance-neighbour graph." *Proceedings of the Royal Society A: Mathematical, Physical and Engineering Sciences* 110, pp. 709–737, 1926.

[60] G. K. Batchelor. "The application of the similarity theory of turbulence to atmospheric diffusion." *Quarterly Journal of the Royal Meteorological Society* 76, pp. 133–146, 1950.

[61] G. K. Batchelor. "Diffusion in a field of homogeneous turbulence." *Mathematical Proceedings of the Cambridge Philosophical Society* 48, pp. 345–362, 1952.

[62] G. K. Batchelor. "The effect of homogeneous turbulence on material lines and surfaces." *Proceedings of the Royal Society A: Mathematical, Physical and Engineering Sciences* 213, pp. 349–366, 1952.

[63] I. T. Drummond and W. Münch. "Turbulent stretching of line and surface elements." *Journal of Fluid Mechanics* 215, pp. 45–59, 1990.

[64] S. S. Girimaji and S. B. Pope. "Material-element deformation in isotropic turbulence." *Journal of Fluid Mechanics* 220, pp. 427–458, 1990.

[65] M. Guala, A. Liberzon, B. Lüthi, W. Kinzelbach, and A. Tsinober. "Stretching and tilting of material lines in turbulence: The effect of strain and vorticity." *Physical Review E* 73, p. 036303, 2006.

[66] B. J. Devenish. "Geometrical properties of turbulent dispersion." *Physical Review Letters* 110, p. 064504, 2013.

[67] J. F. Hackl, P. K. Yeung, and B. L. Sawford. "Multi-particle and tetrad statistics in numerical simulations of turbulent relative dispersion." *Physics of Fluids* 23, p. 065103, 2011.

[68] L. Biferale, G. Boffetta, A. Celani, B. J. Devenish, A. Lanotte, and F. Toschi. "Multiparticle dispersion in fully developed turbulence." *Physics of Fluids* 17, p. 111701, 2005.

[69] H. Xu, A. Pumir, and E. Bodenschatz. "The pirouette effect in turbulent flows." *Nature Physics* 7, pp. 709–712, 2011.

[70] H. Xu, N. T. Ouellette, and E. Bodenschatz. "Evolution of geometric structures in intense turbulence." *New Journal of Physics* 10, p. 013012, 2008.

[71] M. Chertkov, A. Pumir, and B. I. Shraiman. "Lagrangian tetrad dynamics and the phenomenology of turbulence." *Physics of Fluids* 11, pp. 2394–2410, 1999.

[72] A. Pumir, E. Bodenschatz, and H. Xu. "Tetrahedron deformation and alignment of perceived vorticity and strain in a turbulent flow." *Physics of Fluids* 25, p. 035101, 2013.

[73] A. E. Perry and I. Marusic. "A wall-wake model for the turbulence structure of boundary layers. Part 1. Extension of the attached eddy hypothesis." *Journal of Fluid Mechanics* 298, pp. 361–388, 1995.

[74] J. P. Salazar and L. R. Collins. "Two-particle dispersion in isotropic turbulent flows." *Annual Review of Fluid Mechanics* 41, pp. 405–432, 2009.

[75] J. M. Burgers. "On the resistance of fluids and vortex motion." *Koninklijke Nederlandse Akademie van Wetenschappen Proceedings Series B Physical Sciences* 23, pp. 774–782, 1921.

[76] J. Jimenez and A. A. Wray. "On the characteristics of vortex filaments in isotropic turbulence." *Journal of Fluid Mechanics* 373, pp. 255–285, 1998.

[77] C. B. da Silva, R. J. N. dos Reis, and J. C. F. Pereira. "The intense vorticity structures near the turbulent/non-turbulent interface in a jet." *Journal of Fluid Mechanics* 685, pp. 165–190, 2011.

[78] P. K. Yeung, S. B. Pope, and B. L. Sawford. "Reynolds number dependence of Lagrangian statistics in large numerical simulations of isotropic turbulence." *Journal of Turbulence* 7, N58, 2006.

[79] B. L. Sawford, P. K. Yeung, and J. F. Hackl. "Reynolds number dependence of relative dispersion statistics in isotropic turbulence." *Physics of Fluids* 20, p. 065111, 2008.

[80] R. Bitane, H. Homann, and J. Bec. "Geometry and violent events in turbulent pair dispersion." *Journal of Turbulence* 14, pp. 23–45, 2013.

[81] R. Bitane, H. Homann, and J. Bec. "Time scales of turbulent relative dispersion." *Physical Review E* 86, p. 045302, 2012.

[82] Y. Li, E. Perlman, M. Wan, Y. Yang, C. Meneveau, R. Burns, S. Chen, A. Szalay, and G. Eyink. "A public turbulence database cluster and applications to study Lagrangian evolution of velocity increments in turbulence." *Journal of Turbulence* 9, N31, 2008.

[83] E. B. Saff and A. B. Kuijlaars. "Distributing many points on a sphere." *The mathematical intelligencer* 19, pp. 5–11, 1997.

[84] E. Dresselhaus and M. Tabor. "The kinematics of stretching and alignment of material elements in general flow fields." *Journal of Fluid Mechanics* 236, pp. 415–444, 1992.

[85] W. Schoppa and F. Hussain. "Coherent structure generation in near-wall turbulence." *Journal of Fluid Mechanics* 453, pp. 57–108, 2002.

[86] L. Brandt, P. Schlatter, and D. S. Henningson. "Transition in boundary layers subject to free-stream turbulence." *Journal of Fluid Mechanics* 517, pp. 167–198, 2004.

[87] P. Schlatter, L. Brandt, H. C. de Lange, and D. S. Henningson. "On streak breakdown in bypass transition." *Physics of Fluids* 20, 101505, 2008.

[88] D. G. Bogard and W. G. Tiederman. "Burst detection with single-point velocity measurements." *Journal of Fluid Mechanics* 162, pp. 389–413, 1986.

[89] S. Tardu. "Characteristics of single and clusters of bursting events in the inner layer." *Experiments in Fluids* 20, pp. 112–124.

[90] S. Tardu. "Characteristics of single and multiple bursting events in the inner layer. Part 2. Level-crossing events." *Experiments in Fluids* 33, pp. 640–652, 2002.

[91] M. Metzger, B. McKeon, and E. Arce-Larreta. "Scaling the characteristic time of the bursting process in the turbulent boundary layer." *Physica D: Nonlinear Phenomena* 239, pp. 1296 –1304, 2010.

[92] T. Michioka, H. Takimoto, and A. Sato. "Large-eddy simulation of pollutant removal from a three-dimensional street canyon." *Boundary-Layer Meteorology* 150, pp. 259–275, 2014.

[93] R. T. Reynolds and I. P. Castro. "Measurements in an urban-type boundary layer." *Experiments in Fluids* 45, pp. 141–156, 2008.

[94] J. Tomas. "Obstacle-resolving large-eddy simulation of dispersion in urban enviornments." PhD thesis. Delft University of Technology, 2016.

[95] H. E. Eisma. "Pollutant dispersion in wall-bounded turbulent flows." PhD thesis. Delft University of Technology, 2017.

[96] C. M. de Silva, N. Hutchins, and I. Marusic. "Uniform momentum zones in turbulent boundary layers." *Journal of Fluid Mechanics* 786, pp. 309–331, 2016.

[97] M. P. Simens, J. Jiménez, S. Hoyas, and Y. Mizuno. "A high-resolution code for turbulent boundary layers." *Journal of Computational Physics* 228, pp. 4218 – 4231, 2009. ISSN: 0021-9991.

One's life is like a particle in a turbulent flow, where even the smallest of the changes can have a largest influence and the largest of the changes can have a smallest influence. What I am today, is the sum of all those smallest to largest changes over time. And I thank all those people who have been a part of this.

ACKNOWLEDGMENTS

First and foremost I would like to express my sincerest gratitude to dr.ir. G.E. Elsinga, my research supervisor, for his patient guidance, constant encouragement and useful critiques of this work. His willingness to give time and invaluable assistance so generously has been very much appreciated. Secondly, I am grateful to my promoter prof.dr.ir. J. Westerweel without whose assistance this study would not be successful. Even the smallest interactions with you have taught me a lot of things. Additionally, I am thankful for allowing me to work in my own independent way. Finally, a special thanks goes out to STW for helping and providing the funding for this work.

With a special mention to prof.dr.ir. Bendiks Jan Boersma for his guidance and valuable inputs on numerical algorithms and libraries required for direct numerical simulation (DNS), which led to the development of an efficient DNS code. I greatly appreciate him and dr.ir. M.J.B.M. Pourquie for the help in the usage of supercomputers. Also, I thank Dr.ir. W.-P. Breugem for suggestions and discussions related to numerics. Furthermore, I am grateful to Mark Franken for translating the abstract to Dutch. Finally, I am indebted to the many countless contributors to the "Free Software/Open Source" programming community for providing the numerous tools and systems I have used to produce both my results and this thesis.

In my daily work and life, I have been blessed with a friendly and cheerful group of colleagues and friends. I always felt our room was a jungle filled wonderful people, like Marieke, Sita, Jasper, Florian, Dries, Gem, Erik, Koen and his fishes. I thank them for all the useful and chaotically useless, but fun, discussions over the last four and half years. I would like to express my gratitude to Rob van den Boogaard and our secretaries Ria and Caroline for lightening my burden in administrative tasks. dr.ir Mathieu Pourquie, thanks for all the history lessons, crazy stories of the lab, and most importantly your extensive and unforgettable teachings on Belgium beers. I really appreciate the patience and effort by Dr. René Delfos to teach me Dutch every time I tried talking to him. René, *Ik beloof dat ik op een dag Nederlands zal leren*. In no order, I would like to thank Pepijn, Pedro, Jerke, Norbert, Edwin, Andries, Arnoud, Christian, Ernst Jan, Melika, Maurice, Greta, Soren, Jan, Jasper, Henk, Daniel, Valentina, Gosse, Gijs, Dirk, Aris, Saad, Mike, Arati, Daniele, Sedat, and Ankur for all the good times in the lab and have helped me directly or indirectly in pursuing my thesis. Lennon and Naina, thanks for all the fun weekends and trips. Susheel, it was nice meeting you in Europe and sharing and talking about our old school days. I am also thankful to all my tango, football and other friends for all the happy times in Delft.

I would like to extend special thanks to my friends, Arjun, Debarshi and Rakesh. I partly owe my knowledge on computers to them. In addition to these three, Roar, Paul, Chris, Elise, and Bjorn, I cannot thank you guys enough for all the help, moral and emotional support through out my PhD. I take this opportunity to tell Johann Dugge and all the Dugge family for being a family away from home. I consider the beautiful memories of Christmas and the new year with you all as one of the treasures of my life in Europe.

Finally, many things can come and go but family will always be there. I am very grateful to my sister and parents for always being with me and supporting me in every way throughout my studies and life. Many Thanks!

CURRICULUM VITAE

Manu V Goudar

03-10-1985	Born in Shivapura, Karnataka, India.
1996–2003	Secondary school, Sainik (Army) School, Bijapur, Karnataka, India.
2003–2007	Bachelor of Technology in Mechanical Engineering National Institute of Technology Hamirpur, Hamirpur, Himachal Pradesh, India.
2007–2010	Scientist, Center for Military Airworthiness and Certification, Defense Research and Development Organization, India.
2010–2012	Master of science in Mechanical Engineering, Specialization in Computational Fluid mechanics and Turbulence, Technische Universiteit Delft, The Netherlands.
2012–2017	PhD in Laboratory of Aero & Hydrodynamics, Mechanical Engineering, Technische Universiteit Delft, The Netherlands.

PUBLICATIONS

PAPERS

1. M.V. Goudar, W-P. Breugem, G.E. Elsinga, *Auto-generation in wall turbulence by the interaction of weak eddies*, Physics of Fluids, **28**, 035111, (2016) http://dx.doi.org/10.1063/1.4944048
2. M.V. Goudar, G.E. Elsinga, *Possible modification of the large-scale flow structures by vortical structural interactions* J. Phys.: Conf. Ser. **506 (1)**, (2014). http://doi.org/10.1088/1742-6596/506/1/012012
3. M.V. Goudar, G.E. Elsinga, *Tracer particle dispersion around elementary flow patterns.*
   Under review, JFM.
4. G.E. Elsinga, T. Ishihara, M.V. Goudar, C.B. da Silva, and J.C.R. Hunt, *The scaling of straining motions in homogeneous isotropic turbulence.*
   Under review, JFM.

CONFERENCES

1. M.V. Goudar, W-P. Breugem, Y. Jodai, G.E. Elsinga, *Auto-generation by interaction of weak eddies*, 24th International Congress of Theoretical and Applied Mechanics, Montreal, Canada, Aug 21-26, 2016.
2. M.V. Goudar, W-P. Breugem, G.E. Elsinga, *Auto-generation in wall turbulence by the interaction of weak eddies*, Physics@FOM, Veldhoven, The Netherlands, Jan, 2016.
3. M.V. Goudar, G.E. Elsinga, *Pair dispersion statistics and coherent structures*, European Turbulence Conference-15, Delft, The Netherlands, Aug, 2015. http://www.etc15.nl/proceedings/proceedings/documents/170.pdf
4. M.V. Goudar, W-P. Breugem, G.E. Elsinga, *Merging and auto-generation of vortices in wall bounded flow*, Turbulence and Shear Flow Phenomenon-8, Poitiers,

France, Aug 28-30 2013.
http://www.tsfp-conference.org/proceedings/2013/v1/coh1d.pdf

5. G.E. Elsinga, M.V. Goudar, W-P. Breugem, *Merging and auto-generation of vortices in wall bounded flow*, American Physical Society, San Diego, California, Nov 18-20 2012.
   http://meetings.aps.org/Meeting/DFD12/Event/177298

PROPOSITIONS

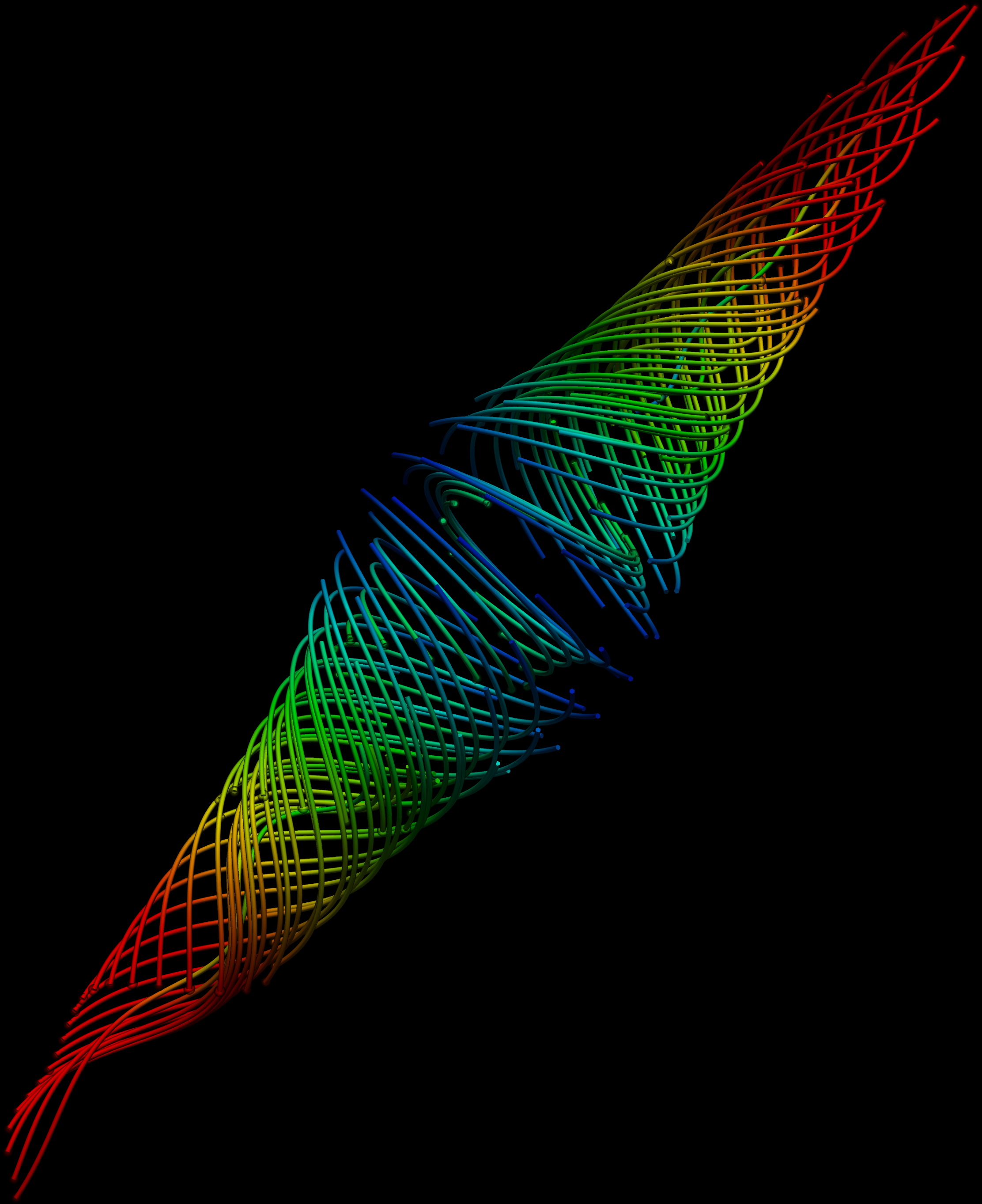1. For drag reduction, it is important to quantify the influence of flow from the outer region. (This thesis, Chapters 2,3)
2. The development of better vortex identification techniques helps in improving the understanding of turbulence. (This thesis)
3. Simultaneous optimization and parallelization of a code leads to recursive debugging and further paralysis.
4. Similar to a particle pair in turbulence, sometimes, faster growth in life pushes you away from initial relationships. And eventually, lose them.
5. The farther you go from the norms of society, the lesser you are in its eyes.
6. What we see on media is the portrayal of society's opinion.
7. A strong belief in something makes us find uncertainties in others to justify ourselves.
8. A thesis needs an unacknowledgement section.